PREPARATION AND CHARACTERIZATION OF Pt NANOCATALYSTS
SUPPORTED BY THIOUREA-TREATED GO NANOPARTICLES:
THE APPLICATION TO ANODIC PROCESS IN DMFC

A THESIS SUBMITTED TO
THE GRADUATE SCHOOL OF NATURAL AND APPLIED SCIENCES
OF
MIDDLE EAST TECHNICAL UNIVERSITY

BY

TOPRAK SEDA KARAOSMANOĞLU

IN PARTIAL FULFILLMENT OF THE REQUIREMENTS
FOR
THE DEGREE OF MASTER OF SCIENCE
IN
CHEMISTRY

SEPTEMBER 2017

Approval of the thesis:

**PREPARATION AND CHARACTERIZATION OF Pt NANOCATALYSTS
SUPPORTED BY THIOUREA-TREATED GO NANOPARTICLES:
THE APPLICATION TO ANODIC PROCESS IN DMFC**

Submitted by **Toprak Seda Karaosmanoğlu** in partial fulfillment of the requirements for the degree of **Master of Science in Chemistry Department, Middle East Technical University** by,

Prof. Dr. Gülbin Dural Ünver
Dean, Graduate School of **Natural and Applied Sciences**   _____

Prof. Dr. Cihangir Tanyeli
Head of Department, **Chemistry**   _____

Prof. Dr. Gülsün Gökağaç
Supervisor, **Chemistry Dept., METU**   _____

Examining Committee Members:

Prof. Dr. Mürvet Volkan
Chemistry Dept., METU   _____

Prof. Dr. Gülsün Gökağaç
Chemistry Dept., METU   _____

Prof. Dr. Metin Aydın
Chemistry Dept., Ondokuz Mayıs University   _____

Prof. Dr. Ceyhan Kayran
Chemistry Dept., METU   _____

Assoc. Prof. Dr. Emren Nalbant Esentürk
Chemistry Dept., METU   _____

Date: 07/09/2017

I hereby declare that all information in this document has been obtained and presented in accordance with academic rules and ethical conduct. I also declare that, as required by these rules and conduct, I have fully cited and referenced all material and results that are not original to this work.

Name, Last name : Toprak Seda Karaosmanoğlu

Signature :

ABSTRACT

PREPARATION AND CHARACTERIZATION OF Pt NANOCATALYSTS SUPPORTED BY THIOUREA-TREATED GO NANOPARTICLES: THE APPLICATION TO ANODIC PROCESS OF DMFC

Karaosmanoğlu, Toprak Seda

M. Sc., Department of Chemistry

Supervisor: Prof. Dr. Gülsün Gökağaç

September 2017, 127 pages

In this thesis, Pt / graphene oxide (Pt / GO), Pt / reduced GO (Pt / 24 h thiourea-treated GO), Pt / 20 min thiourea-treated GO, Pt/ 2 h thiourea-treated GO, and Pt / 5 h thiourea-treated GO nanocatalysts were prepared for methanol oxidation reaction (MOR). The last three ones were synthesized for the first time. They were characterized by FTIR, UV-Vis spectroscopy, acid-base back titration, XRD, XPS, TEM and ICP-MS techniques. Their electrochemical properties and performances toward methanol oxidation reaction were defined by cyclic voltammetry (CV).

FTIR studies indicated thiourea attachment on the surface of GO at the beginning of the treatment, and the reduction of GO in the longer treatment duration. Acid-base back titration exhibited the decrease in carboxyl and hydroxyl functional groups in consistence with FTIR results. XRD data demonstrated that all the prepared catalysts contain face-centered-cubic platinum nanoparticles in an average size of 3-4 nm. TEM images also confirmed this result. XPS analysis revealed that platinum exists in three different oxidation states, Pt(0), Pt(II), Pt(IV) in different ratios in each nanocatalysts.

Electrochemical studies displayed that Pt / 20 min thiourea-treated GO has the highest performance toward methanol oxidation reaction (3.6 times higher than that of commercial E-TEK Pt / Vulcan XC-72 catalyst) due to its highest platinum utility

(~94%), roughness factor (256), chemical (~80 m^2 / g Pt) and electrochemical surface area (~ 75 m^2 / g Pt).

Keywords: Direct Methanol Fuel Cell, Graphene Oxide, Methanol Oxidation, Supported Platinum Nanoparticles, Impregnation Method

ÖZ

TİYOÜRE İLE İŞLEMDEN GEÇİRİLMİŞ
GO NANOPARÇACIKLARI İLE DESTEKLENEN
Pt NANOKATALİZÖRLERİNİN HAZIRLANMASI VE KARATERİZASYONU:
DOĞRUDAN METANOL YAKIT HÜCRELERİNİN
ANODİK SÜRECİNE UYGULANMASI

Karaosmanoğlu, Toprak Seda

Yüksek Lisans, Kimya Bölümü

Tez Yöneticisi: Prof. Dr. Gülsün Gökağaç

Eylül 2017, 127 sayfa

Bu tezde metanol yükseltgenme tepkimesi için Pt / grafen oksit (Pt / GO), Pt / indirgenmiş GO (Pt / 24 saat tiyoüre ile işlemden geçirilmiş GO), Pt / 20 dakika tiyoüre ile işlemden geçirilmiş GO, Pt / 2 saat tiyoüre ile işlemden geçirilmiş GO ve Pt / 5 saat tiyoüre ile işlemden geçirilmiş GO nanokatalizörleri hazırlanmıştır. Son üç nanokatalizör ilk kez sentezlenmiştir. Hazırlanan nanokatalizörler FTIR, UV-Vis spektroskopisi, asit-baz geri titrasyonu, XRD, XPS, TEM ve ICP-MS teknikleri kullanılarak karakterize edilmiştir. Nanokatalizörlerin elektrokimyasal özellikleri ve metanol yükseltgenmesine karşı performansları döngüsel voltametre (CV) kullanılarak tanımlanmıştır.

FTIR çalışmaları işlemin ilk safhalarında GO üzerine tiyoüre tutunuşunu ve uzun işlem süresinde grafen oksitin indirgendiğini göstermiştir. Asit-baz geri titrasyonu da FTIR sonuçlarını destekleyerek karboksil ve hidroksil fonksiyonel gruplardaki azalmayı göstermiştir. XRD verileri eşliğinde katalizörlerin hepsinde 3-4 nm büyüklüğünde yüzey merkezli kübik platin nanoparçacıkların bulunduğu tespit

edilmiştir. TEM görüntüleri bu sonuçla uyum içindedir. XPS çalışmaları her nanokatalizör için Pt(0), Pt(II), Pt(IV) olmak üzere değişik oranlarda üç oksidasyon durumunun olduğunu göstermiştir.

Elektrokimyasal çalışmalar metanol yükseltgenme tepkimesine karşı en yüksek performansın, en yüksek Pt kullanım yüzdesine (~%94), en yüksek pürüzlülük faktörüne (256); kimyasal (80 m^2/ g Pt) ve elektrokimyasal yüzey alanına (75 m^2 / g Pt) bağlı olarak Pt / 20 dakika tiyoüre ile işlemden geçirilmiş grafen oksite ait olduğunu göstermiştir. Bu değer, ticari E-TEK Pt / Vulcan XC-72 katalizöründen 3,6 kat daha yüksektir.

Anahtar Kelimeler: Doğrudan Metanol Yakıt Pili, Grafen Oksit, Metanol Yükseltgenmesi, Platin Nanokatalizör, Emprenye Yöntemi

Dedicated to the memory of Emine Gökağaç

&

Dedicated to the memory of Mine

who is greatly missed

"The highest activity a human being can attain is learning for understanding, because to understand is to be free."

Baruch Spinoza

ACKNOWLEDGEMENTS

TABLE OF CONTENTS

LIST OF TABLES

<p style="text-align:center">LIST OF FIGURES</p>

FIGURES

CHAPTER 1

INTRODUCTION

Since the beginning of history, people have tried to find ways of saving or producing energy. Discoveries aiming at this ways caused significant innovations in the history of civilization. Domesticating animals in order to perform hard labor, simple inventions such as the wheel, use of wood and coal to heat up homes were some of the efforts for saving energy. In fact, we are all energy-dependent. Our respiratory system and food consumption are all for energy production. As our bodies, technological devices require energy to operate.

Nowadays, with the development of industry, we are consuming more and more energy resources, such as coal, oil and natural gas, etc. The limits of these resources are becoming a problem day by day. Energy issues currently cover two areas: one is related to the risk of depletion of fossils and fissile resources; the other is the problem of environmental pollution, such as greenhouse warming and acid rain. The massive use of fossil fuels is in fact unsustainable in the long term; because, as one of the issues, their operating costs will increase considerably due to depletion of fossil reserves; on the other hand, these energies are largely responsible for the CO_2 emissions that causes global warming. It is known that emissions of greenhouse gases have increased gradually.

In view of such issues, reducing pollution in the world (a first step was the Kyoto Protocol signed in 1997), and to look for alternative energy possibilities in the same properties as hydrocarbons has become a necessity. At the plenary meeting of the Intergovernmental Panel on Climate Change (IPCC) in Paris in 2003, the goal of a halving of global greenhouse gas emissions before 2050 was accepted. We must therefore prepare our energy future by making use of the inexhaustible resources and which are called renewable energies. In this context, the use of fuel cells is an attractive solution. This technology directly transforms chemical energy into electrical energy. It is presented as an ecological means of energy production since the only waste that they produce is water. In fact, research on fuel cells has been done for a hundred years.

1.1 Current Energy Context

After the first industrial revolution in the 19th century associated with the advent of steam, the invention of the automobile and aircraft in the 1900s; and, after the more recent advent of electronics, a new energy revolution is inevitable in the 21st century as a result of the gradual depletion of fossil oil resources.
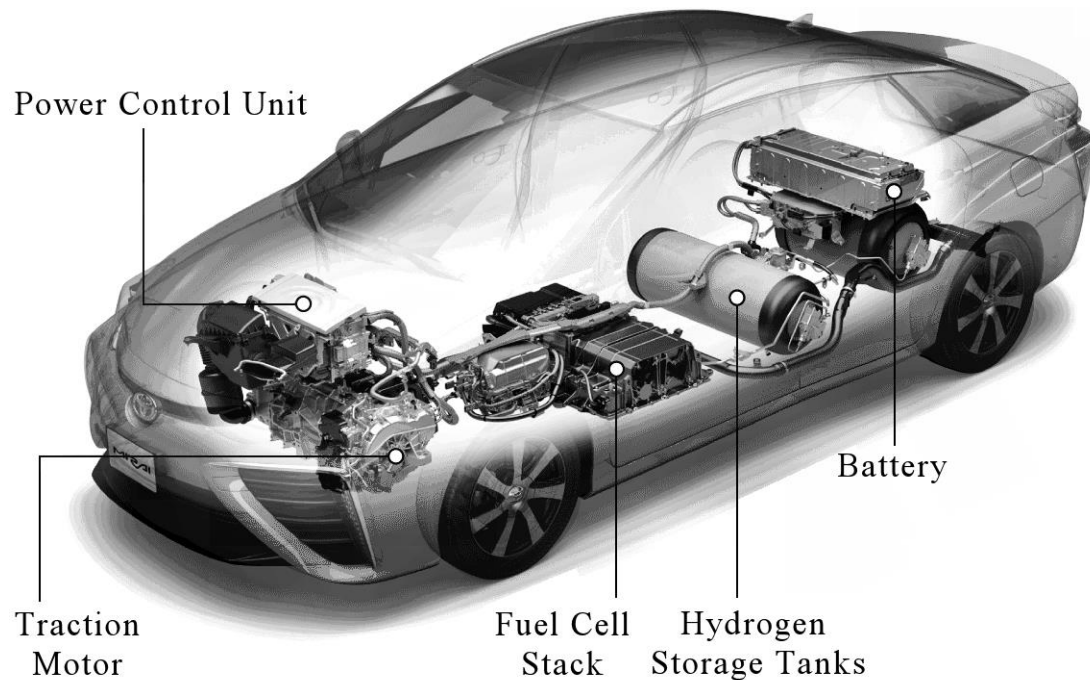
Figure 1.1. Fuel cell prototype vehicles: Toyota Mirai

After the three fossil oil crisis in 1973, 1979 and 2008, industrialized societies have become aware of the dependence of their energy supply on oil which is in finite quantities on the planet. The Western economies are extremely dependent on their hydrocarbon imports from the countries of the Middle East. Another argument that the public is beginning to take into account is the current rise in crude costs. On a more critical and sensitive level, ecological issues begins to be argued more seriously. Indeed, the repeated warnings of climatologists concerning global warming are beginning to challenge the governments and the general public. Their observation is simple: massive emission of CO_2, due to human activities and in particular to the use of hydrocarbons, causes an increase in the greenhouse effect that has critical effects on temperature. In this context, it is not surprising that all major automakers have their prototype of fuel cell powered vehicles. Studies forecast that two million fuel cell vehicles (buses and individual automobiles) will be on the roads until 2020 [1].

1.2 General Description of a Fuel Cell

According to 1st law of thermodynamics, energy cannot be destroyed, but be only transformed [2]. Many of the forms of energy can be transformed to other types of energy.

The conventional process to produce electrical energy, as step by step, is conversion of chemical energy firstly into heat energy; and then, the conversion of heat energy into mechanical energy; and lastly, the conversion of mechanical energy into electrical energy. On the other hand, fuel cell, an open electric power generator, directly converts chemical energy to electrical energy in one step, by basing on electrochemical oxidation reduction (redox) reaction [2].
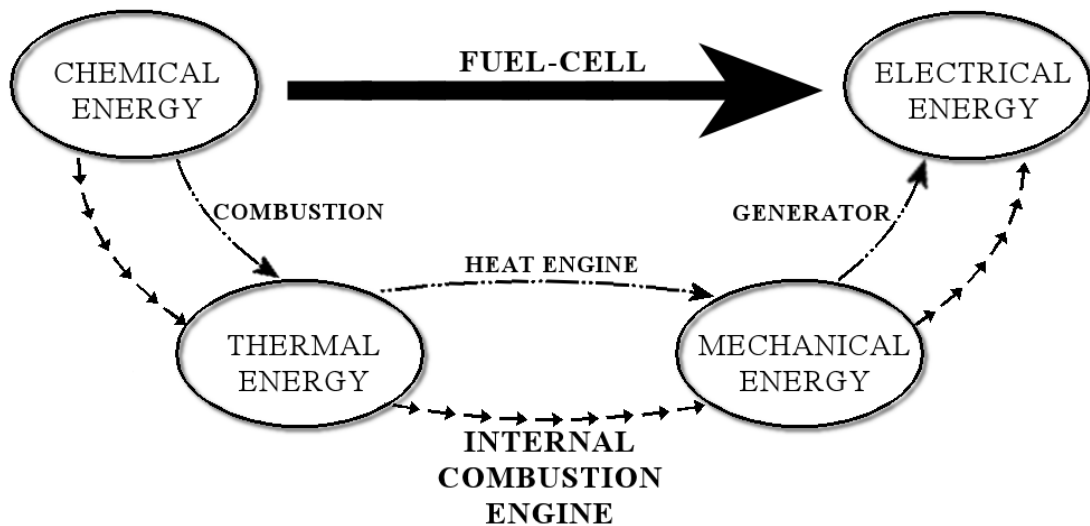
Figure 1.2. Schematic representation of fuel-cell
and internal combustion engine operations

It is a system that produces practically no noise, since it does not have mechanical components in motion, such as turbines and motors. In addition, the electric current is produced as long as the fuel cell is fed with fuel (hydrocarbons, alcohols, biomass, natural gas, hydrogen) and by oxidizing agent (oxygen in the air). This is what distinguishes it from accumulators and other batteries, where a limited amount of electrical energy is stored and which must either be recharged or be replaced. An accumulator is, in fact, a closed system which allows only a limited amount of energy to be supplied, since it contains only a limited amount of reactive within it. Open character of the fuel cells gives them a higher energy density than their competitors, but also a degree of complexity undeniably more marked [3]. They have many significant advantages [4] today:

3

Firstly, they produce very good energy yields. Currently, the conversion efficiency in electrical energy varies according to the type of battery and is generally greater than 50%. Energy not converted into electrical energy is emitted as heat and is discharged as hot water or steam. But while in large power stations heat is lost, here it is rewarding.

Secondly, they are nonpolluting (depending on the fuel used). The environmental qualities of fuel cells and their excellent performance would contribute, where they are used as a replacement for traditional systems, to improving air quality and reducing greenhouse gas (CO_2). For this reason, the use of fuel cells could be an essential contribution to meeting the Kyoto commitments.

Thirdly, they are silent. Their operation is silent unlike engines or gas turbines; only ventilation, converter and circulation of fluids are audible (compressors, pumps, fans). This is a change to reduce noise pollution in cities.

As the forth advantage, they take up little space. Modern technology - miniaturization- has solved a major handicap of the battery: its bulk. This is an advantage for telephones, laptops and other mobile devices.

As another advantage, they can operate at low temperatures. For mobile applications, the temperature inside the engine reaches only 80 °C at the maximum, whereas the core temperature of a diesel engine is more than 1000 °C. The exhaust gas temperature of the fuel cells is much lower than a traditional motor. This advantage increases the number and diversity of applications of fuel cells. Also, they require little maintenance. Since the fuel cell does not cause any movement, there is no wear and therefore no maintenance is required.

On the other hand, being expensive and having low durability are disadvantages of the fuel cells. The cost of the fuel cell is the main obstacle to its commercialization. They require expensive materials such as the platinum catalyst, graphite, the membrane etc.

1.3 Historical Overview

In 1806, Sir Humphry Davy realized the electrolysis of distilled water and obtained hydrogen and oxygen by consuming electricity [5]. It was Christian Friedrich

4

Schoenbein the first one who, in 1838, observed the principle of fuel cells. In his experiment, he used a U-tube with two platinum electrodes. Thanks to an electric current, he could obtain hydrogen and oxygen. By turning off the power supply, he found that the gases produce an electric current in the opposite direction to the first. William Robert Grove met Schoenbein at a conference in Birmingham in 1839. The two men became acquainted with their research. In 1839, Grove demonstrated the principle of the fuel cell [6].
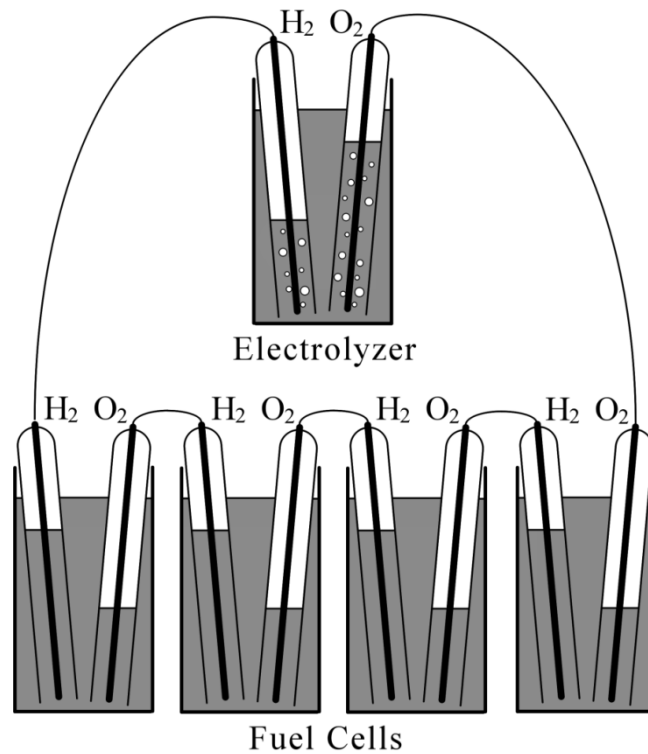
Figure 1.3. Sketch of William Grove's 1839 fuel cell

In the famous experiment, he used U-shaped tubes (Figure 1.3), a hydrogen-oxygen cell with porous platinum electrodes, and sulfuric acid as an electrolyte. A constant current flowed between the platinum electrodes, one end of which was immersed in a sulfuric acid container and the other in sealed containers for collecting oxygen and hydrogen. The sealed containers held water like gases, and he noted that the water level was mounted in both tubes as long as the current was flowing. By combining several sets of these electrodes in a serial circuit, he created what he called a "gaseous battery", to which a name of "fuel cell" was given in 1889 by Ludwig Mond and Carl Langer who have introduced the catalysts (platinum).

After the demonstration of his simple fuel cell, Grove realized that the thin platinum wafers he used as the electrodes had been caused only a thin layer of electrolyte

reaching the electrodes, therefore limiting the reaction. On account of overcoming this, Grove developed an electrode with an improved surface of action by depositing platinum particles onto the platinum electrode, which led to the successful electrolysis of water and preempted the need for high surface area electrodes. In 1882 Lord Rayleigh successfully increased the surface of action of electrodes by using platinum gauze and noticed that coal could be used as a fuel [7].

At the end of the nineteenth century, Ludwig Mond and Carl Langer realized another limitation of this gas battery is that water forming and flooding the electrode surface prohibited prolonged cell performance; and, in 1889 he demonstrated a system using a non-conducting porous material impregnated with the electrolyte, achieving an open circuit voltage of 0.97 V with an efficiency of almost 50% much better than the steam based technology of the time which achieved only around 10% efficiency. They also noticed that they encountered efficiency losses due to the dissipation of the heat from the exothermic reaction into the cell [8].

Meanwhile, Friedrich Wilhelm Ostwald, the physico-chemist who provided much of the theoretical understanding of battery operation, studying the relationship between physical property and chemical reactions, improved the Grove battery [8]. In 1893, he experimentally determined the interactive roles between different components of the battery: electrodes, electrolytes, oxidants and ions, etc. His work in chemistry gave the researchers the foundation of the fuel cell. Later, he also demonstrated that the batteries were more efficient than the internal combustion engine.

Since coal was the only accessible fuel in the nineteenth and mid twentieth century, studies were led into the direct fuel cell which utilized molten salts as the electrolyte. However, this way was relinquished in 1904 when Haber and Bruner [9] notices that the cell reaction was not a carbon reaction at the electrode but rather utilized hydrogen got from an indirect reaction of the coal with the electrolyte. In 1923 Schmid improved the first gas diffusion electrodes for acid electrolyte fuel cells which had both coarse carbon pore and fine platinum pore structures [10]. Between 1912 and 1935, Baur and Brunner studied on high temperature fuel cells for the purpose of utilizing coal gas directly as a fuel source [7]. They examined an entire scope of electrolytes including molten carbonates utilizing less expensive electrode materials; however, the internal resistances remained too high. So, they concentrated

on strong electrolytes such as ceramic; in 1937, the solid oxide fuel cell utilizing a zirconia based electrolyte produced by Nernst was developed by Baur and Preis [11].

In 1946, by basing on the development of Baur and Preis, Davytan created a high temperature cell (700°C) which could run on coal gas and incorporated sodium carbonate with other materials [12]. In 1960, by noticing the fact that the carbonates within Davytan's system became molten at high temperature (550-750°C), Broers and Ketalaar improved a fuel cell utilizing the carbonate materials as an electrolyte within a solid rare earth matrix; so, the molten carbonate fuel cell (MCFC) was born [13]. In the Institute of Gas Technology, Broers' design led to the development of an MCFC using natural gas directly with steam as a fuel source, via a water/gas shift reaction to produce hydrogen, which utilizes platinum electrodes for stability. In 1946, Davytan also studied on the idea of using of aqueous potassium hydroxide (alkaline) as a low temperature electrolyte which had been introduced by Bacon [14] between 1954 and 1974 in the development of the alkaline fuel cell (AFC) as a lightweight power supply used in NASA's Apollo space program. Meanwhile, gas diffusion electrodes were developed by Justi and Winsel, in 1961. Also, carbon electrodes were improved by Kordesch, in 1960 [15]; and Allis-Chalmers developed the electrolyte matrices that immobilized the electrolyte of the AFC in 1962. Then, the electrodes incorporated PTFE for improved water control developed by General Electric (GE), in 1965, which led to an improved AFC used for the orbiter space program. Then, liquid electrolytes caused a problem for the corrosive materials. In order for the fuel cell to be as efficient as the Bacon battery, the electrolyte must be such that the ions pass through it as easily as a flow of electrons. It is later discovered that several stacked cells make it possible to obtain a higher power. The modern fuel cell with a membrane (solid electrolyte with proton exchange membrane / PEM) allowed the application in a stationary or mobile environment [7]. The PEM fuel cell is also referred as solid fuel cell polymer due to the use of the solid electrolyte. The first PEM fuel cell was designed by General Electric in the early 1960s with the work of Thomas Grubb and Leonard Niedrach [16]. PEM fuel cell technology was used as part of the Gemini Project in early 1960. In 1970, DuPont developed the Nafion (polytetrasulfonatedethylene) membrane which is a chemically, thermally and mechanically stable ion exchange polymer, resulted in a revitalization of the PEM fuel cells. A large number of products derived from modifications of Nafion and

other polymers (e.g. sulfonated polyetherketones or SPEK) have appeared in a wide range of cell prototypes [7]. By the incorporation of Nafion into the diffusion electrode structure which led to better transport of ions, the performance of the PEM fuel cell was further enhanced at Los Alamos National Laboratory.

In 1975, advantages of a fuel cell utilizing natural gas directly at low/intermediate temperatures led to the development of the first Phosphoric acid fuel cell (PAFC) operating at 150-200 ^{o}C by the Team to Advance Research for Gas Transformation (TARGET) [7]. On the other hand, following the development of the carbon electrode in 1960, Kordesch posited that alcohols could be used as direct fuel. The direct methanol fuel cell (DMFC) was initially utilized with an acid electrolyte in 1965, as the CO_2 produced by the anodic oxidation reaction could react with an alkali to form a carbonate [17]. Meanwhile, Binder et al studied on noble metals in acidic electrolytes and stated Pt-Ru as the most useful alloy since it could remove some catalyst poisons (e.g. CO). But mixing of the methanol with the acid resulted in a huge amount of methanol diffusion [18]. Consequence of the parasitic reaction at the cathode, it was seen that low molarities of methanol could be used, whereas low power densities and efficiencies were observed. This led to a pause in research on the DMFC until the advent of Nafion and the studies of Jet Propulsion Laboratory on the DMFC in 1992. Since Nafion is solid, the methanol solution could be delivered to the anode not with the electrolyte; however, methanol crossover is still a problem and researches are still being carried out to find a more suitable solid electrolyte.

The very strong development of PEM fuel cell research in the 1970s resulted from the first oil crisis. In 1972, more than 30 research projects were carried out in the United States on the storage of embedded hydrogen or its on-board manufacturing. In the 1980s, the battery technology began to be tested by utilities and car manufacturers. Since then, the object of the research on the fuel cells is at the level of the practical application: the improvement of the performance and the lifetime in use.

1.4 Principle of Operation

The electrochemical reaction uses a proton-conducting solid electrolyte membrane. The electrolyte is sandwiched between two electrodes (the anode and the cathode). The electrodes involve catalysts to activate the reaction on one side. At the anode, ions and electrons are produced by the oxidation of the fuel. The electrons are always

transferred from the anode to the cathode. Then, at the cathode, the electrons allow the reduction of the oxidant (oxygen of the air) and the production of the oxygen ions. Since the electrolyte is a proton conductor, the material allows only the passage of ions. The ions produced on the anode are always transferred from the anode to the cathode. Finally, at the cathode, the ions combine with the oxygen ions to give molecules of water. This relationship corresponds to that of the combustion of fuel and oxygen. The energy of the reaction is released as heat and as electricity. In general, combustion occurs by using a platinum (Pt) catalyst [19].

1.5 Current Fuel Cell Performance

As it is mentioned above, the fuel cell directly converts chemical energy into electrical energy. This chemical process includes two electrochemical half-cell reactions. The general reaction [19] can be defined as:

$$A_{ox1} + B_{red1} \rightarrow C_{red2} + D_{ox2} + \text{electricity} + \text{heat}$$

The released chemical energy can be calculated by the variation of Gibbs' free energy (Δg_f), which is the difference between the energy of the products and the energy of the reagents. Gibbs' free energy is used to calculate the energy available to perform the external work [19]. The variation of the free energy of Gibbs for the fuel cell is:

$$\Delta g_{f} = (g_f)_{products} - (g_f)_{reactants} = (g_f)_C + (g_f)_D - (g_f)_A - (g_f)_B$$

The variation of Gibbs' free energy depends on temperature and pressure as:

$$\Delta g_f = \Delta g^o_f - RT \ln \left(\frac{p_C \cdot p_D}{p_A \cdot p_B} \right)$$

where g^o_f is the variation of the Gibbs' free energy at the standard pressure (1 bar) which depends on the temperature T expressed in Kelvin; p_A, p_B, p_C and p_D are the pressures of products and reactants; R is the universal gas constant (8.31451 J mol^{-1} K^{-1}).

The value of g^o_f is negative since the energy is released by the reaction. If there were no losses in the fuel cell, all Gibbs' free energy would be converted into electrical energy. For each hydrogen molecule, two electrons pass through the external

electrical circuit; and, the electrical work is equal to the variation of the Gibbs free energy if the system is lossless; the electric work performed is:

$$\Delta g_f = -nFE$$

where F is the Faraday constant (96.485 Coulombs / mole) which represents the electrical charge of an electron mole, n corresponds to the number of moles of electrons in the reaction (n = 2 for hydrogen; but this value may be higher for the other fuels, e.g. n = 6 for methanol), E is the open circuit voltage of the fuel cell.

The open voltage of the fuel cell circuit can therefore be written as:

$$E = -\Delta g_f / nF = -\Delta g^o{}_f / nF + \frac{RT}{nF} \ln \left(\frac{p_C \cdot p_D}{p_A \cdot p_B} \right)$$

In practice, the operation of the fuel cells is accompanied by losses; some of the chemical energy is converted into heat. The term $-\Delta g_f/nF$ varies as a function of the operating point of which standard state is 25 ^{o}C and 1 bar. So, according to the equation, the voltage depends on temperature, pressure of reactants [19].

In fact, the voltage of a fuel cell depends on thermodynamic quantities. According to the first principle of thermodynamics, the internal energy U of a system is the sum of a quantity of heat (Q) and a work (W) [20-22]. For an elementary transformation, we have:

$$dU = \delta Q + \delta W$$

If, moreover, a reversible transformation is considered in which only the forces of pressure are involved, $\delta Q = TdS$ and $\delta W = -pdV$. The equation then becomes:

$$dU = TdS - pdV$$

where S is the entropy function. The (S) entropy of a system is a state function that can be interpreted as measuring the degree of system disorder at the microscopic level. According to the second principle of thermodynamics, the entropy of an isolated system cannot diminish; but it increases or remains constant if the transformation is reversible [20-22].

The Gibbs energy G, also called free enthalpy, is a state function which follows the relation:

$$G = H - TS$$

where H, T and S are the enthalpy, temperature, and entropy respectively. For a reversible reaction at constant temperature, the free enthalpy change ΔrG, also known as free enthalpy of reaction, characterizes the part of the enthalpy which can be exchanged outdoors as work, the other part being dissipated as heat TΔS:

$$\Delta_r G = \Delta_r H - T\Delta_r S$$

In a differential form, it can be expressed as:

$$dG = Vdp - SdT$$

The Faraday equation connects the free enthalpy of reaction ΔrG^o with the reversible voltage E_0 of a fuel cell at equilibrium, that is to say when it does not supply current. Also as known as no-load voltage, E_0 is defined in the standard state (e.g. at a pressure of 1 bar):

$$E^0 = -\Delta rG^o / nF$$

where n is the number of electrons involved in the overall reaction, and F is the Faraday constant (96.485 Coulombs / mole).

1.5.1 Influence of Temperature

The entropy at constant pressure can also be expressed in the form:

$$S = \left(-\frac{\partial G}{\partial T}\right)_p$$

According to the Faraday equation and knowing that the vacuum voltage depends only on the temperature, we have:

$$\left(-\frac{\partial \Delta_r G}{\partial T}\right)_p = nF\frac{dE}{dT}$$

which can be expressed as:

$$(\Delta_r S / nF) = (dE/dT)$$

During its operation, a fuel cell yields heat to the environment (TΔS<0). Therefore, the reversible potential of the cell decreases as the temperature increases (dE/dT <0).

11

However, this observation is valid for a reversible system: the potential of a real battery in operation is degraded by the irreversibility which can decrease with the increase of the temperature. This is the case of the irreversibility caused by the activation energy required for the reactions [22, 23].

1.5.2 Influence of Pressure

Considering the following electrochemical reaction:

$$v_A \text{ A} + v_B \text{ B} \Leftrightarrow v_C \text{ C} + v_D \text{ D}$$

where A and B are the reagents, C and D the products; va, vb, vc and vd the stoichiometric coefficients; the Nernst equation is written:

$$E = E^o - \frac{RT}{nF} \ln \left(\frac{(a_c)^{v_c} (a_D)^{v_d}}{(a_A)^{v_a} (a_B)^{v_b}} \right)$$

such that represents the activity of the various components. By applying the Nernst equation to the global reaction of $A_{ox1} + B_{red1} \rightarrow C_{red2} + D_{ox2}$, it is obtained that:

$$E = E^o - \frac{RT}{nF} \ln \left(\frac{a_C \, a_D}{a_A \, a_B} \right)$$

For gases, the activity is equal to the partial pressure p. It can then be noticed that the voltage supplied by the cell increases with the partial pressure of the reactive gases. However, this growth is logarithmic. In this context, for direct methanol fuel cells, besides cell temperature, oxygen gas or air pressure in cathodic process has also an effect on the power performance [22, 24].

1.5.3 Polarization Potentials

The highest output voltage of fuel cells is achieved at open circuit (no load) conditions and the voltage drops off with increasing current draw, which is known as polarization [20, 21]. The actual open circuit voltage of a fuel cell is lower than the theoretical model due to species crossover from one electrode through the electrolyte and internal currents. For instance, usually, the open circuit voltage of a polymer electrolyte DMFC is significantly lower than the thermodynamic or reversible potential for the overall process. This is mainly the result of methanol crossover

causing a mixed potential at the cathode and of the irreversible adsorption of intermediate species at electrode potentials close to the reversible potential. The coverage of methanol species is large at high cell potentials, that is, at low anode potentials. This is assign to a strong anode activation control that reflects on the overall polarization curve. Fuel crossover losses are the losses that result from the waste of fuel passing through the electrolyte and electron conduction through the electrolyte. This loss is typically small, but can be more significant in low temperature cells. The performance of a fuel cell is interpreted from the polarization curve which represents the intensity-potential characteristics of the cell. The profile of this curve represented in Figure 1.4 is the consequence of a set of phenomena.
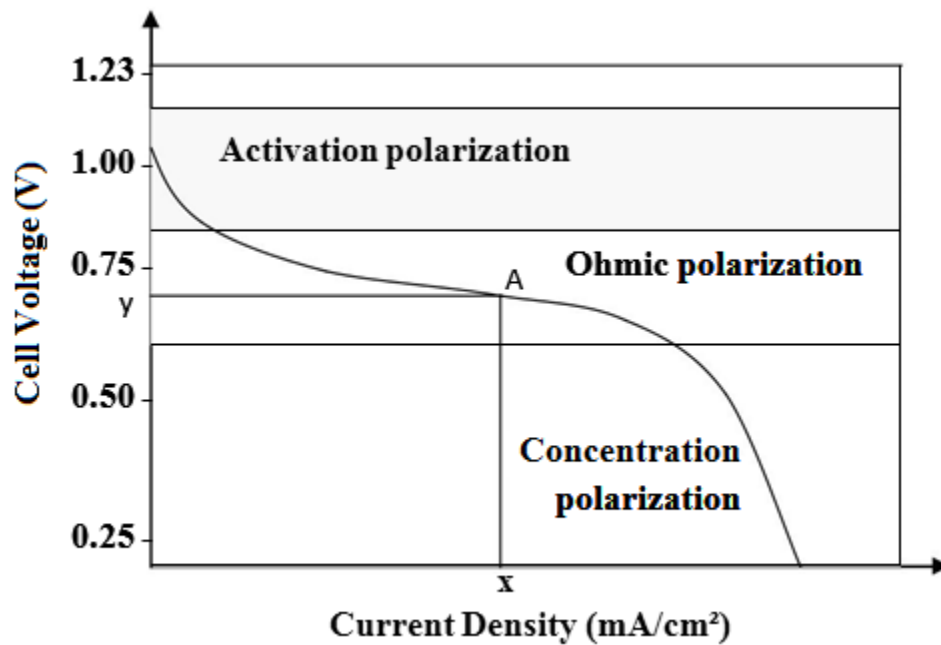
Figure 1.4. Schematic representation of the polarization curve of a FC

The bias potentials of a fuel cell represent the voltage losses generated by the irreversibility of the system [20-22]. The effective voltage U of a working battery is given by the reversible voltage from which the polarization potentials are subtracted:

$$U = E - E_{act} - E_{ohm} - E_{conc}$$

Three forms of polarization can be distinguished as:

(I) Activation Polarization (E_{act}): For an electrochemical reaction to occur, the reactants must overcome an activation barrier. Activation polarization corresponds to

13

losses due to catalytic activation. It depends on the nature and surface of the catalyst. Activation overvoltage (η_{act}) is described by the following general equation, where α is the electronic transfer coefficient, i is the current flowing through the cell and i_0 is the exchange current.

$$\eta_{act} = \frac{RT}{\alpha nF} \ln \left(\frac{i}{i_0} \right)$$

(II) Ohmic Polarization (E_{ohm}): It is caused by the ohmic losses due to the electrical resistance of the various elements of the battery. The ohmic polarizations or ohmic drops are due to the resistance that the ion flux encounters when passing through the electrolyte and to the resistance that the electrons encounter in the electrodes and in the electrical circuit. The ohmic losses are mainly due to the electrolyte. A membrane with a good conductivity makes it possible to limit these losses; and therefore, obtain for this curve a very small slope in Figure 1.4. The electrolyte obeys the law of ohm, the ohmic drops can be expressed by the following equation, where R is the total resistance of the cell and i is the current flowing through the cell.

$$\eta_{ohm} = Ri$$

(III) Concentration Polarization (E_{conc}): It is caused by the concentration variation of the reagents on the electrode. When there is a loss of potential due to the inability of the system to maintain the initial concentration of the reactants, a concentration gradient formation is then produced. Many factors can contribute to concentration polarization (η_{conc}), including low gas diffusion through porous electrodes, diffusion of reagents from the reaction site to the electrolyte, high current densities, supply catalytic sites in reagents being no longer sufficient and the low rate of transport of the reactants or products to the reaction site is the major contribution of the concentration polarizations. The appearance of this zone can be delayed by the improvement of the diffusion layers, the increase in the gas flow rate, etc. The concentration overvoltage is expressed by the following relation:

$$\eta_{conc} = \frac{RT}{nF} \ln \left(1 - \frac{i}{i_L} \right)$$

Where, i_L is the diffusion limiting current and i is the current flowing through the cell. The theoretical potential (E_{theo}) in a fuel cell obeys the Nernst law [20-22].

However, as it was mentioned before, the real potential of a fuel cell decreases with respect to the ideal equilibrium potential, due to losses called "polarization" or "overvoltage". Thus, the fuel cell produces a real potential (E) less than the theoretical potential, as the following equation:

$$E = E_{theo} - losses$$

The real potential of a fuel cell decreases with respect to the Nernst potential due to potential losses with respect to polarization or overvoltage phenomena which are of three types: activation polarization, ohmic polarization and concentration polarization.

Figure 1.4 shows a current voltage characterization of a PEMFC. The potential varies according to the current density. According to this figure, at low current density, the activation polarizations are dominant. At medium current density, the ohmic polarizations become preponderant over a wide range of current density. Whereas at high current density, concentration polarizations due to gas transport become dominant.

1.5.4 Activation Potential

Briefly, the efficiency of a fuel cell is directly related to the rates of reactions occurring at the anode and the cathode. Since the oxidation of fuel is naturally slow reaction, an acceleration of it is necessary to optimize the operation of a fuel cell.

The empirical law of Arrhenius used in chemical kinetics makes it possible to describe the variation in the speed of a chemical reaction [20-22]. This reaction rate is a function of the reaction temperature and the activation energy Ea:

$$k = A \exp(\frac{-E_a}{RT})$$

where k is the rate constant and A is a function of the reaction. Thus, it can be seen that a rise in temperature makes it possible to increase the reaction rate. On the other hand, by decreasing the activation energy necessary to initiate the reaction, the rate constant is also increased. The role of the catalyst is precisely to reduce this activation energy. Because of its physicochemical properties (malleability, conductivity and chemical stability), platinum is one of the most commonly used

catalysts in fuel cells, particularly those of the PEM type [20-22]. It is incorporated into a support (carbon powder for example) in the form of fine particles and then deposited on the electrode. Each catalyst particle then forms an active site, the seat of the electrochemical reactions. More precisely, the reactions occur at the catalyst / carbon / electrolyte interface, also known as the triple phase boundary (Figure 1.6).

1.5.5 Efficiency

The thermal efficiency of a fuel cell is defined as the amount of useful energy produced relative to the change in stored chemical energy released when a fuel is reacted with an oxidant, which is in general referred as thermal energy [4, 24]. Therefore, the efficiency is defined as:

$$\eta_e = \text{usefull output energy} / \Delta H$$

In the ideal case of an electrochemical energy conversion reaction such as a fuel cell, the change in Gibbs free energy of the reaction can be expressed as useful electric energy at the output of the device. Hence, the ideal efficiency of a fuel cell operating irreversibly can be stated as:

$$\eta_e = \Delta G / \Delta H$$

As explained above, the actual cell voltage is less than the ideal cell voltage due to the losses associated with cell polarization and the iR loss. Hence, the efficiency of an actual fuel cell can be expressed in terms of the ratio of the operating cell voltage to the ideal cell voltage [4, 24]:

$$\text{Energy conversion efficiency} = E_{op} / E$$

1.6 Main Components of the Fuel Cell

1.6.1 Membrane

The membrane, or electrolyte, is a key element of the fuel cell system. Its role is multiple and the performance of the fuel cell depends strongly on its mechanical, electrical and chemical characteristics. It has to perform several functions such as electrically insulating the anode from the cathode while ensuring the conduction of the protons, and effectively separation in order to avoid direct contact of the fuel and

of the oxidizing gas [19]. Its insulating character is very important because any electron that can pass through it directly results in reagent consumption without current generation, which has the consequence of reducing the overall electrical efficiency.
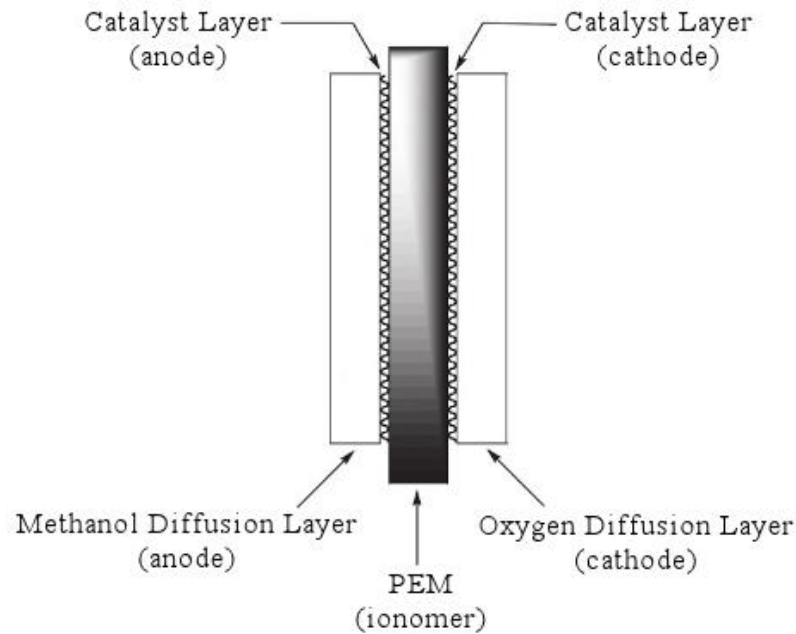
Figure 1.5. Schematic of membrane electrode of DMFC

A typical DMFC contains two flat electrodes with a thin layer of membrane electrode assembly (MEA) in the middle. The membrane electrode assembly is the key component of DMFC and comprise of a catalyst layer and a diffusion layer for both anode and cathode [25]. Figure 1.5 represents the membrane electrode of Direct Methanol Fuel Cells.

1.6.2 Electrodes

In general, the electrodes are constituted by a carbon felt or carbon paper whose face in contact with the electrolyte is coated with a paste containing platinized carbon, polytetrafluoroethylene (PTFE) and a proton conductive polymer electrolyte [19].

The Gas diffusion electrode (GDE) of a DMFC is composed of several layers each with a different composition. The diffusion layer is generally composed of carbon and polytetrafluoroethylene (PTFE) [26]. It ensures the structure onto which the following layers are fabricated and provides mechanical strength to the electrode. Its porous structure allows reactants to transport freely to the active electrode area

(catalyst) and allows products (CO_2 in anode and H_2O in cathode) to exit from the reaction sites, which increases the performance of the cell. It also constitutes the electrical connection between the active layer and the bipolar plate. It must therefore be a good conductor of electrons. Its components must have good chemical inertia in the acidic and corrosive medium of the fuel cell. This is why carbon is generally used as the main component in this layer [26-28]. The active layer also called as catalyst layer is the site of the electrochemical reactions take place. Catalyst metals are finely dispersed on a support material (usually carbon) having higher surface area, which increases the active surface area of a catalyst [27]. They both needs to have good contact with the membrane material in order to provide protons an adequate mobility; and to achieve this, they are dispersed in an electrolyte solution as forming a triple phase boundary around the catalyst to allow the effective transport of protons through the PEM. The triple phase boundary lies between the fuel (CH_3OH) supply, the electrolyte and the electrode (between the catalyst and ionic conductor). The oxidation and reduction reactions can take place only in these confined spaces where protons, reactive fuel, electrons and catalyst are combined as shown in Figure 1.6.
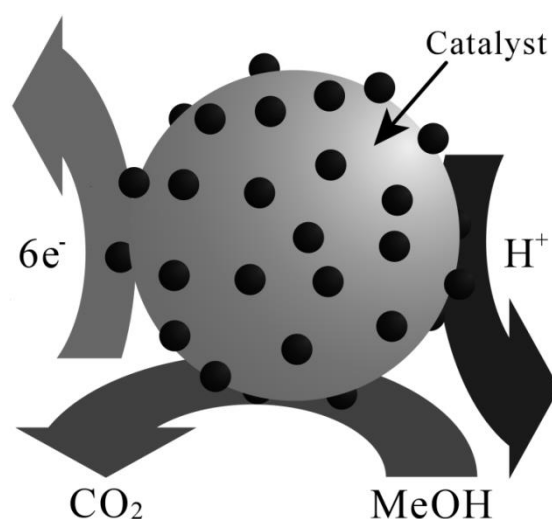
Figure 1.6. Schematic representation of the triple phase boundary of DMFC

1.6.3 Bipolar Plates

Bipolar plates (Figure 1.7) play the role of an electronic conductor between the electron-producing anode and the electron-consuming cathode of the neighboring cell. They contain a flow field responsible for the fuel feed and removal of effluent from the fuel cell. They are usually made of graphite [19].

18
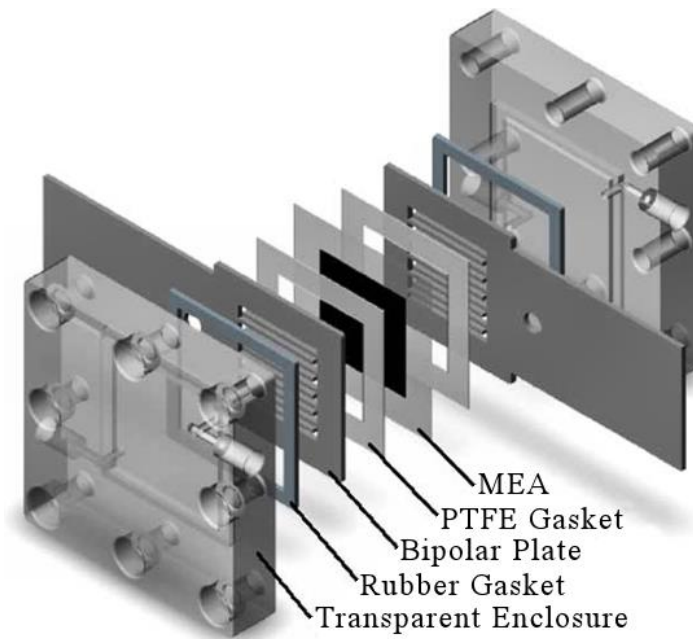
Figure 1.7. Bipolar plates in-house fabricated transparent DMFC

1.7 Types of Fuel Cells and Their Applications

There are different types of fuel cell that are typically differentiated by the nature of their electrolyte [4, 19]. An exception in this classification is the DMFC (Direct Methanol Fuel Cell) type which is actually a PEMFC (Proton Exchange Membrane Fuel Cell), but using methanol as fuel which is directly sent to the anode. Another characteristic used to classify the batteries is their operating temperature. There are two categories of fuel cells: high-temperature fuel cells operating at temperatures above 600 °C and those operating at temperatures below 200 °C. The low-temperature types are PEMFC, DMFC, AFC (Alkaline Fuel Cell), FAFC (Formic Acid Fuel Cell), DBFC (Direct Borohydride Fuel Cell) and PAFC (Phosphoric Acid Fuel Cell); whereas high temperature types are SOFC (Solid Oxide Fuel Cell) and MCFC (Molten Carbonate Fuel Cell) operating between 600 and 1000 °C [4, 19].

High-temperature and medium-temperature (600-1000 °C) fuel cells such as SOFC and MCFC have several advantages. They eliminate the use of expensive, precious metal catalysts. High operating temperatures offer the possibility of using the heat produced in the form of steam for district heating, industrial processes or cogeneration, ie the use of a steam turbine to produce heat, electricity. A disadvantage of high-temperature fuel cells is long start-up time. The rise in temperature is ensured by auxiliary sources until the operating temperature is

reached. This complicates any use in short and repetitive cycles. In addition, the components must withstand these very high temperatures and the corrosive medium of the battery in operation. The materials suitable for these conditions are expensive.

1.7.1 The Solid Oxide Fuel Cell (SOFC)

The operating principle of SOFCs is based on the following mechanism: oxygen is dissociated at the cathode at O_2, and then the anion migrates through the ion conductive electrolyte at high temperature and will combine with the anode with hydrogen, or carbon monoxide, to form water and release electrons [29].

At the anode, with a zirconium and nickel cermet catalyst, the reaction is carried out:

$$2H_2 + 2O_2^- \rightarrow 2H_2O + 4e^-$$
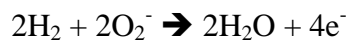
At the cathode, in both cases, with the aid of a strontium-doped manganite catalyst, the reaction is carried out:

$$O_2 + 4e^- \rightarrow 2O^{2-}$$
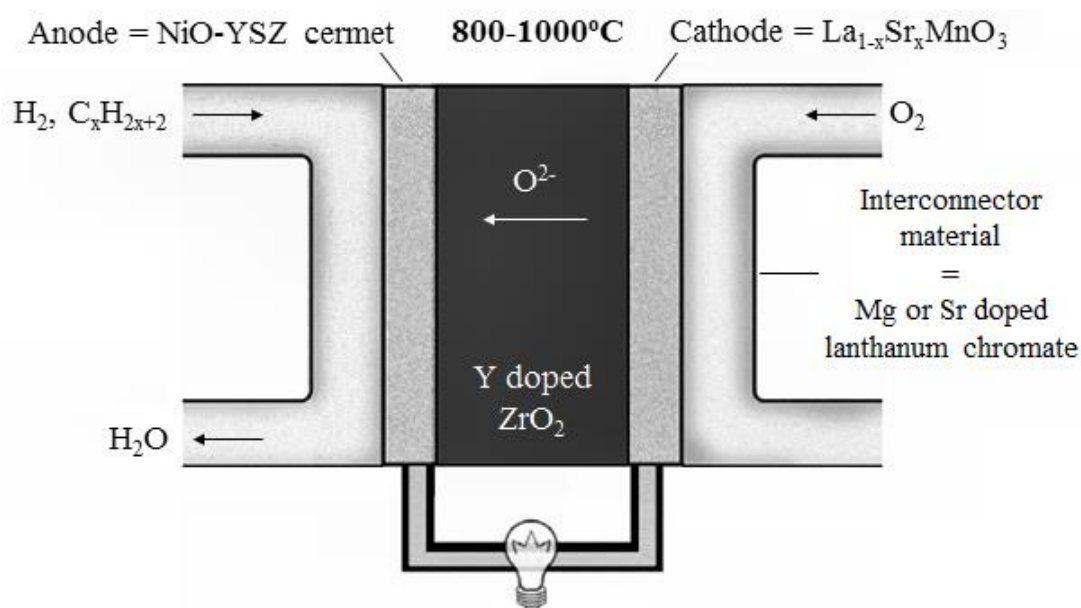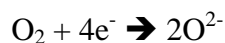
Figure 1.8. Schematic representation of SOFC

The main characteristic of the SOFCs therefore lies in their high operating temperature (600 to 1000 °C) necessary to obtain a sufficient ionic conductivity of the ceramic electrolyte. This temperature has two main advantages. Firstly, it allows the direct use of hydrocarbons, which can be easily reformed without a catalyst based on noble metals. It also produces high heat easily exploitable in cogeneration; the

efficiency can thus reach 80% [19, 29]. Since they are not poisoned by carbon monoxide that can even be used as fuel, it can utilize natural gas, biogas, and gases made from coal. Slow startup and requirement significant thermal shielding to retain heat are disadvantages. The high operating temperatures also cause a requirement for increased durability of materials.

SOFC technology is particularly well suited for decentralized power generation and cogeneration (ranges from 1 kW to a few tens of MW). The development of this type of battery implies, through this high operating temperature, the solving of thermomechanical problems of resistance to relatively complex materials, as well as assembly and sealing.

1.7.2 The Molten Carbonate Fuel Cell (MCFC)

The development of molten carbonate fuel cells began in the mid-twentieth century. The advantages and disadvantages of this type of battery are substantially the same as in the case of SOFCs [19]. The high temperature greatly improves the kinetics of the oxygen reduction reaction and thus renders the use of noble metals as catalysts unnecessary.

MCFC battery-based systems can achieve efficiencies in excess of 50%, or even more than 70% when combined with other generators. In addition, MCFCs can use a wide range of fuels, and are not sensitive to CO or CO_2 contamination as is the case with low temperature fuel cells [19, 30]. The reactions taking place are as follows: At the anode, with a catalyst made of a nickel-chromium / nickel-aluminum alloy, the reaction is carried out:

$$2H_2 + 2CO_3^{2-} \rightarrow 2H_2O + 2CO_2 + 4e^-$$
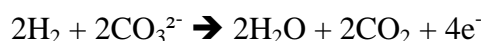
At the cathode, with a nickel oxide catalyst, there are:

$$O_2 + 2CO_2 + 4e^- \rightarrow 2CO_3^{2-}$$
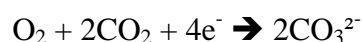
The electrolyte is made of a mixture of alkali metal carbonates (lithium, potassium and sodium carbonates) retained by a ceramic matrix of aluminum oxide and lithium ($LiAlO_2$) [19, 30]. Bipolar plates are made of nickel-coated stainless steel on the anode side. The choice of materials is extremely important, due to the highly corrosive nature of the electrolyte and the very high operating temperature.

21
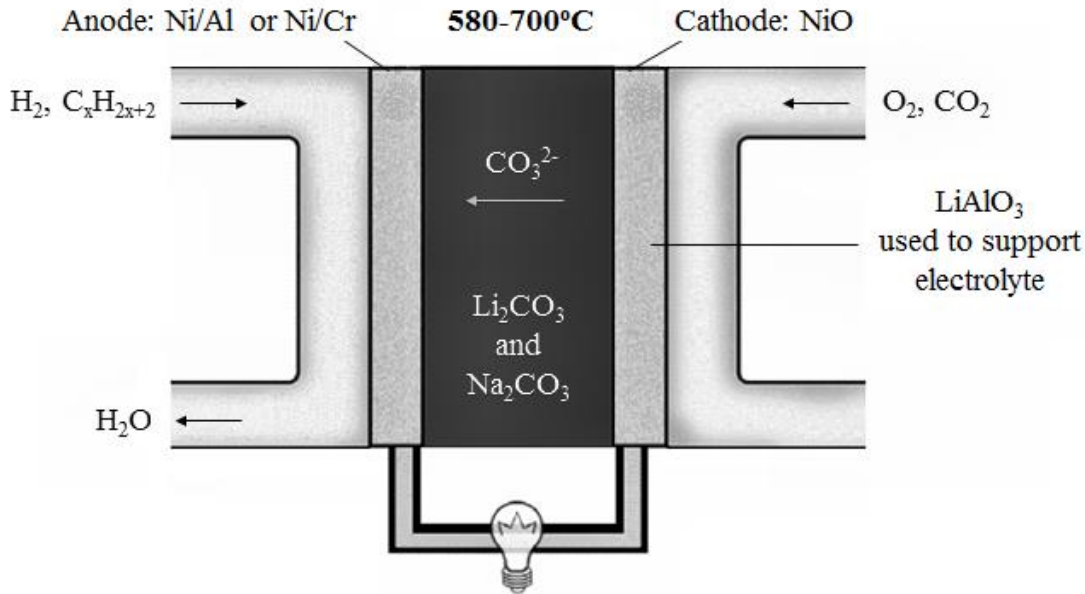
Figure 1.9. Schematic representation of MCFC

1.7.3 The Phosphoric Acid Fuel Cell (PAFC)

The phosphoric acid fuel cell is the most advanced system in development and commercialization. It is mainly used for stationary applications, as an electric generator. PAFC power plants, with a power supply between 5 and 20 MW [19], have been installed in different locations around the world to supply electricity, heating and hot water to some villages, factories or hospitals.

The advantages of PAFCs are their ease of manufacture, their thermal and chemical stability and the low volatility of the electrolyte at operating temperatures (between 150 and 220 °C). These factors have facilitated the commercial development of this type of system. The reactions occurring in a PAFC are the same as in the case of PEMFC, with operating temperatures varying from 150 to 220 °C. At the anode:

$$2H_2 \rightarrow 4H^+ + 4e^-$$

at the cathode:

$$O_2 + 4H^+ + 4e^- \rightarrow 2H_2O$$
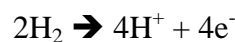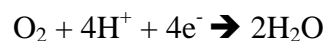
The components of the two fuel cells (PAFC and PEMFC) are very similar except for the electrolyte. In the case of PAFC, the electrolyte is phosphoric acid (also a proton-conducting electrolyte), a liquid, whereas it is a solid polymer in the case of PEMFC [30, 31]. At the beginning of the development of the PAFCs, phosphoric

22

acid was used in solution in order to limit the corrosion of certain constituents of the cell. But with the progress made in the materials used for fuel cell construction, the acid concentration is now 100% [19, 30].

The high acid concentration increases the conductivity of the electrolyte and reduces the corrosion of the carbon electrode support. As in the case of PEMFCs, this cell uses carbon electrodes, with a platinum-based catalyst, which allow the diffusion of gases [31]. The bipolar plates are two porous plates separated by a thin sheet of graphite to form a substrate in which the electrolyte can be stored. Other catalysts are being tested for this type of fuel cell: iron-cobalt, titanium, chromium, and zirconium.
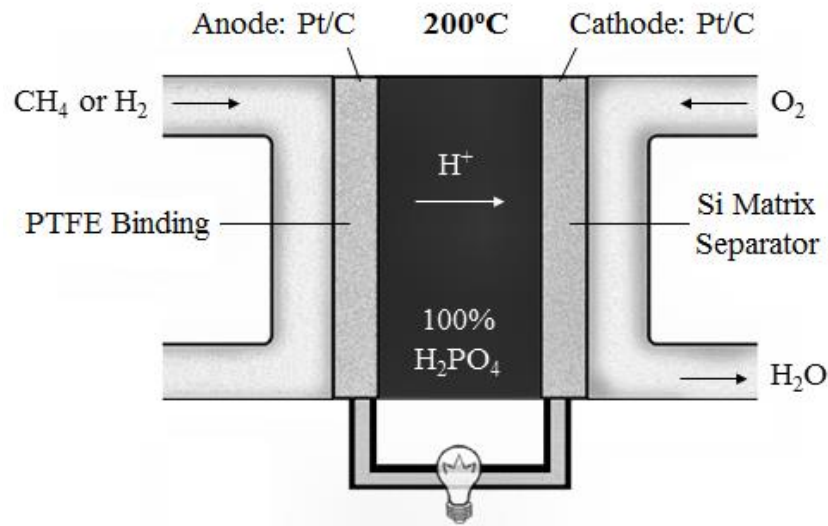
Figure 1.10. Schematic representation of PAFC

On the other hand, the low temperature batteries, 60 and 200 °C, allow a fast start, a great flexibility of operation and a good thermal management. Low temperatures also allow a wider choice of materials. Since the operating temperature is low, the presence of catalysts is essential for the reaction rate to be acceptable. These catalysts are based on precious metals (silver, platinum, and palladium). They are also very sensitive to the presence of poisons such as carbon monoxide present in small quantities in the fuel, which inhibit the activity of the catalyst. This involves extensive purification of the fuel and oxidizer to remove CO.

1.7.4 The Polymer Exchange Membrane Fuel Cell (PEMFC)

Polymer Exchange Membrane Fuel Cells have been the subject of intensive research since the 1990s to reduce their cost [19]. Indeed, their potential is not negligible

because they are versatile. They can also be used for transport, stationary and even for portable technologies [33]. In this type of cell the electrolyte is a proton-conducting polymer membrane. The presence of diffusion plates, also called bipolar plates are characteristic.

The function of the electrolyte is to conduct the H^+ protons to ensure the passage of electrical charges into the cell. The membrane is sealed with dihydrogen and dioxygen and prevents the passage of electrons inside the battery. Its thickness may be of the order of ten microns, which favors the passage of protons. These protons need water to circulate. Thus the membrane must be precisely moistened so as not to impair the operation of the cell. Indeed, a dry membrane will not be a good conductor and will wear, conversely a membrane too wet will risk drowning the electrodes. Currently, the PEMFC type batteries have a Nafion membrane. The PEMFC electrolytes operate at temperatures between 60 and 90 °C at pressures between 1 and 5 bar [32, 33].

The electrodes have a complex geometry. Indeed, they must contact the reagents, the electrolyte and an electronic conductor. They are both covered with Platinum [34]. The purpose of this catalyst is to promote the oxidation reaction of pure or reformed H_2, which is the fuel of the cell, and of reducing the oxygen contained in the air. The air is, in this case, the oxidant. The reaction at the anode:

$$H_2 \rightarrow 2H^+ + 2e^-$$

at the cathode:

$$\frac{1}{2} O_2 + 2H^+ + 2e^- \rightarrow H_2O$$
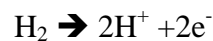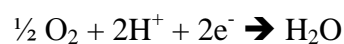
The electrodes found today are composed of carbon particles having a diameter of between 20 and 50 nm. Platinum particles are then deposited thereon, the diameter of which varies between 2 and 4 nm [34]. The platinum content is generally in the order of 0.2 mg/cm². The functioning of PEMFCs may be altered due to the catalyst. This is since it absorbs the carbon monoxide which has not been removed during the purification process.

PEMFCs are also composed of diffusion plates. They surround the electrodes and serve to allow diffusion of gases to the electrodes, the transfer of electrons, and they manage water by evacuating or moistening the membrane. These plates are made of

a carbon fiber substrate which is coated with graphite and a hydrophobic polymer: PTFE. Thus, the diffusion plates are porous and conductive. Bipolar plates serve to collect current and separate the gases at the anode and the cathode. They are generally composed of graphite sheets, composite or carbon-based metals [32, 33]. Indeed, this allows the bipolar plates to be good electrical conductors and to be impermeable to gases.
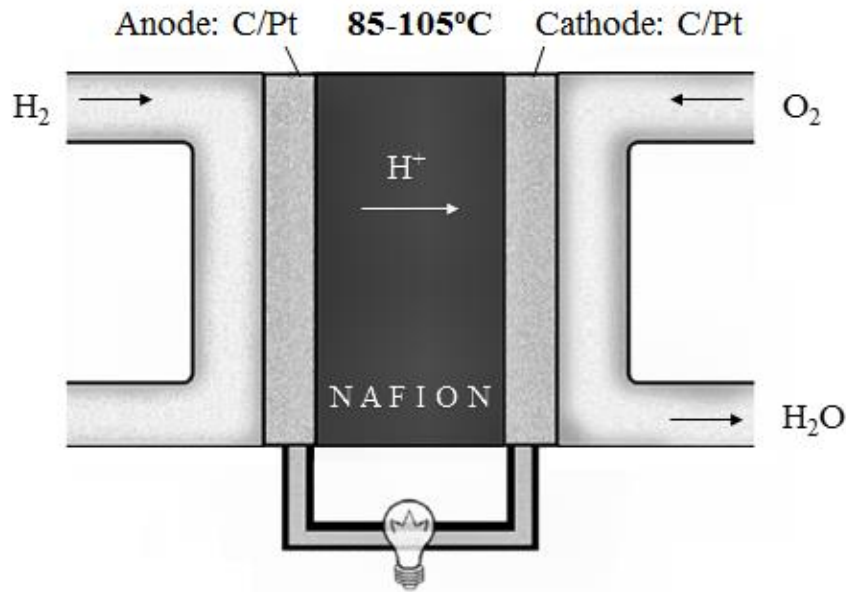
Figure 1.11. Schematic representation of PEMFC

Transport has been the field of application for the development of fuel cells since the early 1990s. Among the different fuel cells studied, at present, the PEMFC proton polymer membrane is probably the most suitable to the automotive applications and the most promising due to its low operating temperature, its simplicity of manufacture, its better reactivity, and its good efficiency to the powers below the maximum power. Hydrogen-powered vehicles are currently in circulation; and, General Motors, Toyota, Honda, Daimler and Hyundai are planning a first commercialization by 2015.

1.7.5 Alkaline Fuel Cell (AFC)

They consist of a liquid electrolyte which is generally a solution of potassium hydroxide (KOH) with a concentration ranging from 30 to 40% [19]. This electrolyte provides conduction of the OH^- ions. The hydroxide ions of the electrolyte can react with the carbon dioxide of the air, for example according to the following reaction:

$$CO_2 + 2OH^- \rightarrow (CO_3)^{2-}$$
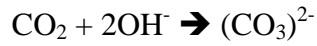
This reaction will lead to a reduction in the conductivity of the electrolyte. This is why it is necessary to work with pure gases and not with air or reformed gases [35]. These pure gases constitute the oxidants.

The catalysts for the oxidation reaction of hydrogen are generally composed of nickel and an inactive metal such as aluminum, which makes it possible to reduce the costs. Platinum-Palladium catalysts are also found [36]. The fuel of this cell is therefore dihydrogen. The catalysts for the reduction of oxygen are either silver or platinum-gold. The reaction at the anode:

$$H_2 + 2OH^- \rightarrow 2H_2O + 2e^-$$

at the cathode:

$$\frac{1}{2} O_2 + H_2O + 2e^- \rightarrow 2OH^-$$
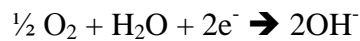
The plates used for the interconnection are made of nickel or stainless steel [19]. Its operating temperature of the electrolyte is between 60 and 90 ° C. However, if the pressure is increased, the operating temperature also increases. This makes it possible to work at higher temperatures.

Due to the normal operating temperature and elimination of the storage problem, this study interested in (the anodic part of) DMFC explained in the following section.
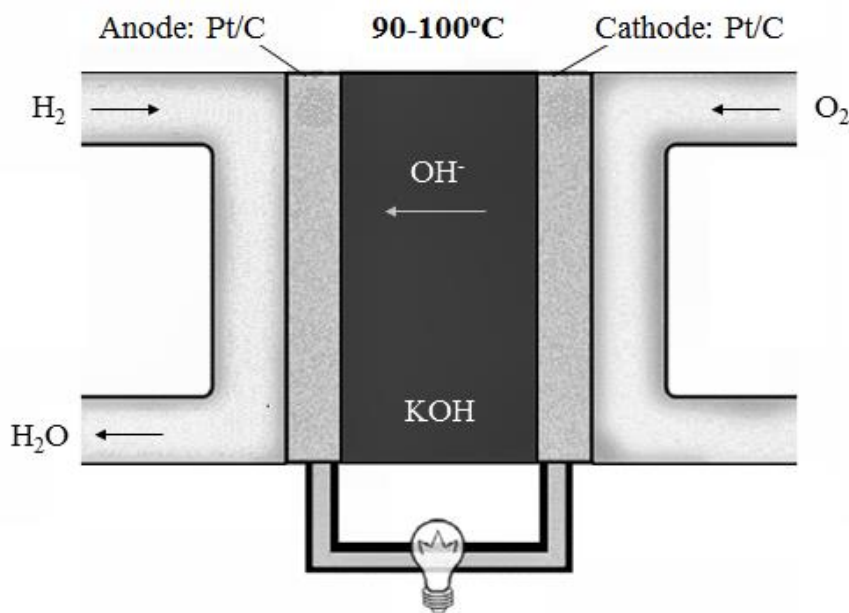
Figure 1.12. Schematic representation of AFC

26

1.8 Direct Methanol Fuel Cell (DMFC)

The DMFC is a fuel cell with a proton exchange membrane fed directly with methanol (CH_3OH). Methanol is one of the few reagents with hydrogen (as well as glycol, ammonia or hydrazine) that has sufficient oxidation characteristics to be able to be used in low-power fuel cells and at normal temperature. Methanol liberates six protons and six electrons per molecule throughout its oxidation. Its high energy density makes methanol an ideal fuel for fuel cells (DMFC) that work under low-temperature conditions and are fueled mainly with methanol diluted in water.

It is a relatively new type of fuel cell and many significant improvements have already been made in recent years in terms of power, efficiency, and lifetime [37-39]. The decisive advantage over PEM fuel cells is that they operate directly with methanol which is liquid at normal temperature and currently produced from natural gas (it is also possible from oil, coal or biomass) and which can benefit from the existing infrastructure for gasoline. The problem of reforming and / or storing hydrogen is thus dispensed with.

The fuel is a mixture of water and methanol reacts directly in the anode according to the following reaction:

$$CH_3OH + H_2O \rightarrow CO_2 + 6H^+ + 6e^-$$
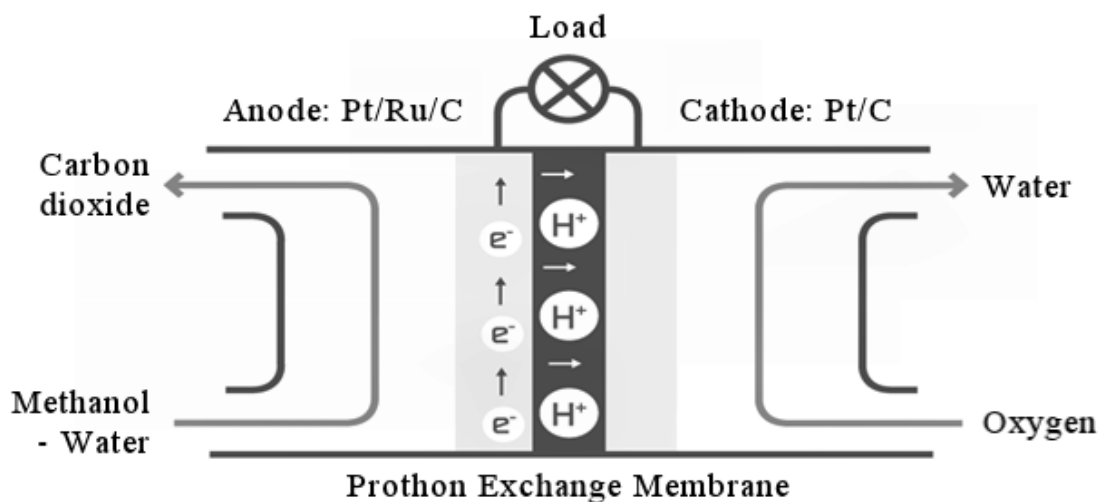
Figure 1.13. Schematic representation of DMFC

The two catalytic electrodes where oxidation of methanol (anode) and reduction of oxygen (cathode) occur are separated by a membrane which conducts the protons from the anode to the cathode, while the other inverse diffusion is inhibited. The set

of electrodes and membranes is called membrane electrode assembly (MEA) as represented in Figure 1.14. Each electrode is made of a gas diffusion layer and a catalytic layer [26-28]. The MEA consists of five layers: A proton exchange membrane (PEM), two layers of catalysts, and two diffusion layers.
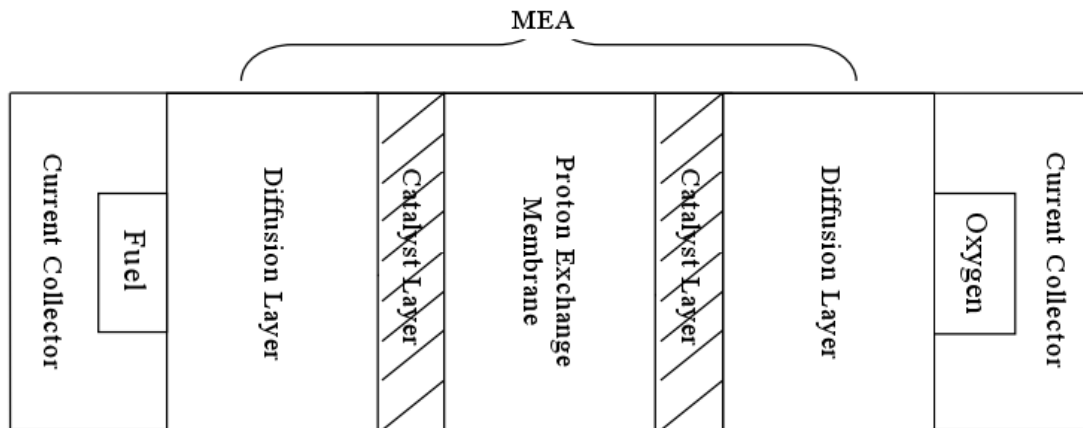
Figure 1.14. Basic building blocks of a typical DMFC

Advantages of DMFC over the conventional battery are its greater energy density, independence of the electrical network, being instantly rechargeable. Advantages over the other fuel cells are that fuel liquid does not require reformatting, operation at room temperature, quick start, and good response to change of power. Furthermore, methanol is much less polluting, 97% less polluting than gasoline. It can therefore be said that from an environmental point of view, the pollution caused by the use of methanol is 97% less than if a fuel such as gasoline is used. Methanol vehicles produce 99% less carbon monoxide than a gasoline-powered vehicle. On the other hand, as a disadvantage, it has low efficiency because of the fact that methanol can pass through the available membrane materials.

1.8.1 Overall Chemical Reaction in a DMFC

At the anode, methanol is oxidized in the presence of water; the products obtained are carbon dioxide, six protons (H^+) and six electrons according to the chemical reaction (1.1). The six protons (H^+) formed react with the oxygen of the air to give the water according to the chemical reaction (1.2) in the presence of platinum [37-40]. The overall chemical reaction represented by equation 1.3 is a combustion reaction sometimes referred to as cold combustion. In fact, the battery is a means of controlling this reaction to produce a current.

28

Anode Reaction: $CH_3OH + H_2O \rightarrow CO_2 + 6H^+ + 6e^-$ (1.1)

Cathode Reaction: $3/2\ O_2 + 6H^+ + 6e^- \rightarrow 3H_2O$ (1.2)

Overall Reaction: $CH_3OH + 3/2O_2 \rightarrow CO_2 + 2H_2O$ (1.3)
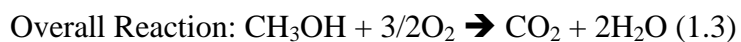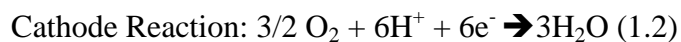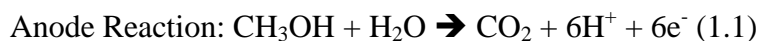
The boiling temperature of methanol at atmospheric pressure is rather low (65 °C), so it requires an operating temperature at around 60-70 °C (to avoid too high vapor pressure). The reaction mechanism is much more complex with the appearance of adsorbed species as well as HCOH and HCOOH [37, 41]. Figure 1.14 represents the proposed mechanism for methanol oxidation reaction. The compounds PtCO are poisons for platinum; the addition of ruthenium makes it possible to remedy them. On the cathode side, oxygen from the air is oxidized (electron release). Theoretically, a yield of 96.7% could be achieved [38]. However, this yield is limited by two factors. On the one hand, by the fact that the oxidation reaction is not always complete; formation of formic acid (HCOOH) or formic aldehyde (HCOH) occurs. The electrode potentials are very different from the theory due to high overvoltage (around 0.3 V at the anode and 0.4 V at the cathode). The electrodes are also poisoned with the intermediate products of the reactions (e.g. HCCOH). At the electrodes, the only catalysts sufficiently active to oxidize methanol and stable at 60 °C are essentially metal alloys based on platinum (Pt-Sn, Pt-Re, Pt-Ru) [41, 42]. The cost problem therefore arises, especially since the current densities are low (150 to 250 mW/cm^2) and the platinum quantities are large (2 mg/ cm^2) due to the lower reactivity of methanol as compared to hydrogen. Operation is therefore being carried out on new platinum-based alloys and new structures for electrodes.

The electrolyte of this type of fuel cell is of the acid type, either a polymeric membrane or a liquid electrolyte. In alkaline solution, which is at high pH, although the reaction is enhanced significantly, alkaline electrolytes are subjected to the disadvantage of carbonation causing deactivation [19, 39]. Membranes are used mainly as for PEM fuel cells. Another problem is the permeation of methanol through the membrane to the cathode and its oxidation with oxygen to carbon dioxide and water (without supplying current). This phenomenon is called "methanol crossover" and it is a loss of fuel estimated at 10% [39]. One solution could be methanol-sealed membranes with acceptable ionic conductivity. While significant

progress has been made in reducing the permeation of methanol, they result in increased membrane strength and so, increased costs.
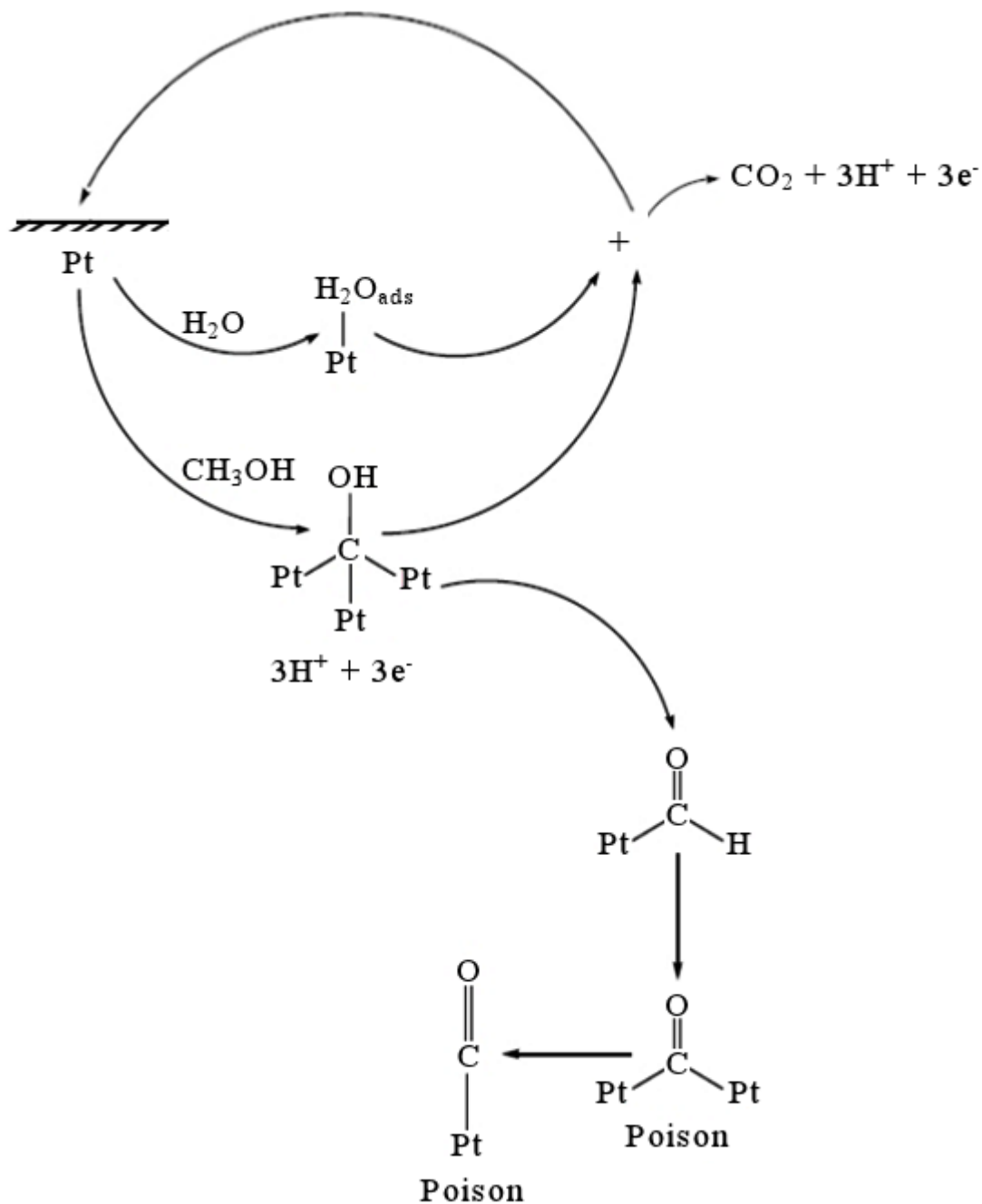
Figure 1.15. Proposed mechanisms for methanol oxidation reaction [43]

CO_2-containing cell effluents require exhaust gas purification by post-catalytic treatment before releasing to the atmosphere; they can thus be washed with water obtained by condensation of that which is in the oxygen or the air leaving the cell. All this reduces the yield to around 20%. However, thanks to its low operating temperature, DMFC can start rapidly and thus respond satisfactorily to changes in

30

power demand. However, the commercial interest of these generators is conditional on the development of efficient electro-catalysts due to the slow kinetics of the oxidation reaction of methanol [37].

1.9 Catalysts

The most widely used catalyst in the fuel cell is pure platinum or alloyed with a transition element such as manganese (Mn), nickel (Ni), cobalt (Co), iron (Fe) [44, 45]. Indeed, only this noble metal (platinum) possesses sufficient electro-catalytic activity with respect to the reduction of oxygen and the oxidation of fuel, and can, in addition, lastingly resist corrosion in very acidic chemical environment. Researches carried out have therefore focused on reducing the amounts of platinum and improving performance. In fact, a better use of the catalyst will significantly increase the electrochemical performances (current or power at fixed voltage). To achieve this objective, researches is being carried out to increase the electro-active surface.
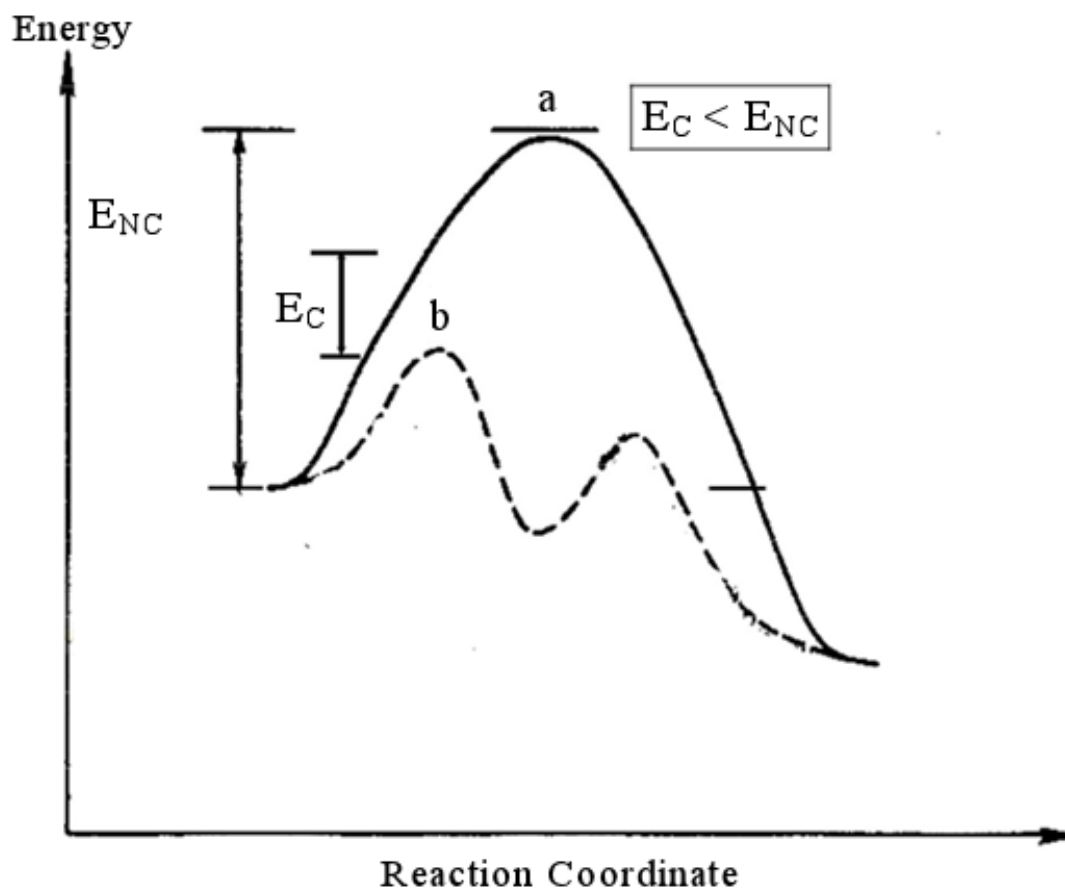
Figure 1.16. Variation of system energy as a function of reaction coordinate

(a is the uncatalyzed reaction, b is the catalyzed reaction)

31

According to Ostwald, a catalyst is "any substance that alters the rate of a chemical reaction without appearing in the final products". The catalyst is thus essentially a speed accelerator. When the starting chemical system can evolve in several thermodynamically possible directions, the catalyst can orient it selectively in a given direction. The catalyst is traditionally indicated above the reaction boom since it is not consumed in the reaction. It is necessary to distinguish between homogeneous catalysis where the catalyst belongs to the same phase as the reactants, and heterogeneous catalysis, where the catalyst belongs to a different phases [46].

1.9.1 Basic Properties of Catalysts

The selection of a catalyst is based primarily on three fundamental properties: activity, stability, and selectivity. It is also related with its application on an industrial scale and the support used. Morphology (shape and size of grains), the mechanical resistance (resistance to attrition, hardness), the porosity (large specific surface area, pore volume, pore size distribution), the thermal characteristics (a good thermal conductivity will allow to limit the gradients of temperature inside the grains and in a possible fixed bed of catalyst) are the main properties taken into account [47]. Other essential criteria are price and reproducibility.

(i) Activity: The catalytic activity is the relative increase in the rate of reaction by the catalyst. A high activity corresponds to an accelerated reaction rate which will result in high productivity and operation under mild operating conditions, in particular at a relatively low temperature at which the reaction can be carried out in a more favorable thermodynamic field.

(ii) Selectivity: Specific reagents can lead to different reaction products depending on how they are used. Thus, if it is desired to produce a given product in a relatively pure state, it is advantageous to employ a specific catalyst for the reaction which leads to the desired product. By increasing the rate of the corresponding reaction, the production of unwanted products is avoided. The same catalyst may have a different activity for various reactions. It can be active for a given reaction, and be absolutely inactive for another. Under the influence of the catalyst, the direction of the reaction is modified. The selectivity is thus defined as the ability of a catalyst to promote a

reaction in a desired direction by repressing the concurrent, concurrent side reactions which are considered to be parasitic.

(iii) Stability: A good stability characterizes the fact that the catalyst evolves only very slowly and remains reversible over time under the conditions of implementation and regeneration.

1.9.2 Heterogeneous Catalysts

The field of heterogeneous catalysis deals with reactions taking place between several physical phases (solid / gas, solid / liquid). The reaction mechanisms may differ depending on the reaction studied, but they always present a step of adsorption or chemisorption of at least one of the reagents on the surface of the catalyst [46]. The reaction then takes place on the surface of the catalyst and will be followed by desorption of the reaction product.

The reaction in the adsorbed phase may result in a decrease in the energy of the transition state and thus of the activation barrier, thereby reducing the reaction temperatures while maintaining a suitable conversion of the reactants. Moreover, the use of catalysts also allows thermodynamically favored reactions, but whose rate without catalyst is very low or even zero [47]. In the case of electro-catalysis, the performance of the catalyst has an influence on the reaction rate and on the overvoltage of the reaction.

The surface structure of the catalyst thus has consequences on the adsorption of the reactants and, by extension, on the catalytic activity of the chosen material. Thus, several factors, such as the presence of surface defects or the crystalline orientation, can influence the reaction kinetics. The chemical composition of the catalyst also makes it possible to modify its catalytic behavior.

The lifetime of heterogeneous catalysts is ultimately limited by a variety of causes such as surface poisoning by substances that prevent molecules from approaching active centers, high temperatures, agglomeration which reduce the specific surface area and in general the catalytic activity. So, they must either be replaced from time to time or regenerated where possible.

1.10 Nanomaterials for Temperature-Based Fuel Cells

Nanoparticles are the subject of a great deal of studies and are today widely used in applications such as electronics, optics and chemical industries. They have different physicochemical properties of the same massive material, which allows variable applications. In catalysis, the two main interests of nanoparticles are the reduction of the cost of production by minimizing the mass used for an identical surface and the fact that the catalytic behavior of a material can be variable according to the size and the shape of the crystals [48]. It is therefore possible to create more efficient catalysts by modifying these two parameters. In electro-catalysis, platinum is the subject of a large number of studies for its good catalytic properties. In order to develop applications such as fuel cells, it is necessary to work on the development of more efficient electro-catalysts.

1.10.1 Areas of Application

Nanoparticles are materials whose size is less than 100 nm in the three dimensions of space. A catalyst makes it possible to decrease the activation energy of a reaction following the adsorption of at least one of the reactants. The catalyst is not transformed during the reaction and does not appear in the reaction balance, only surface atoms (being adsorption sites) are considered as active, which justifies the need to reduce the particle size for increase the surface to volume ratio. The use of nanostructured catalysts thus makes it possible to obtain large surfaces developed with low masses of material [49]. This is due in particular to the fact that the materials generally used in heterogeneous catalysis are noble metals (Pt, Pd, Ru, Rh, Ir, etc.), the price of which is very high.

1.10.2 Influence of Shape on Surface

The shape of the nanocrystals will have an influence on the superficial structure of the object. Under thermodynamic equilibrium conditions, the shape of a nanoparticle is defined by Wulff's theorem [50, 51]. The face-centered cubic (fcc) crystalline compounds have three oriented surfaces of low Miller index which have the orientations (111), (100) and (110) shown in Figure 1.17 [51]. The energy of these surfaces is such that the domains (111) are more stable than the domains (100) themselves more stable than the orientation domains (110). In general, orientation

surfaces (110) are not considered to be significantly present for nanoparticles, so a nanocrystal will be composed of a mixture of orienting surfaces (111) and (100).
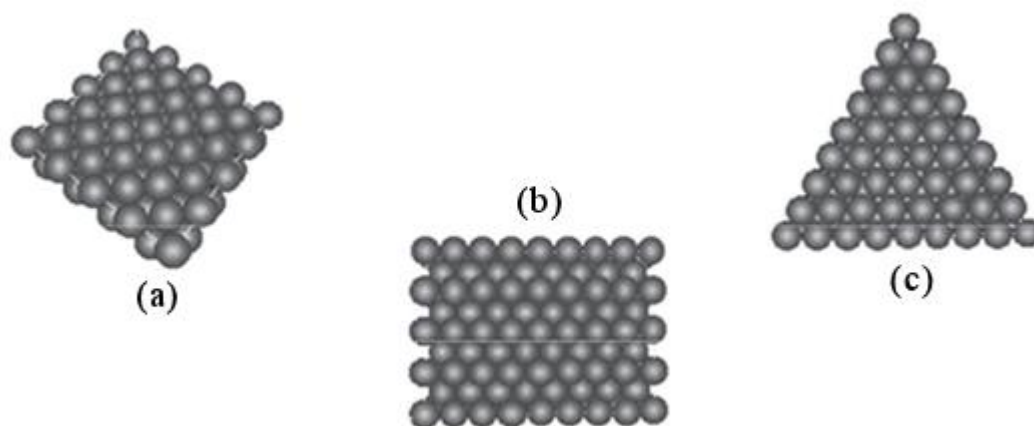
Figure 1.17. Representation of the crystal orientations of low Miller index for a compound fcc such as platinum. (100) at (a), (110) at (b) and (111) at (c).

From the point of view of Wulff's construction, the energetically favored form will be that of which the distances of the faces with respect to the center of the crystal are proportional to the surface energy according to following equation:

$$\gamma_{(100)} / \gamma_{(111)} = d_{(100)} / d_{(111)}$$

where γ represents the surface energy of the different faces and d is the distance between the faces and the center of the nanoparticles. The equilibrium form of a compound fcc is thus the truncated octahedron satisfying this equality having six square faces of symmetry (100) and eight oriented hexagonal faces (111) shown in Figure 1.17.

The surface structure of these nanocrystals is different in terms of crystalline orientation. Thus, an octahedron or a tetrahedron are forms exhibiting only orientation domains (111), while the cube exposes six orientation faces (100). The cuboctahedron presents on the surface a mixture of these two orientations. The preparation of truncated cubes or truncated octahedrons also leads to the formation of mixed surfaces whose proportions in each orientation are dependent on the level of truncation [50, 51]. It is important that regardless of the shape of the nanoparticles, the different faces will be separated by edges and corners formed of atoms of low coordination.

The physical properties of the materials can be strongly influenced by the particle size. In particular, a contraction of the mesh parameter with the decrease in the size of the nanoparticles is commonly observed. This contraction is associated with the high pressure of the external environment towards the center of the particle and the strong surface stresses.

Finally, the catalytic behavior of nanoparticles will also depend on factors such as the size or shape of the crystals. Indeed, various studies on the catalytic activity of nanomaterials have shown that some catalytic reactions are sensitive to the structure of the surface. For these reactions, the nature of the adsorption site in terms of crystal structure or coordination has an influence on the activity of the catalyst. In some cases, the surface structure of the catalyst even makes it possible to control the selectivity of the reaction so as to obtain only a single reaction product. It is therefore very important to have means for characterizing the surfaces of the materials in order to improve the understanding of the reaction mechanisms for which they are used as catalysts. It would then be possible to demonstrate the parameters having an influence on the activity, the selectivity or the tolerance of a catalytic material in order to produce better catalysts. The study of nanoscopic objects presenting a surface whose complexity is reduced to the maximum (with an orientation of the surface according to a largely predominant crystallographic plane) is a means of increasing the understanding of the catalytic phenomena on the surface of a nanomaterial.

1.11 Supported Catalysts

In general, the catalysts are dispersed on the surface of a support allowing better exposure. Indeed, a good support must have a large specific surface area in order to guarantee good distribution of the nanoparticles but also a high stability over time when exposed to the conditions of use such as acidic or basic media, high temperature etc.

For electro-catalysis, the question of support is also very important. The application of a catalyst to the field of electro-catalysis requires the use of supports having good electronic conductivity and also a stability in the potential range considered for the intended application. The chemical environment of use of the electro-catalysts may also have conditions of pH, temperature or pressure aggravating the phenomena of

degradation of the support [52]. A large majority of the electro-catalysts are therefore dispersed on carbon supports. This material has the qualities necessary for fuel cell applications in terms of electron conduction and corrosion resistance and can also be chemically modified to improve or bring new properties to the catalytic layer [53].

The supported catalysts are in a form suitable for the actual application; these objects of study are extremely complex. Indeed, they are composed of nanoparticles disseminated on the surface of a powdered carbon (the Vulcan XC72), the interaction between the metal and the support will therefore have to be taken into account [54, 55]. In addition, a polymeric binder is often added to the catalytic ink to allow good cohesion of the catalytic layer. In fact, a fundamental study of the catalytic processes carried out on supported catalysts will be very difficult because of the very large number of factors influencing the catalytic behavior.

1.11.1 Effect of Support

Conventional electro-catalysts based on platinum, as stated above, are typically supported on carbonaceous materials having a large specific surface area. The use of carbon supports can improve the dispersion of the active metals, and may consequently lead to an increase in the catalytic activity of the electro-catalysts [53]. The activity of the catalysts is often related to the morphology of the supports used. The interactions of the metal with the support allow the metal to acquire certain stability in the dispersed state and thus increase its active surface area. However, the efficiency of a support depends on certain geometric and mechanical characteristics. Geometrically, it must provide a suitable surface and porosity to allow the metal to disperse well and to avoid the phenomenon of diffusion in the pores [54]. Mechanically, it must have a good resistance to thermal shock and to wear by friction. The support therefore has an impact on the performance of the catalyst. Indeed, by fixing the active substance within the support, the agglomeration of the metallic species is reduced. In addition, it is much easier to recover a catalyst at the end of a catalytic reaction when supported.

The most commonly used supports are Vulcan carbon-based materials such as the Vulcan XC-72 or the Vulcan XC-72R [55]. Despite their advantages, such as high electron conductivity and high surface area, the deposition of platinum nanoparticles on these supports also leads to the numerous problems such as the low stability and

therefore the low durability of the electro-catalysts during battery tests. Indeed, Vulcan carbon is not stable; it oxidizes thermodynamically to CO_2 at a potential of 0.21V/SHE and 0.97 V/SHE in acid medium [55]. This value was measured by mass spectrometry coupled with electrochemistry (Differential Electrochemical Mass Spectroscopy: DEMS). For this reason studies are currently being carried out on the development of new carriers in order to improve the electro-catalytic activity of the catalysts for the related reactions and their stability and tolerance for small organic molecules. In particular, studies have been carried out on the use of different carbon-based materials ("graphitic" carbons, graphene-based materials) or on new metal oxide composite supports.

By nature, nanostructured carbon materials provide anchor points for a metal center [52, 53]. Apart from its chemical inertia, carbon also has many interesting physical properties (electronic conductivity, high surface area). It has also been demonstrated that an electronic modification of the catalytic material can be achieved by strong interaction with a carbonaceous material. This interaction can lead to excellent durability as well as considerable tolerance to the CO molecule. It has previously been proposed that carbonaceous carriers having a high degree of graphitization such as carbon nanotubes (CNT) or graphene derivatives are much more thermally and electrochemically stable due to their increased resistance to corrosion [53, 53]. The excellent stability of them leads to a high stability for the supported Pt catalysts. Moreover, the increase in the degree of graphitization leads to an increase in the interaction between the Pt nanoparticles and the surface π sites which act as anchor centers for platinum, thus enhancing the metal-support. By virtue of the existence of this metal-carbon interaction, it appears that the use of such supporting materials improves the durability of the supported electro-catalysts and their tolerance to the molecule of CO [55, 56]. This metal-carbon interaction can also be modulated by using both the nanoparticle synthesis method and the degree of order of the carbon structure.

1.11.2 Platinum Nanoparticles on a Support

In heterogeneous catalysis, the platinum is in the form of metal nanoparticles dispersed on a support. The main difference between a massive material and a nanoparticle is the ratio of surface atoms to volume atoms, which is very important

38

for nanoparticles. The catalytic properties of a nanoparticle are improved with respect to the solid material, since only the surface atoms are accessible to the reactants; and, this ratio depends on the morphology of the nanoparticle. For crystalline materials such as platinum, the crystal structure determines the geometries of the nanoparticles. Thus, platinum is face-centered-cubic (fcc) and can adopt several configurations (cuboctahedron, icosahedron, tetrahedron, octahedron etc.) as mentioned above. The cuboctahedron is the geometry that makes it possible to obtain the smallest nanoparticles. The morphologies and sizes are generated according to the conditions of preparation of the nanoparticles on the support.

The support can be considered only as a dispersant, in which case it allows the physical separation of the nanoparticles and their stabilization. But it is sometimes active; the phenomenon known as strong metal support interaction (SMSI) modifies the chemisorption properties and the catalytic activity of the metal.

1.12 Preparation Methods of Supported Electro-Catalysts

A supported metal catalyst generally consists of a metal belonging to the columns 8, 9, 10 and 11 of the Periodic Table of the Elements, deposited on a support (alumina, silica, coal, etc.). This type of metal has the property of possessing orbital above and below the Fermi level, that is to say levels that are both electron donors and acceptors. As a result, electrons move freely in these orbitals, making it possible to create either bonds with electron-deficient molecules or holes, allowing the electron-rich molecules to adsorb easily. The metal can therefore chemisorber and consequently activate very diverse molecules. Metal is rarely used in a massive state because it has a specific surface area which is too low [57-59]. This is why it is generally deposited on a support, at a rate of a few percent by weight, in order to increase its active area.

The usual methods of preparation of the supported catalysts are grouped into three approaches: colloidal methods, microemulsions and impregnation [59]. These methods are largely derived from the development of catalysts for methanol fuel cells.

Colloidal approaches covers a wide variety of methods, all based on the same principle. A colloidal solution of metal precursors is prepared and deposited onto the

carbon support [60]. In this approach, the presence of a surfactant is required to avoid particle agglomeration. Chemical or thermal treatment allows the reduction of metals as well as decomposition of surfactants. Among the colloidal approaches, there is the reduction method of alcohols where polyethylene glycol serves as both solvent and reducing agent [60, 61]. Then, there is the Bönnemann method which uses organometallic colloids [62]. The disadvantage of several colloidal methods is that the agglomeration of the particles and their growth during the heating stages is difficult to control. However, this limitation does not appear to apply to the Bönnemann method, for which the composition, shape and size of the catalyst particles can be controlled. On the other hand, the surfactants used are expensive and there is potential of contamination of the catalyst.

The microemulsion of water in oil is the second approach to prepare carbon supported catalysts. It involves preparing a suspension of water droplets in which metal salts are dissolved. The addition of a chemical reducer causes the crystallization of nanoparticles in the microemulsions [57, 58]. Then the whole is adsorbed on a carbon support, and then the microemulsion is decomposed. Some work on the electrocatalysts for the oxidation of ethanol prepared by this method has been published. The advantages and disadvantages are practically the same as for colloidal approaches.

The third approach is the impregnation method discussed detailed in the following section. It is employed in this study due to no requirement of surfactants or stabilizers. There are also other more marginal methods such as thermal decomposition, sonochemistry, microwave irradiation and thermal decomposition of polymeric precursors [59]. These methods also require sample heating, which may be a limiting factor in controlling the microstructure and composition of final material.

1.12.1 Impregnation Method

The impregnation method is widely used in the scientific community. The protocol which is favored consists first and foremost of chemically modifying the surface of the carbon. In the impregnation step, the metal precursors are mixed with the carbon substrate in an aqueous solution. This step is followed by a reduction step, either by chemical reduction with strong and soluble reducing agents (formic acid, $NaBH_4$, N_2H_4, $Na_2S_2O_3$, $Na_4S_2O_5$) or by dihydrogen [63]. The main advantage of this method

comes from not using surfactants or stabilizers to control the particle size of the nanocatalysts in the reduction step. For the other methods, it is an additional and troublesome work to remove these materials which reduce the surface activity if not removed completely. On the other hand, its main weakness is that it generally leads to the preparation of carbon powders having low amounts of metal.

The preparation of a catalyst by impregnation is the operation of wetting the support with the solution of the metallic precursor salts. The active agent is never introduced into a porous support in its definitive form. The selection of the precursor has a great importance on the quality of the final deposit, namely its structure, its particle size distribution, its dispersion. Depending on whether there is interaction between the support and the precursors at the time of wetting, two types of impregnation can be considered.

Impregnation without interaction is known as wetting without interaction or "incipient wetness impregnation", consists in bringing the support into contact with the solution of the precursor. In this case of impregnation without interaction, the volume of the solution containing the precursor salt must not exceed the pore volume of the support. Under the action of the capillary forces, the solution is introduced into the pores of the catalyst and distributed there. The catalytic solid is then dried without being washed (washing would reversibly cause the precursor out of the support) to cause supersaturation of the solution and crystallization of the precursor in the pores of the support. Finally, calcination takes place, followed by reduction of the precursor [63].

Impregnation with interaction is known as wetting with interaction or also wet-soaking, is the one where, at the moment of wetting, a bond is established between the solute to be deposited and the surface of the support. It makes it possible to obtain a good atomic dispersion of the active agent which binds to well-defined sites of the support. The interaction between solute and support can be ion exchange (anionic or cationic), adsorption or chemical reaction. Ionic exchanges occur more frequently than other types of interaction. This technique is generally used in the preparation of precious metal catalysts which requires the least possible use whilst obtaining a maximum active surface area. This is only possible with strict control of the parameters that the type of substrate and its surface state (nature and number of

surface hydroxyl groups and their acid-base properties), and the impregnation solution (pH, concentration and type of the precursor metal, the presence of competing ions) [64].

In other words, during wet impregnation, the support is immersed in the precursor solution. In the case of capillary (ion-exchange) impregnation, the support is dry, whereas in the case of diffusional impregnation it is filled with solvent. The drying step which follows the impregnation has the purpose of removing the solvent contained in the wet solid.

In the case of an impregnation with interaction, the bonds created between the support and the precursor are strong and the drying will therefore have no other effect than to evaporate the solvent. On the other hand, in the case of impregnation without interaction, this step is very important because it can redistribute the active elements deposited in the porosity of the grains of the support. The rate of drying plays a role in the distribution of the active elements. When the drying is carried out under mild conditions, with a low temperature and a relatively high humidity of the gas stream, the catalyst obtained will be of the homogeneous type with high reactivity. On the other hand, Fulton's work in 1986 [65] showed that, under fast drying conditions, the product exhibits both macroscopic (heterogeneous grain) and microscopic heterogeneities (poor distribution verified by a reduction in reactivity). The operating conditions used during drying, as well as the properties of the support and of the precursor solution, therefore have a significant impact on the location of the deposit.

The last operation during the synthesis of heterogeneous catalysts in the liquid route is activation, also called reduction. The solid is also placed at high temperature under a gaseous atmosphere which is reducing: a mixture of dihydrogen and dinitrogen. The object is to reduce the metal oxide to metal. In some rare cases, the reduction of the catalysts is carried out in solution by chemical reagents such as formaldehyde or hydrazine. The variables of this stage are the parameters that the rate of rise in temperature, the final temperature reached, the duration of the operation and the flow rate of dihydrogen and its concentration. Pinna (1998) pointed out that a rapid sweep through the gas stream of dihydrogen is preferable in order to evacuate the water formed by this reaction [66]. It is thus possible to move the equilibrium towards the

reduction and to prevent the water vapor from altering the dispersion of the metal within the support.

Briefly, the interaction between the precursor and the support may influence the distribution of the precursor within the support. If these interactions are weak, post-impregnation thermal treatments (drying and calcination) may lead to a redistribution of the precursor, and drying is a decisive step in the process [67]. When the precursor has a very high affinity for the support, in this case, drying cannot be considered as a key operation.

At the end of the impregnation step, the dispersion of the precursor within the support depends essentially on the phenomenon of adsorption, that is to say on the metal / surface interaction. The other parameters to be considered are the structure of the support (size and distribution in pore sizes, internal porosity and tortuosity) and the properties of the precursor solution, namely its viscosity and its molecular diffusivity.

In general, apart from the textural properties of the support, impregnation in the liquid route depends only on the precursor concentration in solution and on the physicochemical properties of the solution. Thus, for a given solution-support system, a significant parameter of the system is the precursor concentration.

1.13 Graphene and Graphene Derivatives

Graphene that can be a preference as supporting material due to its high surface area is a layer at the atomic scale, a two-dimensional (2D) sheet composed of sp^2 carbon atoms arranged in a honeycomb structure (Figure 1.19). The honeycomb structure is a perfect alternation of single and double bonds, which gives mobility to the load carriers and therefore ballistic properties of charge transport to the material [68, 70]. Graphene has aroused great interest in the scientific world for several years (Figure 1.18).

Graphene was considered the building block of all other allotropies of graphitic carbon with different dimensionalities. For example, graphite (3 D carbon allotropy) consists of graphene sheets stacked one on top of the other and separated by a distance of 3.4 A° [68]. Fullerene (0D carbon allotropy) can be envisioned to be

made by wrapping a section of graphene sheet. Carbon nanotubes (CNT) and nanoribbans (1D carbon allotropies) can be achieved by winding and cutting the graphene sheets, respectively. In fact, these carbon allotropies, with the exception of nanoribbons, are not synthesized from graphene. Graphite is a natural material, it was first discovered in a deposit near Borrowdale, England, in 1555, but its first use began 4000 years before that date [69]. In 1940, it was theoretically established that graphene is the building block (by stacking) of graphite [69]. Carbon nanotubes were first synthesized in 1991 following the discovery of fullerene in 1985. In 2004, Geim and his colleagues at the University of Manchester succeeded in experimentally carrying out a single layer of graphene in a simple table experiment, when graphene was separated from graphite using micromechanical cleavage [68]. In 2010, the Nobel Prize in Physics was awarded to André Geim and Konstantin Novoselov for this discovery.
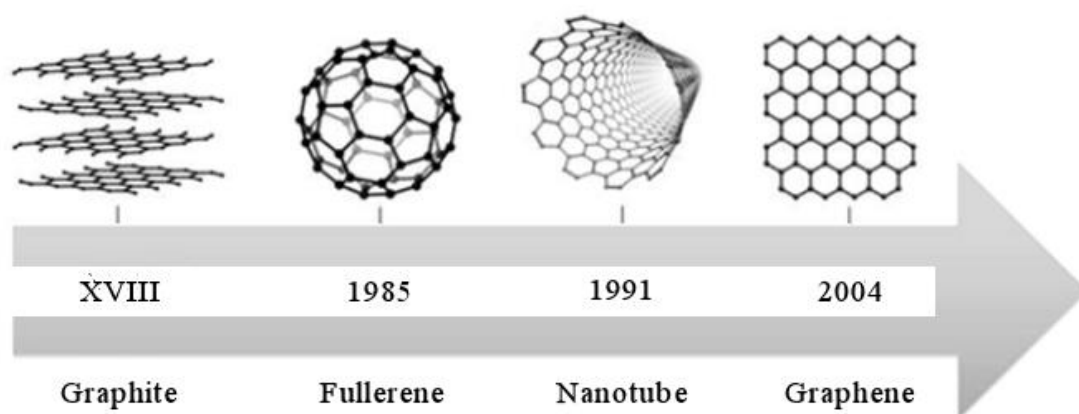
Figure 1.18. Graphite to graphene [20]

The GO was prepared by Brodie et al. In 1859 [71]. Then, it was also produced by alternative methods developed by Staudenmaier or Hummers et al. respectively in the years 1890 and 1950, in which the graphite is oxidized using strong mineral acids and oxidizing agents such as $KMnO_4$, $KClO_3$, and $NaNO_3$ in the presence of sulfuric acid (H_2SO_4) or its mixture with of nitric acid (HNO_3) [72]. These reactions to achieve similar levels of oxidation (C:O ratio of about 2:1) which can disrupt the delocalized graphite electron structure and impart a variety of oxygen-based chemical functions to the surface of Graphite plane. Although the precise GO structure is still a subject of debate, it has been the subject of experimental and theoretical studies. Experimentally it has been demonstrated that hydroxyl (-OH) and epoxide (>O) groups are located on the plane of each sheet and carboxylic acid

44

groups (-COOH) are located on the edge of the planes (Figure 1.19). Recently, (Gao et al.) the structure of GO was studied by using 13C NMR [73]. It is proposed that, in addition to the epoxide and hydroxyl groups, the GO contains ketones, 6-membered lactol, and tertiary alcohol. Theoretically, the Lerf-Klinowski model (Figure 1.19) is the most suitable for experimental studies [71].
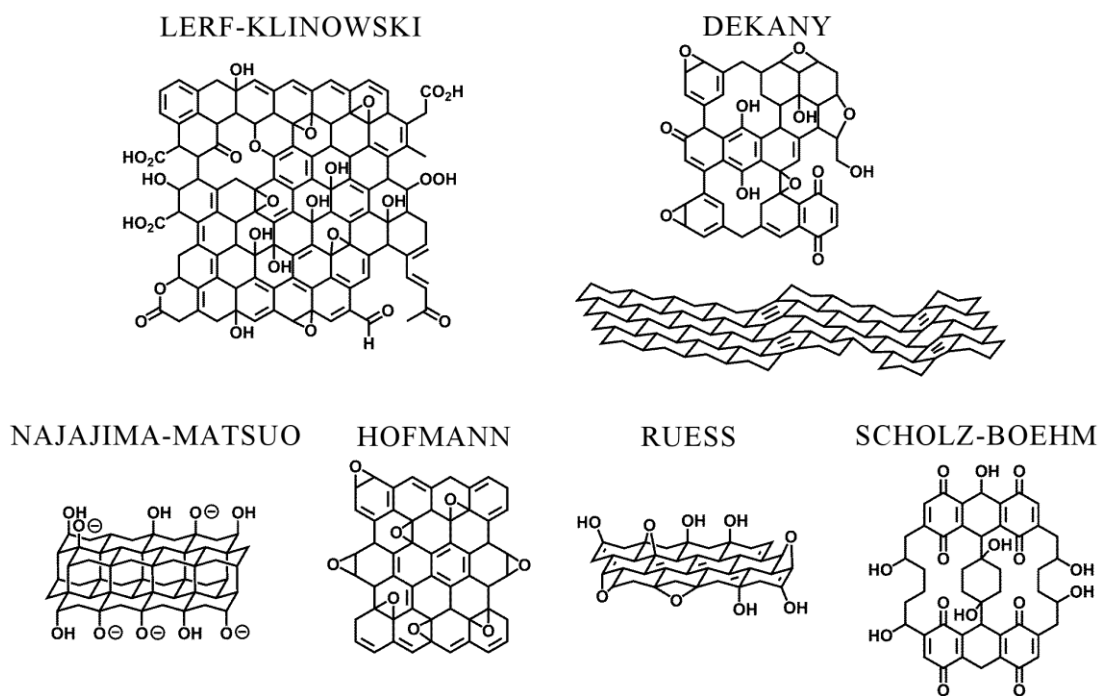
Figure 1.19. Models indicating the functional groups on the edge of GO [75]

Graphene derivatives have very high electronic and thermal conductivity, extremely high surface area (theoretically 2630 m^2 g^{-1}) and high mechanical strength [76]. The main characteristic of GO with respect to graphene is the loss of electronic conductivity due to the partial transition from sp^2 to sp^3 carbon atoms. The reduction of GO would recover part of the characteristic conductivity of graphene by partially restoring the π-network. The elimination of oxide groups would create vacancies along the sp^2 carbon structure which could favor the deposition and dispersion of the catalyst particles.

CHAPTER 2

EXPERIMENTAL

2.1 Chemicals

H_2SO_4 (95-97%, Merck), H_3PO_4 (65%, Merck), Graphite (Sigma-Aldrich), $KMnO_4$ (Merck), H_2O_2, HCl (fuming 37%, Merck), $(C_2H_5)_2O$ (Sigma-Aldrich), NaOH (99%, Merck), $CS(NH_2)_2$ (Eastman Organic Chemicals), HBr (99%, Merck), H_2PtCl_6 (Sigma-Aldrich), CH_3CH_2OH (99.9%, Merck), CH_3OH (99.8%, Merck), CCl_4 (99%, Merck), $HClO_4$ (60%, Merck), Nafion (5%, Sigma-Aldrich), Dimethylformamide (Merck), N-Methyl-2-pyrrolidone (Merck) were used as pure form. Deionized water (18 MΩ) was distilled over Millipore water purification system.

2.2 Preparation of Graphene Oxide

Graphene Oxide (GO) has been synthesized by oxidizing the purified natural flake graphite (NFG) via the modified Hummers' method (Figure 2.1) in order to use for the main experiments. In this method, $KMnO_4$, H_2SO_4, H_3PO_4 has been used as oxidants. Less defection, high yield and less pollution are the advantages of this method whereas being highly time-consuming is a disadvantage.

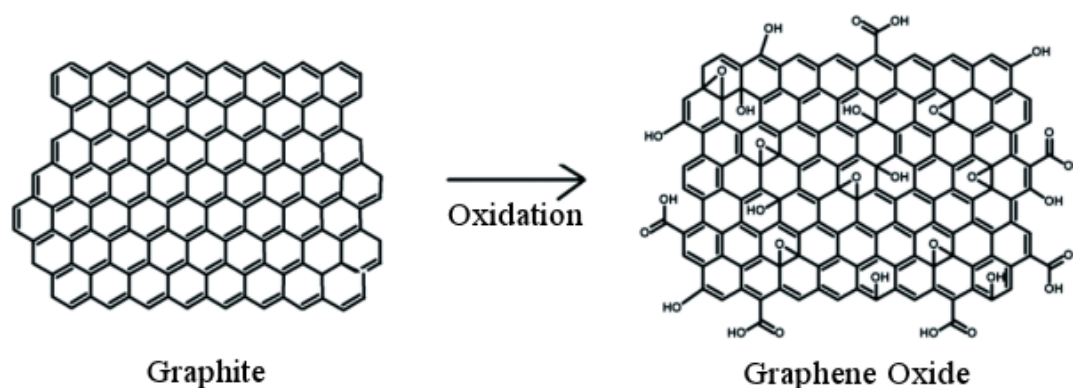

Figure 2.1. Schematic representation of Hummers' method process

Briefly, a 9:1 homogeneous mixture of concentrated H_2SO_4/H_3PO_4 (360:40 mL) was added to a mixture of graphite flakes (3 g) with a continuous stirring. The reaction

was then heated to 80 ^{o}C and stirred continued for 6 hours by means of a magnetic heater. Then, the mixture was allowed to cool to room temperature; and, 18 g of KMnO$_4$ was gradually added with a continuous stirring at 35 ^{o}C for 4 hours. In the next step, 1.5 L of purified water is added to the solution. Just after then, 15 mL of 30% H$_2$O$_2$ was added in order to remove the excessive potassium permanganate; then, a bright yellow color and bubbles were observed. The mixture was filtered and washed 5 times with 0.1 M HCl to remove metal contamination. The brownish precipitate was then washed again with 1 L of distilled water; and, after the filtrate was adjusted to pH 7, it was dried under vacuum at 70 °C to obtain graphene oxide.

2.3 Treatment of GO by Thiourea

Thiourea (TU) treated GOs were prepared by using the method of thiol functionalization. GO (100 mg) was dispersed in deionized water, stirred for at least one night and ultrasonicated for at least 8 hours respectively until a homogeneous mixture was obtained in order to form 1 mg/mL dispersion. Then the solution was transferred to a rounded flask placed in a sand bath which provides an equal heat distribution (Figure 2.2). In this method, hydroxyl and epoxide groups were targeted; for this reason, graphene oxide was subjected to hydrobromic acid (HBr) for an aim of achieving simultaneous reduction and bromination effects on graphene oxide [77]; therefore, HBr (6.67 mL) was added to the mixture in the rounded flask and stirred continuously under reflux at room temperature for 3 hours by means of a magnetic stirrer. Then, the temperature was increased to 80 ^{o}C under reflux; and, thiourea (0.67 g) was added with continuous stirring for 80 ^{o}C. By changing the duration of the treatment with TU at this step, four different solutions were obtained which were 20 min, 2h, 5h and 24h treated. Then, the solutions were allowed to cool to the room temperature. For the aim of hydrolysis, 4 M NaOH (47 mL) was added to only 24 h treated GO; and, this mixture was further stirred at room temperature for 30 min. All the TU-treated solutions were then filtered and washed with deionized water over a 0.2 µm regenerated cellulose filter. The filtered solids were re-dispersed in water and treated with ultrasonication for 10 min three times. The final solids were dried in the oven at 60 ^{o}C for at least 15 h.

By this method, four different supporting materials treated for 20 min, 2h, 5h and 24 h were obtained one by one. Also, samples treated at various durations were

collected and characterized by FTIR in order to observe the change over time, as explained in results.
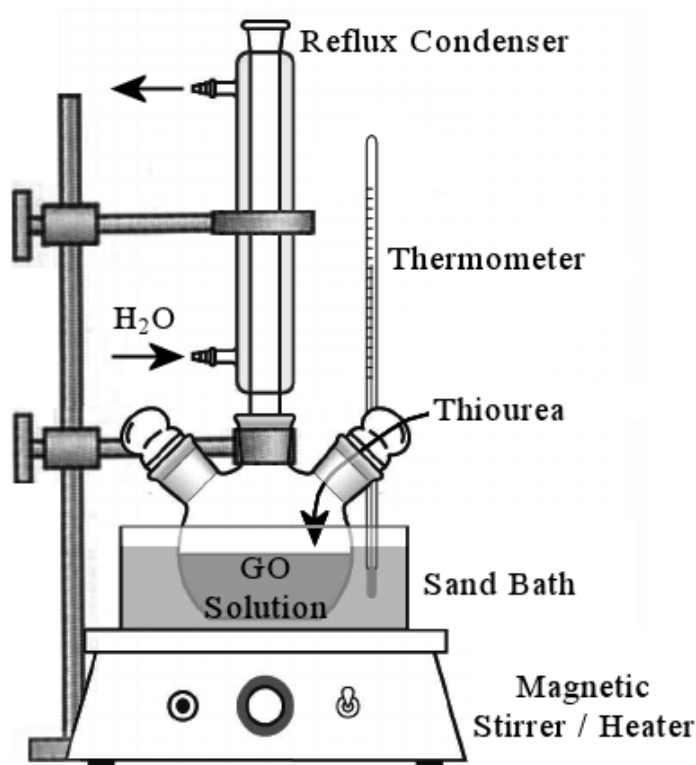
Figure 2.2. Experimental setup of thiol functionalization process

2.4 Preparation of the Nanocatalysts

The preparation of Pt nanoparticles supported by GO and TU-treated GOs was accomplished by impregnation method and hydrogen gas reduction. All of the nanocatalysts were prepared with theoretical amount of 30% (by weight) Pt. The actual amounts of Pt (% by weight) were determined by ICP-MS.

In this method, 50 mg of supporting material was added to 8.97 mL of 12.25×10^{-3} M of chloroplatinic acid ($H_2PtCl_6.6H_2O$) solution. The mixture was initially stirred continuously by the means of a magnetic stirrer at room temperature for at least 2 days; and ultrasonicated for at least eight hours in sonication bath to achieve good dispersion of the precursor on supporting material. The well-dispersed solution was then dried in the oven at 60 °C for at least 15h to evaporate water completely. After drying step, the solid containing the precursor deposited onto the support were collected and put into a sealed reduction vessel placed into sand bath on a magnetic heater (Figure 2.3). Nitrogen gas was flown into the reaction medium while the

temperature was increased up to 170 °C. At 170 °C, nitrogen gas flow was stopped and hydrogen gas was flown into the system while the temperature was increased up to 210 °C. It was continued to hydrogen gas flow into the system at 210 °C for 1 h. At the end of the 1h, the reduction vessel was taken out of the sand bath and allowed to cool at room temperature under nitrogen gas atmosphere. The prepared nanocatalyst was then collected from the vessel and stored in a sample holder. Five different nanocatalysts (Pt / GO and Pt / TU-treated GOs) were prepared one by one by this process and used for further analyses.
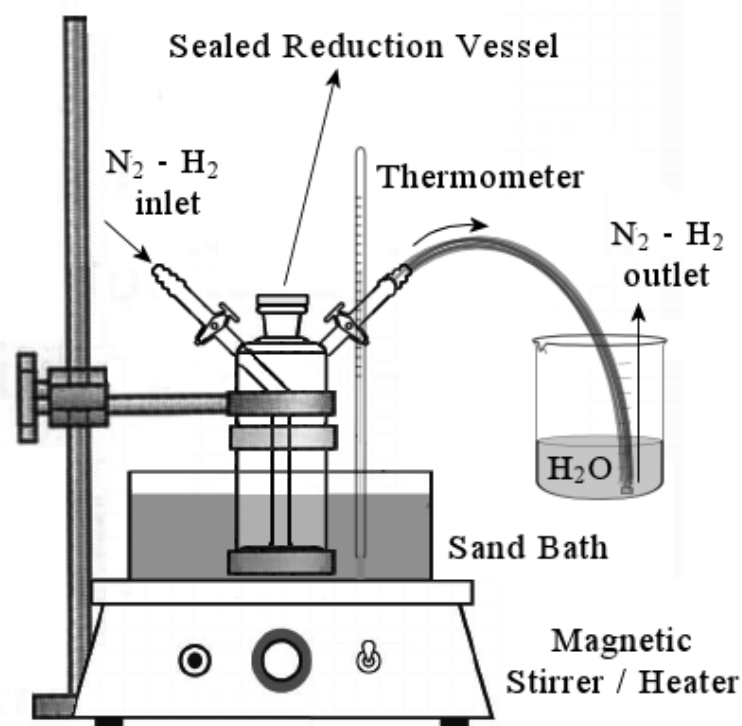
Figure 2.3. Experimental setup of hydrogen gas reduction process

2.5 Preparation of the Electrode Mixtures

The electrode mixtures of the nanocatalysts were prepared according to the following method [78]: 10 mg of the nanocatalysts prepared, 0.5 mL of nafion, 0.15 mL of N,N-dimethyl form amide, and 2.0 mL of N-Methyl-2-pyrrolidone were mixed in a sample holder one by one for each catalyst. These mixtures were ultrasonicated for at least 5h and continuously stirred by the means of a magnetic stirrer for at least two days to obtain highly-dispersed colloidal solutions. Then, 40 μL of each of these well-dispersed solutions for each electrode were loaded on the glassy carbon electrodes with 7 mm-diameters. The loaded electrodes were dried by increasing the

temperature by 5 $^\circ$C in every 30 minutes from room temperature up to 100 $^\circ$C. These electrodes were employed as working electrodes for cyclic voltammetry experiments.

2.6 Fourier Transform Infra-Red Spectroscopy (FTIR)

FTIR is based on the interaction between infrared radiation and the analyzed material. Infrared spectroscopy allows determining the molecular structure of the materials analyzed. An IR spectrum is formed by plotting the absorbance of a photon as a function of its wavenumber. The wavenumber, the unit most commonly used in IR spectrometry, has the advantage of being directly proportional to the frequency and therefore to the energy of the absorbed radiation.

The principle of IR spectroscopy consists in probing the material by means of IR radiation (between 4000 cm^{-1} and 400 cm^{-1}) and to analyze in return the absorption of the radiation emitted by the molecules. The molecules begin to vibrate as a result of the interaction with infrared light. This vibrational and rotational ball is performed in the most perfect rigor, tabulated by group theory. These absorptions are quantified.

The frequency of oscillation depends on the masses of the atoms and on the binding force [79]. This frequency is given by Hooke's law:

$$\bar{v} = 1/\lambda = v/c = E/(hc) = 1/(2\pi c) \sqrt{\frac{f(M_x + M_y)}{M_x M_y}}$$

where v is frequency or vibration wavenumber (cm^{-1}), λ is incident photon wavelength (cm), c is light velocity (2,998.1010 cm.s^{-1}), E is photon energy (J), h is Planck constant (6.63.10^{-34} J.s), f is link strength constant (dyne.cm^{-1}, 1 dyne = 10^{-4} N), and Ms are the massed (g) of the X and Y atoms.

The radiation is decomposed over a suitable wavenumber range from v_1 to v_2; and, the measurement of I_0/I gives an absorption spectrum with the wavenumbers of excited transitions. It is thus possible to determine the nature of the various absorbent entities.

The absorbance A, defined by $\log_{10}(I_0/I)$, is according to the Beer-Lambert law, proportional to c and l, which gives:

$$A = \log_{10}(I_o / I) = \varepsilon.c.l$$

where ε is the molar absorption coefficient (L mol^{-1} cm^{-1}), c is the concentration of the sample (mol L^{-1}); and, l is the path length of the cell (cm). The vibrations representing a variation of the electric dipole moment give rise to IR absorption.
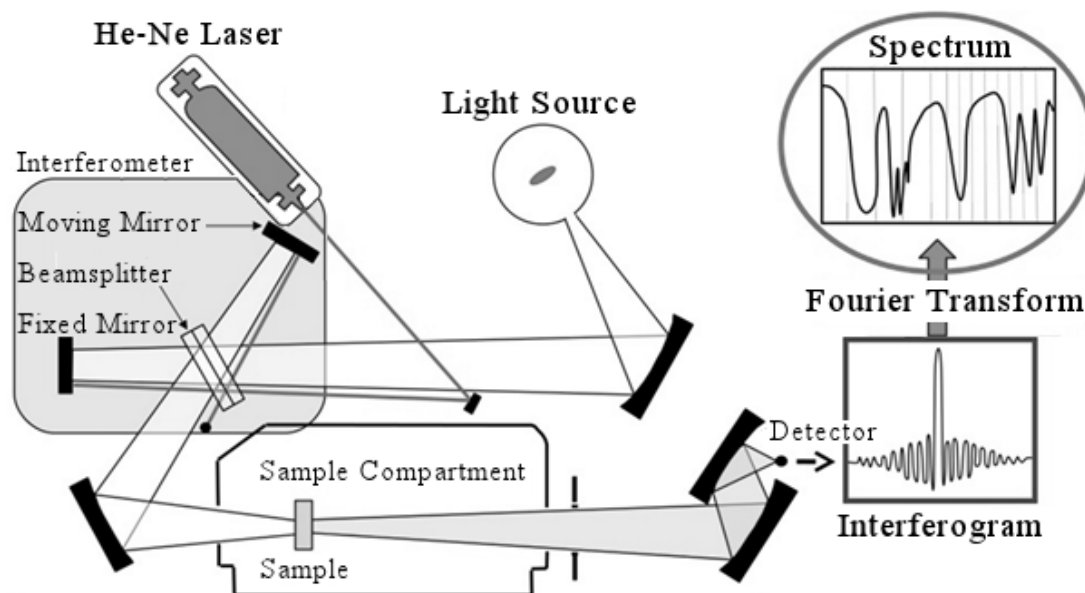

Figure 2.4. Schematic representation of FTIR spectrometer

Fourier Transform Infra-Red Spectrophotometer (FTIR) consists of light source, sample compartment, He-Ne laser, moving mirror, beamsplitter, fixed mirror, detector and interferometer (Figure 2.4). Radiation emitted from the source is split into two with a beamsplitter in the interferometer. The fixed and moving mirrors reflect each of the beams back to the beamsplitter, where the two beams recombine into one and fall on the detector. The two beams combine constructively or destructively, varying as the optical path difference, when the moving mirror is moved. When the combined beam is transmitted through the sample, it is detected as an interferogram and contains all infrared information on the sample. The infrared spectrum is obtained from the interferogram by the mathematical process of Fourier transformation.

In this study, the reference sample KBr was initially dried at 100 $^\circ$C for five hours since it is hygroscopic. Large particles scatter the infrared beam and cause a slope baseline of spectrum; therefore, the powder sample of dried KBr must be ground to

reduce the particle size. A spatula of KBr was grinded in a mortar until crystallites could no longer be seen and powder start sticking to the mortar. Powder samples of the supporting materials (GO and thiourea-treated GOs) in an amount of 1% - 2 % of the KBr were added to the mortar and grinded for 3-5 minutes to obtain a fine powder mixture. If the powder are not ground well or not dispersed properly, this causes pallets having white spots. The final powder mixture was then placed into a stainless steel die and the die was placed into the hydraulic press for 2 minutes under 10-tonnes pressure to form sample pellets. Thin and transparent pallets were prepared since opaque pellets give poor spectra. Afterwards, measurements of the pellets were accomplished by Bruker 66 v/s) in the range between 400 and 4000 cm^{-1} at 16 scans at room temperature at METU Chemistry Department.

2.7 Raman Scattering Spectroscopy

Raman spectroscopy is an optical method analyzing the dynamics of atoms through the tensor coupling between a monochromatic light and the polarizability variation of chemical bonds; in other words, the deformation of the electron cloud during the motion of atoms [80]. This method exploits the physical phenomenon according to which a medium modifies slightly the frequency of the light circulating there. This frequency shift corresponds to an exchange of energy between the light ray and the medium and gives information about the substrate itself.

The principle of Raman spectroscopy is relatively simple. A beam of monochromatic light produced by a continuous laser of frequency υ_0 is focused on the sample to be analyzed. The energy E_0 of the incident radiation is defined by the following relation:

$$E_0 = h\upsilon_0 = h(c / \lambda_0)$$

where h is Planck constant (6.63×10^{-34} J·s), υ_0 is the frequency of incident radiation, c is velocity of light in vacuum (3×10^8 m/s) and λ_0 is the wavelength of the incident radiation. The incident photons are largely transmitted, reflected or absorbed and a much smaller fraction is diffused so that a part of the light is scattered at the same frequency as the incident radiation, and in this case we speak of elastic diffusion or Rayleigh scattering; and, a tiny part of the incident photons is diffused with frequency change. The latter is determined as inelastic scattering or Raman scattering

and represents about 1 Raman photon for 10 incident photons (in order of magnitude).

Figure 2.5 illustrates the Rayleigh and Raman scattering mechanisms. If the frequency of the scattered photon (υ) is less than that of the incident photon (υ_0), there is a gain of vibrational energy for the molecule (and energy loss for the photon); and, this corresponds to the Stokes line. If, on the contrary, the incident photon is scattered at a frequency $\theta + \upsilon$, there is loss of vibrational energy for the molecule (and energy gain for the photon), which corresponds to the anti-Stokes line.
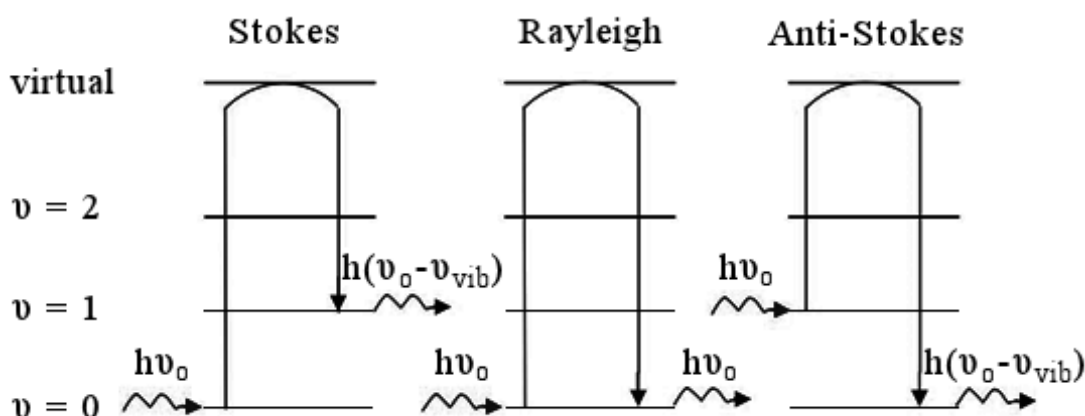

Figure 2.5. Raman and Rayleigh diffusion mechanisms in case of $\nu_0 \gg \nu_{vib}$

In this study, Raman spectra of the supporting materials were measured with a Horiba-Jobin-Yvon model LabRam Raman micro spectrometer at Analytical Chemistry Research Laboratory of the Chemistry Department at METU. It has a holographic grating having 1800 grooves mm^{-1} and HeNe laser wavelength was chosen as 632.8 nm throughout the analyses, with an exposure time of 10 s. The spectra were obtained with Olympus model LMPlanFL, 50X microscope objectives. The laser power was approximately 10 mW and Raman signal was detected with a Peltier-cooled CCD camera.

2.8 Acid-Base Back Titration

Acid-Base titration is a method widely used for the quantitative analysis of acidic or basic solutions. A back titration, or indirect titration, is generally performed in two stages. First, sample of unknown concentration is reacted with excess reactant of known concentration. Then, a direct titration is performed to determine the amount of reactant in excess, as the following example:

Sample + NaOH ➔ basic solution

excess NaOH + HCl ➔ neutral solution

The equivalence point is reached when the number of moles of NaOH remaining after the reaction with the protonic functional groups of the sample equals the number of moles of HCl added. At the endpoint of the titration, the basic solution has been neutralized by the acid as the following equation:

$$V_H^+ \times M_H^+ = n_H^+ = n_{OH-} = V_{OH}^- \times M_{OH}^-$$
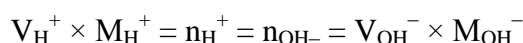
where V is the volume, M is the molarity and n is the number of moles. So, it can be expressed as:

$$n_{NaOH} \text{ Total} = n_{NaOH} \text{ neutralized by sample} + n_{NaOH} \text{ neutralized by HCl}$$

$$(V_{NaOH} \times M_{NaOH}) = (n_{NaOH} \text{ neutralized by sample}) + (V_{HCl} \times M_{HCl})$$

$$(n_{NaOH} \text{ neutralized by sample}) = (V_{NaOH} \times M_{NaOH}) - (V_{HCl} \times M_{HCl})$$

An acid-base indicator which is usually an organic dye, gives a visual indication of the acidity or basicity of a solution by color change. Since the dissociated (In⁻) and undissociated (HIn) forms gives different colors, the color depends on the dissociation of the indicator accordance with the pH of the solution, as the following equation:

$$HIn \Leftrightarrow H^+_{(aq)} + In^-$$
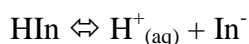
In this study, samples of supporting materials reacted with excess NaOH were titrated with HCl to determine their amount of the acidic sites. The sodium ions in NaOH are exchanged with protons of the acidic sites. Amount of the exchanged sodium ions gave the amount of acidic sites in the supporting materials. Phenolphthalein which gives pink color to the basic solutions (pH>7) was used as an indicator. At the endpoint, at pH=7, the pink color turns to colorless.

The procedure followed is as the following: 5 mg of supporting material were mixed with 5 ml 0.05 M NaOH in a sealed rounded flask and stirred continuously for 12 h

under nitrogen atmosphere by the means of a magnetic stirrer so that the sample equilibrated with the basic solution. Then 2-3 drops of phenolphthalein which gives a pink color to this basic solution were mixed; and, the solution was titrated with 0.05 HCl until the neutral point (pH 7.00) was indicated by the color change of the solution from pink to colorless. The end point was also checked by a pH meter. The amount of HCl required gave the amount of the excess NaOH which gives the amount of protonic functional groups of the sample by being subtracted from the initial amount. This procedure was performed for each supporting material one by one.

2.9 X-ray Powder Diffraction (XRD)

X-ray diffraction is the method for studying the crystalline phases of materials. The principle of the method is based on the property of X-rays to diffract on the crystallographic planes of solids (Figure 2.6).
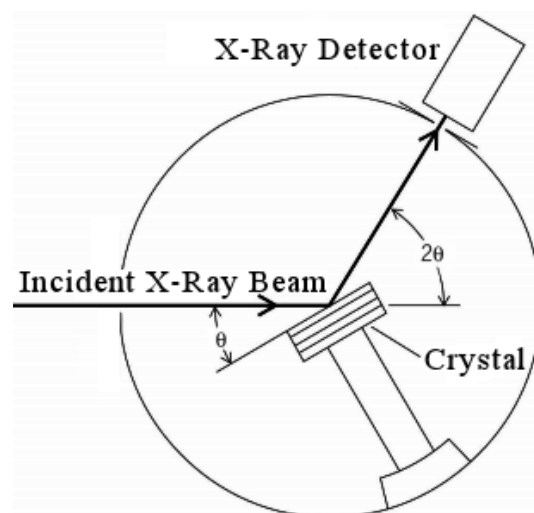

Figure 2.6. Schematic representation of XRD instrument

If a monochromatic X-ray beam is sent in the direction of a periodic organization of atoms, the photons X scattered in certain precise directions will interact together to lead to constructive interference that will cause a non-zero intensity to be seen by the detector [81].

These constructive interferences only occur when the Bragg rule is satisfied:

$$n\lambda = 2d \sin\theta$$

where n is an integer, λ is the wavelength of the incident radiation in Å, d is the interplanar distance in Å of the family of planes considered, and θ is the angle of incidence of the X-ray beam. Figure 2.7 schematizes X-ray diffraction in a crystal when the Bragg conditions are met.
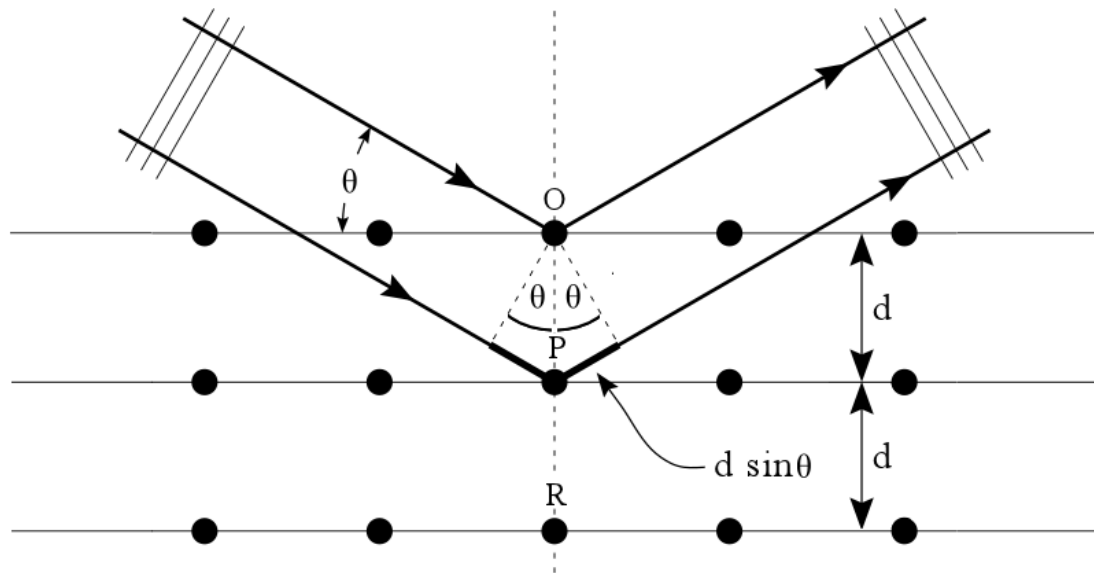

Figure 2.7. X-ray diffraction on the O, P and R atoms of the crystal planes with an interplanar distance d, at an incident angle θ

In practice, the measurement consists in varying the angle of the incident X-rays. By collecting the X-rays on a detector sensitive to the number of photons, intensity is obtained for each angle value θ where the Bragg rule applies.

The position of the peaks and their intensity contain information on the geometry of the crystal, as well as on the type of atom and the position of these in the crystal. Crystalline phases can be identified by using a reference diffractogram bank (JCPDS: Joint Committee on Powder Diffraction Standards published by the International Center for Diffraction Data). The peaks are shifted with respect to the platinum diffractogram due to the tin atoms which replace certain platinum atoms in the fcc mesh, which modifies the mesh parameter. The shape of the peaks, on the other hand, is indicative of the size of the crystallites and of the mechanical stress accumulated in them. In general, the finer peak causes the larger crystallites. In the absence of residual stress, the Scherrer rule allows us to evaluate the size of the crystallites:

$$t = (0.9 \times \lambda) / (B \times \cos\theta)$$

where t is the size of the crystallites in Å, λ is the wavelength of the incident radiation in Å, B is the mid-height width of the peak in radians on the x-axis of the diffractogram (2θ), and θ is the angle of incidence of the beam of X-rays.

In this study, Powder X-ray diffraction results were obtained by using Rigaku X-ray Diffractometer with a Miniflex goniometer operated at 30 kV and 15 mA Cu-Kα line (α=1.54 Å) as the source of X-ray, in Chemistry Department at METU.

2.10 UV-Visible Spectrometry

Absorption spectrometry (Figure 2.8) measures the intensity of a light beam which has passed through the sample (I) with respect to the intensity of an identical beam passing through the sample (I_0).
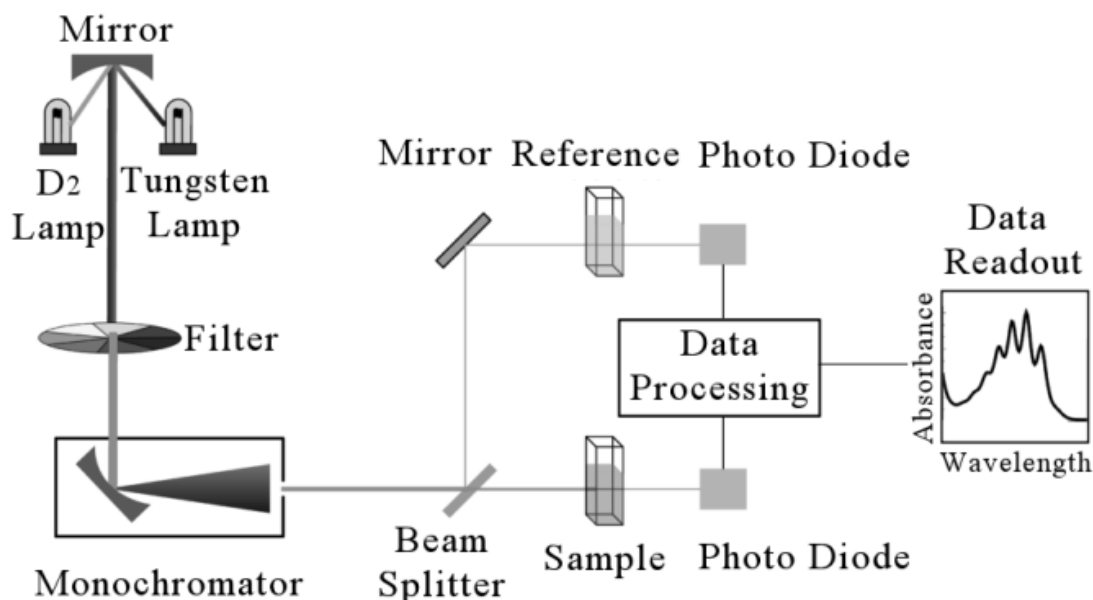

Figure 2.8. Schematic representation of UV- visible spectrophotometer

The transmittance (T) is the ratio of these intensities:

$$T\% = (I / I_{0)} \cdot 100$$

The spectra are expressed in absorbance (A) which is logarithmic and inverse to the transmittance:

$$A = \log (I_0 / I)$$

The intensity ratio is measured for each wavelength in a selected spectral range, from ultraviolet to near infrared, and the absorption spectrum is expressed in absorbance

as a function of wavelength. The resolution of the spectrum is controlled by the sampling pitch and the slit size, or spectral bandwidth [82].

In this study, UV-Visible spectrum was obtained to detect the formation of colloidal Pt particles. Measurements were carried out by Hitachi U-2800 A spectrometer in METU Chemistry Department.

2.11 X-ray Photoelectron Spectroscopy (XPS)

XPS (Figure 2.9) is a widely used surface analysis method. Although it requires complex equipment (several high vacuum chambers, X-ray sources, etc.), it is a rapid method for an elementary analysis of surface. Other advantages of the method are that no requirement for sample preparation and that becoming of the sample intact after the analysis. XPS allows characterizing the chemical composition of the surface of catalysts and also to know the state of oxidation states of the elements present.
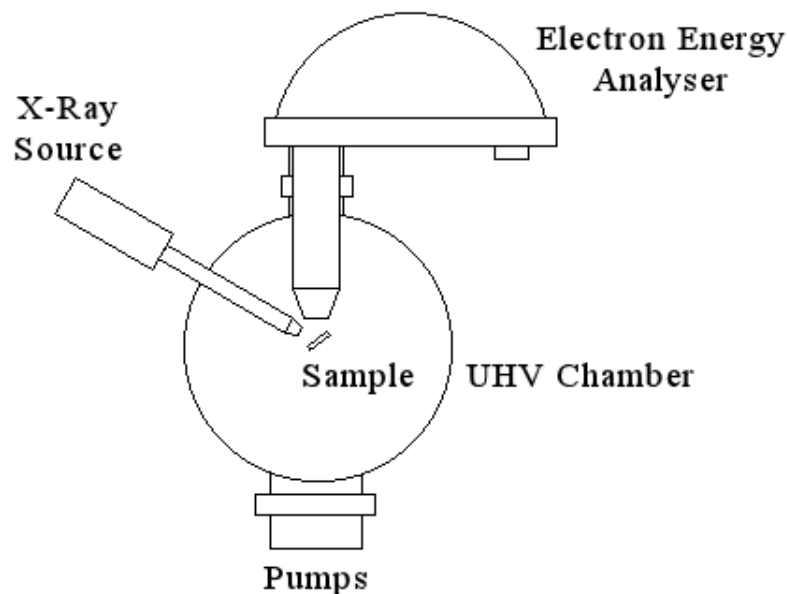

Figure 2.9. Schematic representation of XPS system

To summarize the principle, it is necessary to irradiate a sample with an X-ray source whose energy (hυ) is sufficient to ionize the atoms or surface molecules (Figure 2.10). The kinetic energy of the emitted electrons (E_k) is measured, with which it is possible to calculate the binding energy (E_b) that these have with the atom according to the following formula:

$$E_k = h\upsilon - E_b + \phi$$

Where ϕ is the work function of the spectrometer used. This kinetic energy E_k is characteristic of a certain orbital in an atom and of the oxidation state of the atom (therefore, of its chemical environment). Only the photoelectrons from the extreme surface (some atomic layers) go to the detector, since the photoelectrons emitted deeper into the material quickly lose their energy by inelastic collisions with surrounding atoms and electrons [83].
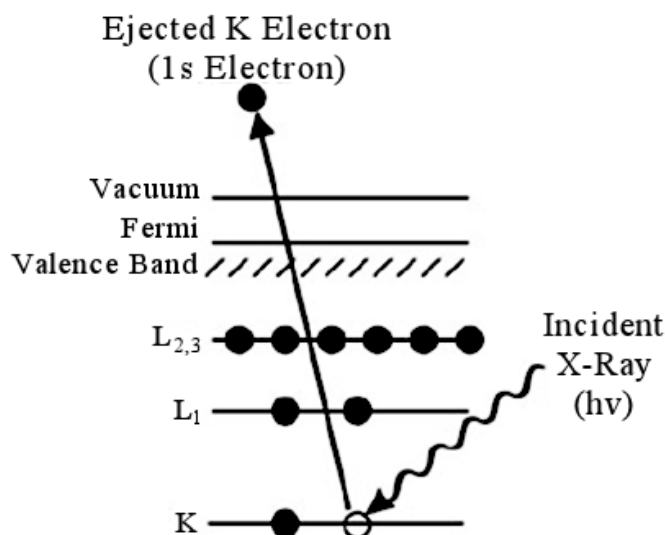

Figure 2.10. The photoemission principle involved for XPS surface analysis (discs represent electrons; bars represent energy levels within the analyzed material)

In this study, Kα lines of Mg (1253.6 eV, 10 mA) were used as X-Ray source; and, Specs-Flex Spectrometer was employed at DAYTAM, at Atatürk University.

2.12 Inductive Coupling Plasma Mass Spectrometry (ICP-MS)

ICP-MS is an essential technique for the analysis of almost all trace and ultra-trace ($mg.L^{-1}$ and $\mu g.L^{-1}$) elements in rocks, water, solids and most materials, from organic matter to electronic components. The speed of analysis, the multi-element character and the increase in the accessibility of the technique have led it to gradually replace the atomic absorption spectrometer.

In this technique, the sample to be analyzed first undergoes dissolution. The solution thus obtained is introduced into a vaporization chamber which forms a very fine aerosol with the aid of argon. The aerosol is sent in an argon plasma at very high temperature (between 5,000 and 10,000 °C.), necessary to ionize most of the elements. The ions produced are fed to the mass analyzer. The interface between the

plasma torch and the mass spectrometer consists of two successive cones. The first cone (sampler) is used to extract the ions from the plasma. The second (skimmer) allows centering the supersonic jet. Its function is to transfer a representative sample of the ion plasma to a vacuum chamber where the ions are then focused. The ions are transferred by pumping from the torch under atmospheric pressure to the quadrupole and the detector operating under vacuum. Depending on the models and the desired mass resolution performances, after separation by electric or magnetic field, the ions are detected and counted by an electron multiplier. Figure 2.11 schematically represents a typical ICP-Mass Spectrometer [84].
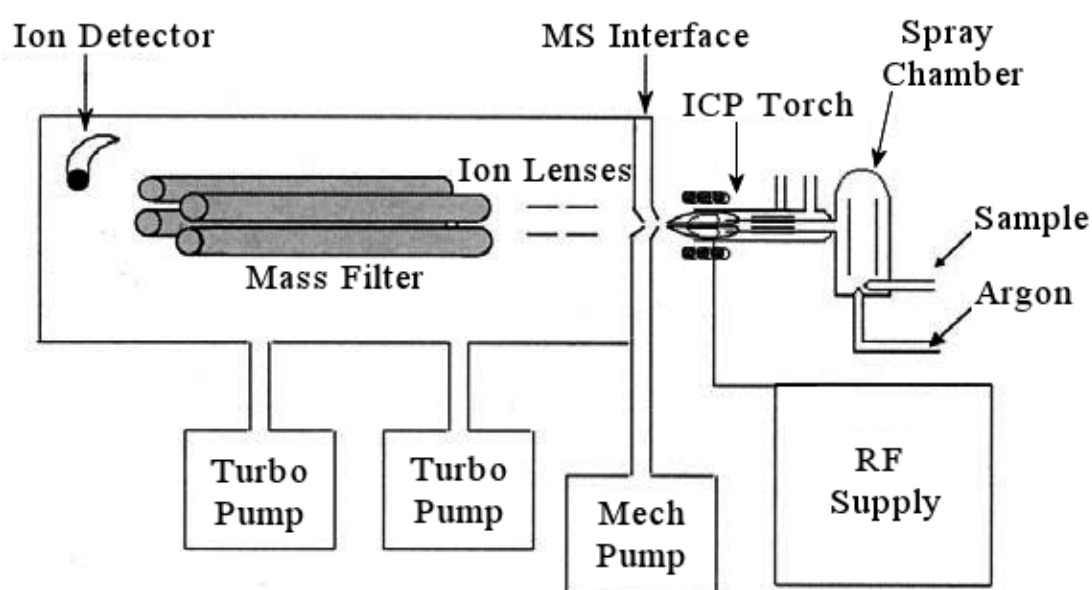
Figure 2.11. Schematic representation of ICP-Mass Spectrometer

In this study, the ICP-MS analysis was performed with Leeman Lab inductively coupled plasma spectroscopy, at METU Central Laboratory. The samples were digested in aqua regia before analyzed by ICP/MS.

2.13 Transmission Electron Microscopy (TEM)

This technique of microscopy has been used, both for the structural characterization and for making images of the nanoparticles. Transmission Electron Microscopy (TEM) can reach growths up to 1 000 000. The optical microscope uses a photon source (light), an optical lens system allows forming a light beam which passes through the sample and thus forming an image on the observer's retina. The TEM uses a source of electrons, magnetic lenses then allow to focus the incident beam of

electrons on the sample whose thickness must be very small (<100 nm) in order to allow the transmission of the incident beam [85]. The image obtained can be seen on a fluorescent screen and recorded on a photographic film or detected by a CCD (camera) sensor. The main components of a Transmission Electron Microscope are shown in Figure 2.12.

Two modes of operation are mainly used in the TEM according to whether one wants to have an image or a snapshot of diffraction [85, 86]. In the image mode, the beam of electrons passes through the sample; the electrons are more or less absorbed according to the physicochemical nature and the dimensions of the latter. In this mode, the objective lens forms an image of the object, which is further enlarged by an intermediate lens. A detector placed in the image plane then makes it possible to have an image of the irradiated zone. One of the strong points of transmission microscopy is the possibility of making images in the light field (with the transmitted beam) or in a dark field (with the different beam). This makes it possible to visualize the different phases of an alloy.

In the diffraction mode, the electrons are differentiated by the crystal lattice (analogous to the X-ray diffraction). The beam is diffracted into several small beams which recombine to form an image. A diaphragm of contrast placed at the level of the focal plane, gives a diffraction shot. A diverging diagram shows the cross-section of the reciprocal lattice, bound to the crystal, by the plane tangent to the Ewald sphere parallel to the fluorescent screen. The most intense central spot in general represents the intersection between the transmitted beam and the screen. It is chosen as the origin and always indexed by (000). The other spots on the deflecting image are at the intersection of the diffracted beams and the screen.

In this study, in order to observe the size and morphology of the synthesized Pt particles, and to determine their dispersion on the support, the electron microscopy technique was used. The samples of the catalysts were prepared by the dispersion of some piece of sample powder one by one, in ethanol in test tubes. These mixtures were ultrasonicated for 5 h in order to obtain well-dispersion. Then few drops of these mixtures were dried upon cupper grid at room temperature to use for TEM analysis. FEI brand Tecnai G2 Spirit Biotwin model High-Contrast Transmission Electron Microscopy (CTEM), operating under accelerating voltage in the range of

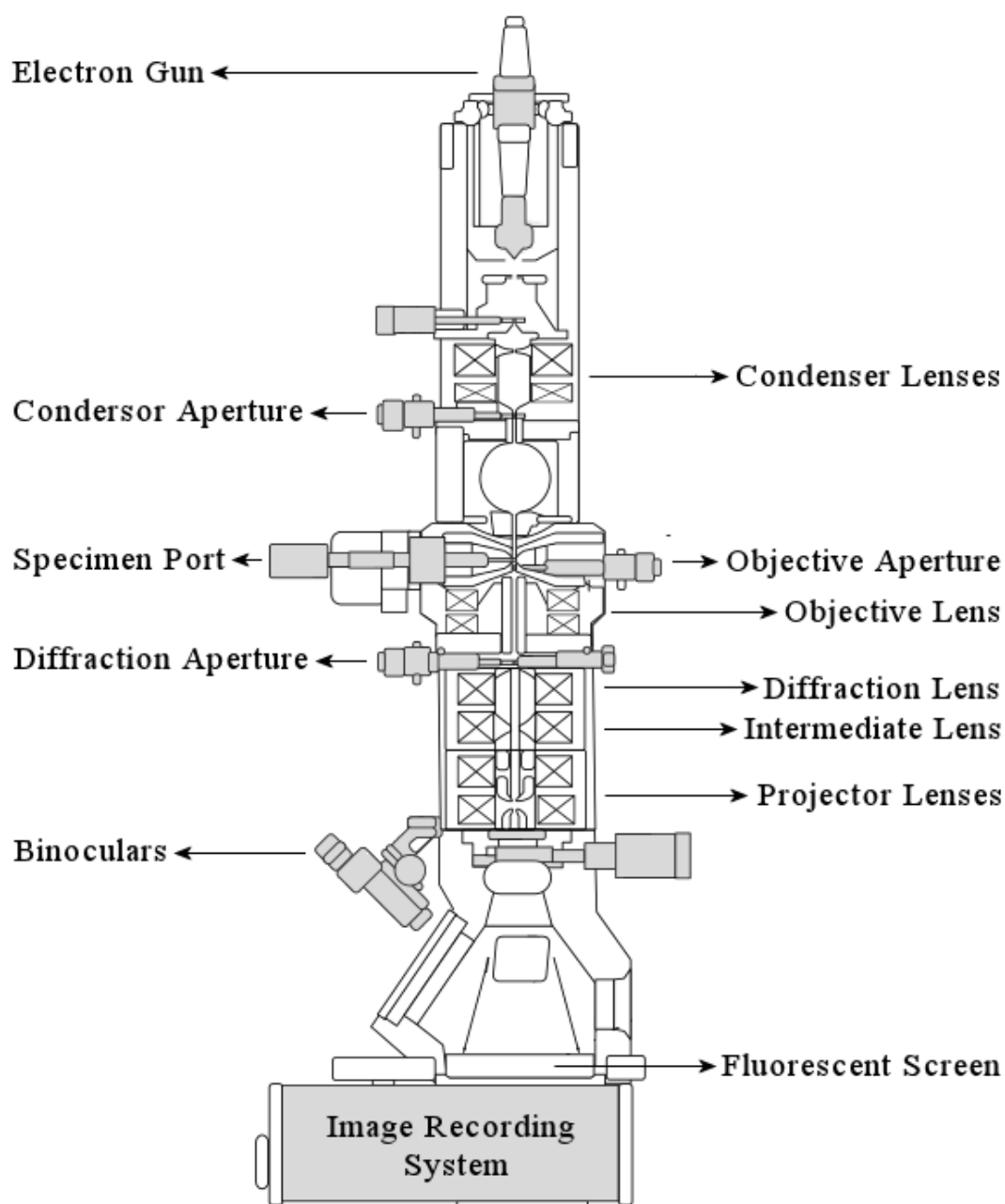20-120 kV, with a Lanthanum hexaboride (LaB$_6$) electron gun, was employed at METU Central Laboratory.

Figure 2.12. Schematic representation of TEM instrument

2.14 Cyclic Voltammetry

Linear voltage scanning voltammetry is an electrical method for the dynamic study of electrochemical systems. In this type of method, a voltage is imposed on the electrode and the temporal evolution of the current flowing through it is studied. Its most frequent use consists in performing two linear sweeps, the first one called

"forward" and the second called "reverse" in the opposite direction so as to return to the starting potential, after having thus performed a cycle. In this case, the term "cyclic voltammetry" is used, which is its standard designation [87]. Voltammetry achieves its true power only when practiced round trip is cyclic voltammetry, the principle of which is to carry out a linear flushing of potential from an initial potential Ei, such as:

$$E = E_i \pm vt$$

where v is the scanning speed, the + sign corresponds to a scan to the positive potentials, the sign - to a scan to the negative potentials.
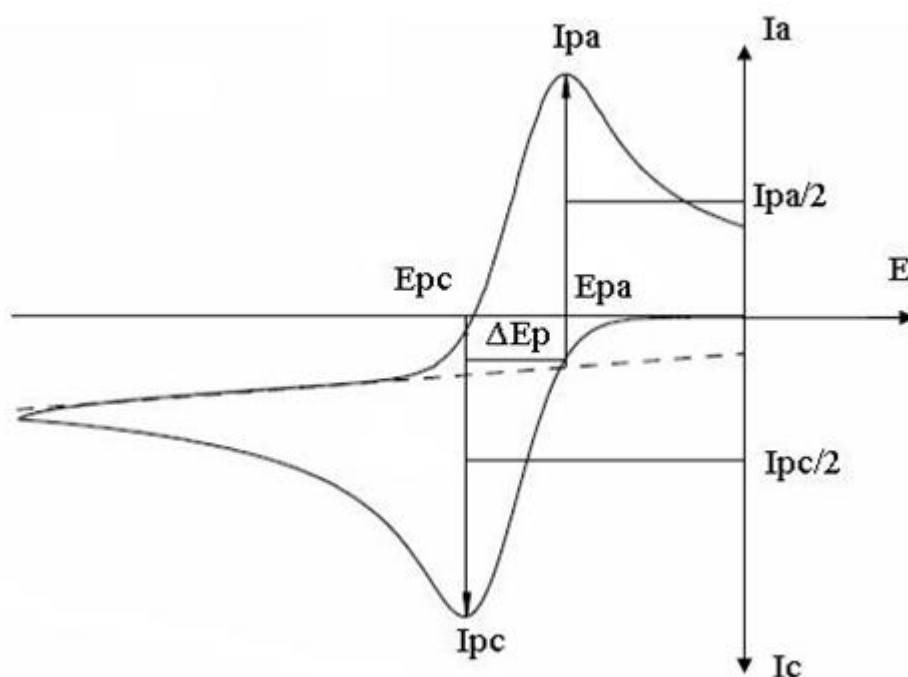

Figure 2.13. General type of a cyclic voltamperogram

The evolution of the current I (t) which passes through the electrochemical system during the voltammetry, represented on a graph as a function of the value of E (t), is called voltammograms, voltamperograms, or polarization curves. In the case of cyclic voltammetry, the direction of the sweep is indicated by arrows. Figure 2.13 shows the general form of a voltammogram I = f (E).

The characteristic quantities of a voltamperogram are Ipc and Ipa are cathode and anode peak currents respectively, whereas Epc and Epa is cathode and anode peak potentials respectively. $E_{pc}/2$ and $E_{pa}/2$ are half-height potentials of cathode and anode peaks respectively; and, ΔE_p is the potential difference between E_{pc} and E_{pa}.

Cyclic voltammetry was achieved by Gamry in Chemistry Department of METU in an electrochemical cell filled with electrolyte. As working electrode, glassy carbon with diameter of 7 mm was prepared and used. Ag/AgCl electrode was used as the reference electrode; and, the counter electrode was platinum wire (Figure 2.14). Measurements were accomplished in 0.1 M $HClO_4$ and 0.1 M $HClO_4$ + 0.5 M CH_3OH electrolyte solutions for each catalyst at room temperature.
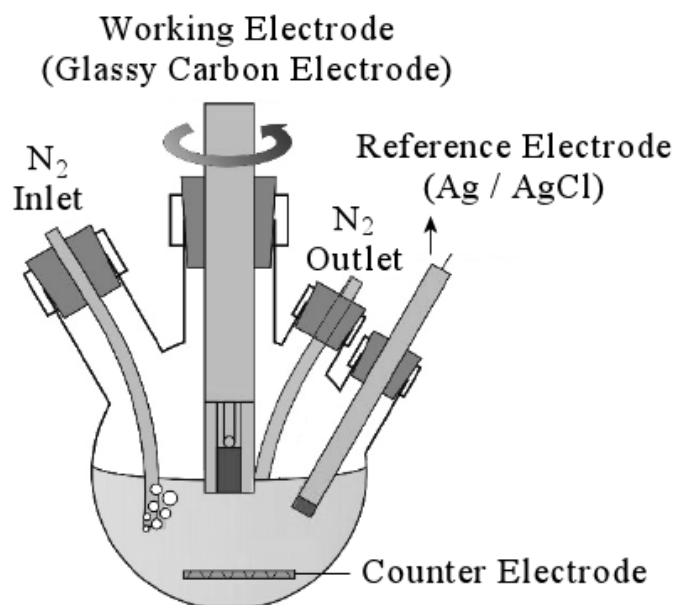

Figure 2.14. Electrochemical-cell design of CV analysis

CHAPTER 3

RESULTS AND DISCUSSION

In this study, five different electro-nanocatalysts were prepared and analyzed through their performances toward methanol oxidation reaction (MOR). In this context, five different supporting materials (graphene oxide and thiourea treated graphene oxides) were prepared, characterized; and used in impregnation procedure in order to obtain supported platinum nanoparticles.

There are various procedures that have been used to prepare GO. The oxidation method employed and the starting materials have a significant effect on the degree of oxidation, variations in the functional groups, so, on the structure and properties of GO prepared. Also, the magnitude of carbon/oxygen ratio gives the effectiveness of the oxidation process. In general, by basing on the models stated in the literature [72], GO is considered as demonstrating various oxygen functional group types distributed across aromatic regions as it is represented in Figure 3.1. In this study, as an initial step, graphene oxide (GO) was prepared by improved Hummers' method as described in the experimental chapter and were examined via FTIR in terms of demonstrated functional groups. Epoxy, hydroxyl and carboxyl groups were exhibited in FTIR spectrum of prepared GO, as explained in the related section.
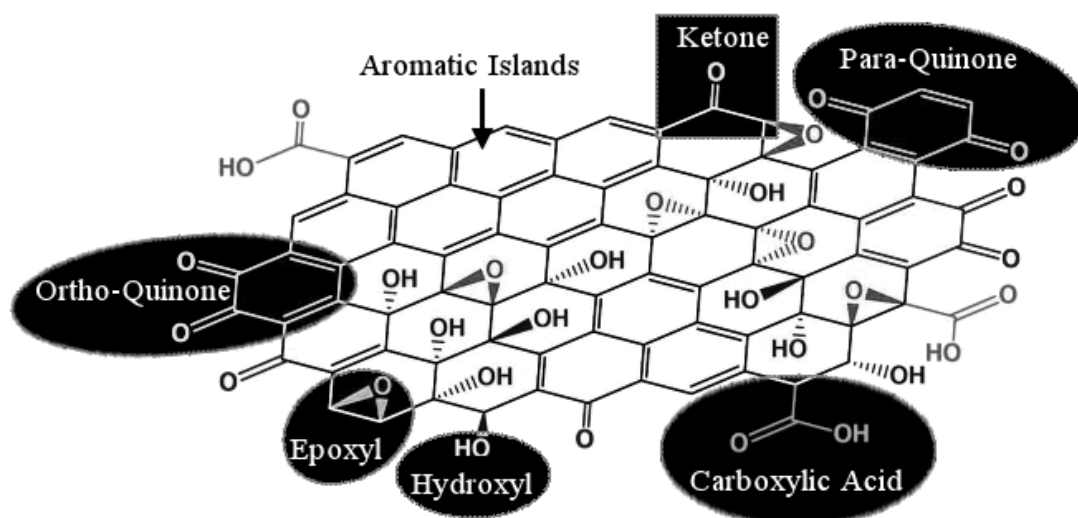

Figure 3.1. Schematic representation of graphene oxide demonstrating various oxygen functional group types distributed across aromatic regions

As a second step, TU treated GO supporting materials were prepared with respect to the durations of treatment. In this step, the graphene oxide solution was firstly treated with hydrobromic acid (HBr) with the aim of nucleophilic substitution and addition reactions on hydroxyl and epoxide groups respectively as represented in Figure 3.2. Dehydration and partial dehydrobromination events were expected as a result of simultaneous high-temperature treatment, by which brominated chemically reduced graphene is obtained. Since bromine which is less electronegative than chlorine is a better leaving group, bromination was preferred rather than chlorination.
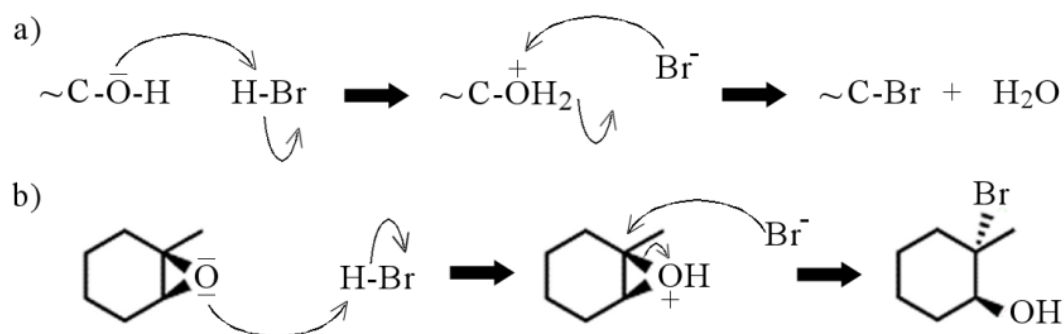

Figure 3.2. Expected bromination reaction between
a) hydroxyl groups b) epoxide groups of graphene oxide

Following that, thiourea containing a nucleophilic sulfur center added as being expected it to be reacted with the bromine moieties to form isothiouronium salts as represented in Figure 3.3. By this way, three different supporting materials were prepared as a result of the treatments for 20 minutes, 2 hours and 5 hours, respectively.
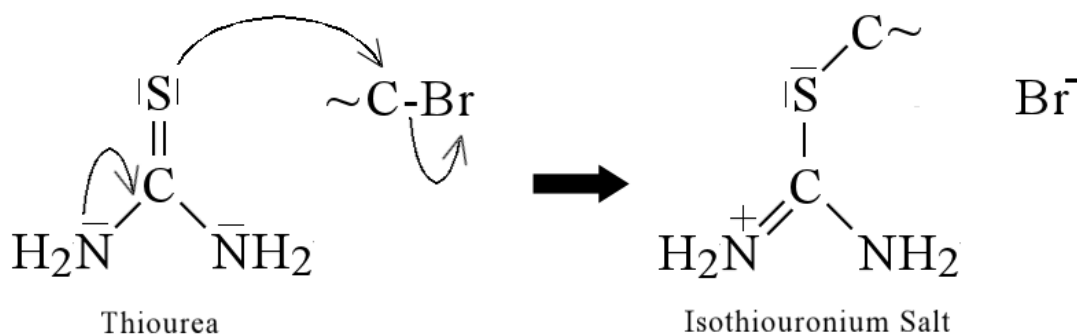

Figure 3.3. Expected reaction of thiourea with brominated groups of graphene

Then, as fifth supporting material, at the end of a treatment for 24 hours, the product was subsequently hydrolyzed by base (NaOH) treatment with an aim of obtaining

thiol-functionalized graphene, as represented in Figure 3.4. These five different supporting materials and prepared nanocatalyts were characterized and analyzed via several techniques.
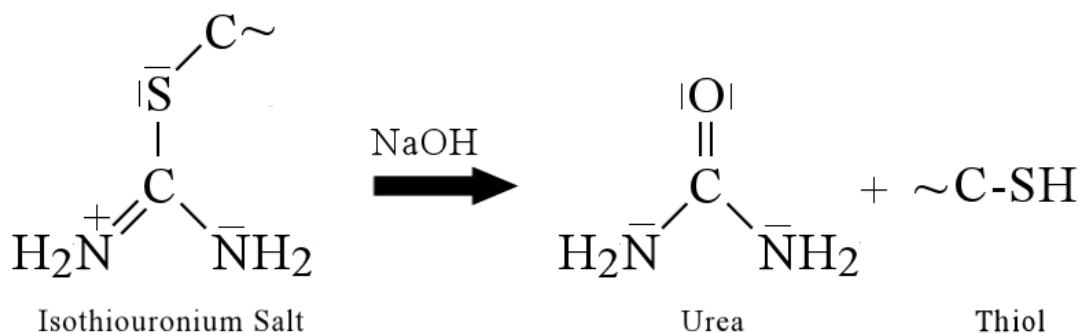

Figure 3.4. Expected thiol formation with addition of NaOH to 24 h TU treated GO

3.1 Characterization by FTIR

The prepared supporting materials were initially characterized by FTIR spectroscopy. Also, samples of different durations as intermediate steps were characterized to observe the change accordance with treatment duration. The Fourier Transform Infrared Spectroscopy (FTIR) deals with the stretching, bending, bonding and wiggle responses of molecular species in a given sample. As shown in Figure 3.5, the spectrums were characterized by relevant molecular stretching and bending vibrations.

In the spectrum of thiourea [88], the absorption bands at 3362, 3259, 3155 cm^{-1} are assigned to NH_2 stretching vibration, while the NH_2 bending vibration is observed at 1605 cm^{-1}. The band at 1483 cm^{-1} is assigned to N–C–N asymmetric stretching vibration. The C=S asymmetric stretching mode is observed at 1405 cm^{-1}, and the N-C-N symmetric stretching mode is observed at 1121 cm^{-1}. The characteristic band at 750 cm^{-1} is assigned to C=S symmetric stretching vibration. At 526 cm^{-1}, the N-C-N asymmetric bending mode is observed.

In the spectrum of graphene oxide [89], the peak corresponding to 3390 cm^{-1} is assigned to O-H stretching and is prominent for GO owing to the presence of a large number of hydroxyl groups in the GO backbone. The C=O stretching vibration of −COOH groups varies between 1720 and 1760 cm^{-1}, indicates a variable conjugation of carbonyls in the product. In the spectrum of GO, the band at 1754 cm^{-1} belongs to the stretching vibration of carbonyl residue (C=O). The peak at 1418 cm^{-1} is ascribed

to the carboxy group as being corresponding to the O–H stretching and bending vibration. The epoxy and alkoxy residues give the absorbance band at 1250 and 1078 cm^{-1} respectively. The characteristic peak at 1642 cm^{-1} in the GO spectrum was due to aromatic C = C stretching.
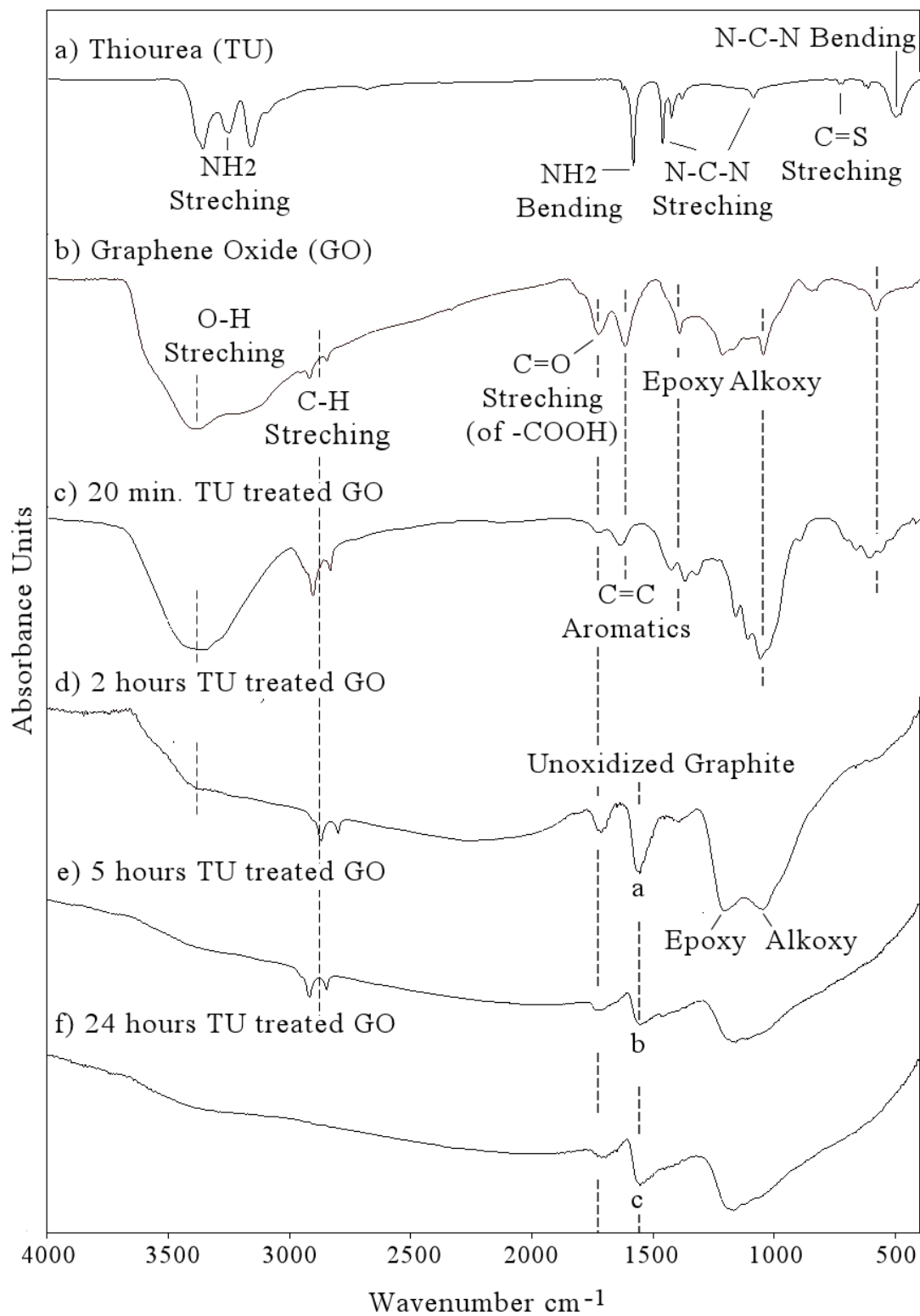
Figure 3.5. FTIR spectra of thiourea and five different supporting materials

Pumera [90] suggests that large peak at 1600 cm^{-1} corresponds to the unoxidized sp^2 regions but in fact signal slightly above 1600 cm^{-1} is more often attributed to OH groups while signal around 1580 cm^{-1}, very common in less-oxidized graphite, may result from sp^2 domains. Here, the band strength at 1645 cm^{-1} varies from sample to sample. This band has been associated with the degree of reduction when compared to that of the starting material.

The reduced GO spectrum [89], as 24 h TU treated GO spectrum, exhibits only three peaks at 1185 cm^{-1} assigned to C–O vibration and 1551 cm^{-1} assigned to C=C vibration, and a weak peak assigned to carbonyl residue which suggests that the GO has been reduced during the process. It is the skeletal vibration from unoxidized graphitic domains which displays its characteristic band at 1586 cm^{-1} as stated above. Intensities of this band at 1586 cm^{-1} for 2, 5 and 24 hours TU treated GOs labeled as a, b, c respectively in Figure 3.5, indicates that 2 hours TU treated GO consist more unoxidized graphitic domains (sp^2).

In the spectrum of 20 minutes TU treated GO, differences in the peaks of epoxy and alkoxy groups were observed compared to GO spectrum, which may be a result of bromination process targeting the epoxy and hydroxyl groups explained above. The stretching vibrations assigned to the C-S linkage are expected in the region of 800 - 600 cm^{-1}. The weakness of absorption and variability of position make this band of little value in structural determination. After the addition of thiourea, in the spectrum of 20 minutes TU treated GO, weak peaks in this region were appeared which may be the result of nucleophilic addition of thiourea.

In order to observe the change of the products in accordance with treatment duration, samples from intermediate steps treated for different durations were also characterized as seen in Figure 3.6. As soon as thiourea is added, the signal appears at 1390 cm^{-1} may be associated with a deformation vibration of the O-H bond (deformation in the plane of the O-H bond in C-OH), is present at the earlier times of the treatment while it is completely absent in the samples which are reduced in higher degrees (5h and 24h). In an overview, it is seen that changes in the regions labeled as x, y and z in Figure 3.6, indicates the attachment of thiourea on the surface of GO at the beginning of the treatment. At longer treatment durations, the decreasing degree of reduction can also be observed in the spectrums.
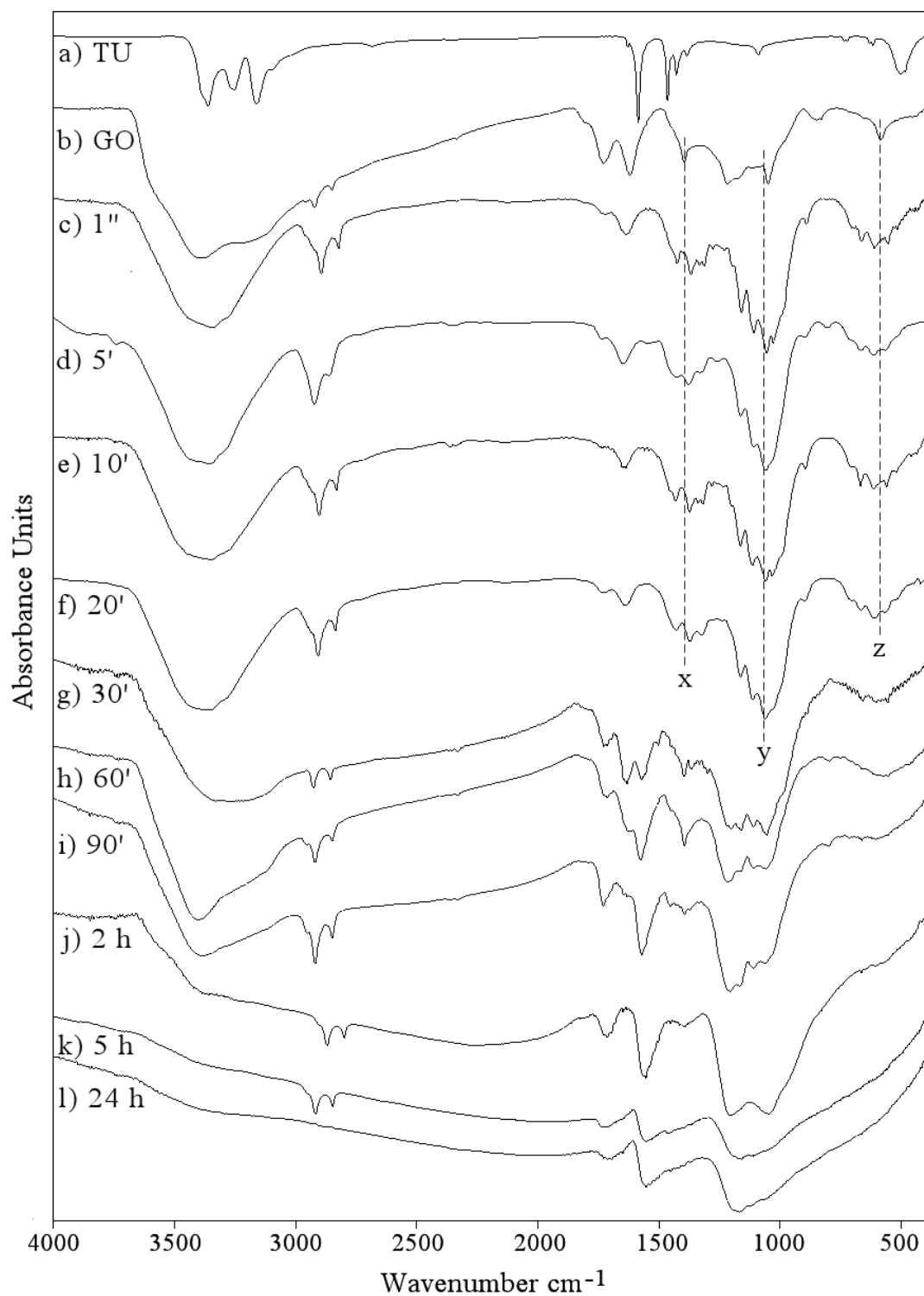
Figure 3.6. FTIR spectrum of TU-treated GOs for different durations

As the degree of reduction by thiourea is increasing, almost all the characteristic peaks weakened and some even disappeared. In the spectra of 5 hours and 24 hours TU treated GO, the intensity of peaks at 3400, 1750, and 1390 cm^{-1} decreased dramatically, demonstrating the removal of oxygen-containing functional groups to a certain degree.

72

3.2 Characterization by Raman Spectroscopy

Raman spectroscopy is a popular technique for characterization of the structural and electronic properties of graphene, such as disorder and defect structures, defect density, and doping levels. Raman spectroscopy of graphene is generally characterized by G and D bands. The G-peak arising from first-order scattering of the E_{2g} phonon from sp^2 carbon atoms is generally observed at 1590 cm^{-1}; whereas the D-peak arising from breathing mode of κ-point photons of A_{1g} symmetry is generally observed at 1340 cm^{-1}.

It is seen in Figure 3.7 that the G-band and D-band of GO appeared at 1600 cm^{-1} and 1339 cm^{-1}, respectively. The spectra supported the structural change of GO after the treatment by TU. In the Raman spectrum of GO, after 24h TU treatment, the D-band shifted to around 1325 cm^{-1}, whereas the G-band shifted to 1576 cm^{-1}. Becoming prominent of the D-band at 1325 cm^{-1} indicates the reduction in size of the in-plane sp^2 domains. GO spectrums after reduction by TU showed a higher D/G intensity ratio than GO. Compared to pure GO, the D/G ratio of the 24 h TU treated GO increased significantly from 1.17 to 1.50, indicating the introduction of sp^3 defects after functionalization and incomplete recovery of the structure of graphene [91].

The ratio of intensity of D/G bands is a measure of the defects present on graphene structure. The G band is a result of in-plane vibrations of sp^2 bonded carbon atoms whereas the D band is due to out of plane vibrations attributed to the presence of structural defects. If the spectra of graphene and graphene oxide is compared, GO has a higher D band due to the disruption of sp^2 bonds of the carbon since GO has oxidative functional groups. So, if the D band is higher, it can be interpreted that the sp^2 bonds are broken which in turn means that there are more sp^3 bonds. However, D band can be present due to various other reasons. So, if D/G ratio is higher than that of graphene, it means that there are defects. It does not indicate that there is more sp^3 than sp^2 in the same sample; indeed, it shows that there is more sp^3 in GO compared to graphene [92]. The variation of relative intensities of the G-band and D-band in the spectra of the GO during the reduction usually demonstrates the change of the electronic conjugation state. This change indicates an increase in the number of sp^2 domains after reduction of GO. Stankovich et al. suggested that reduction of GO increases the number of aromatic domains of smaller average size in graphene, which could lead to an increase of the ID/IG ratio.
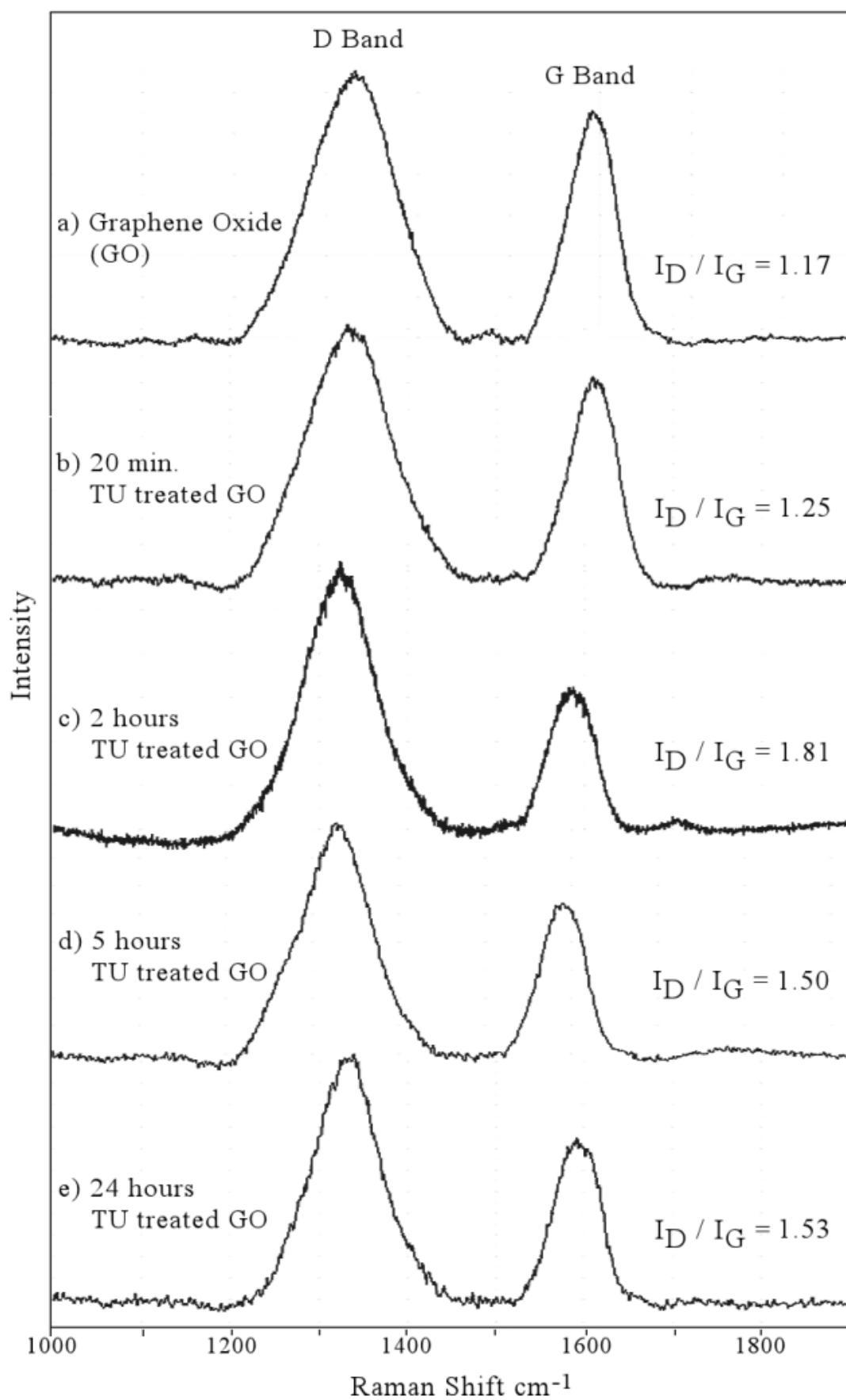
Figure 3.7. Raman spectra of the supporting materials

In other words, the intensity of the D band is related to the size of the in-plane sp^2 domains. The D band is related to the structural defects or partially disordered graphitic domains. A strong D band indicates formation of more sp^2 domains and also confirms the presence of lattice distortions of graphene basal planes. The relative intensity ratio of both peaks (I_D/I_G) is a measure of disorder degree and is inversely proportional to the average size of the sp^2 clusters. I_D/I_G intensity ratio for reduced GO (r-GO) is larger than that for GO, which indicates loss of graphitic structures. The increased I_D/I_G ratio in r-GO indicates establishment of graphene domains by the reduction of graphene oxide, but the domains were of lesser size compared to preceding graphite phase.

In Figure 3.7, the GO sample shows a prominent D peak with an I_D/I_G of 1.17 indicative of structural disorder created due to the presence of oxygen functional groups. The highest I_D/I_G (1.81) is observed for 2 h treated GO. An increased D/G intensity ratio compared to that of GO suggests a decrease in the average size of the sp^2 domains upon reduction of the GO, and can be explained if new graphitic domains were created that are smaller in size to the ones present in GO before reduction, but more numerous in number. In fact, it is seen in FTIR spectrum that 2 h TU treated GO has higher unoxidized graphite peak than 5 h and 24 h TU treated GO at at 1586 cm^{-1}. If the trend is taken into account, it is seen that D/G ratio increases after the addition of thiourea to second hour of the treatment at which the high ratio (1.81) is observed. Afterwards, at fifth and twenty-fourth hours, it decreases to 1.5. In an overview, all of the TU treated supporting materials are observed at a higher ratio of D/G which may explain higher activity of nanocatalysts supported by them toward methanol oxidation reaction than GO supported nanocatalysts, due to the higher degrees of adsorption of platinum.

3.3 Acid-Base Back Titration

In order to acquire more information about the functional groups of the supporting materials, acid-base back titration method was used to calculate the ratio of carboxyl and hydroxyl functional groups. The samples of supporting materials were treated with NaOH as expecting the following reaction:

$$G\text{-COOH or } G\text{-COH} + NaOH_{(excess)} \rightarrow G\text{-COO}^-Na^+ \text{ or } G\text{-CO}^-Na^+ + H_2O + NaOH$$
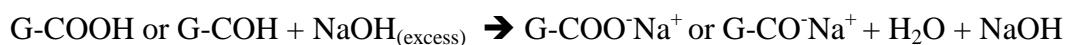
Next, when the solutions were titrated with HCl, the amount of NaOH was determined at the end point and its difference from the initial amount of NaOH gave the amount of Na^+ exchanged which gives the amount of hydroxyl and carboxyl functional groups. As a result (Table 1.1), the highest ratio was found for GO (36 %) as expected. The decreased ratios are seen consistent with the partially reduction of GOs in accordance with treatment durations.

Table 1.1. The ratio of protonic functional groups of supporting materials

Type of Nanocatalyst	-COOH % + -OH %
Pt / GO	36
Pt / 20 min. TU treated GO	28
Pt / 2 h. TU treated GO	29
Pt / 5 h. TU treated GO	24
Pt / 24 h. TU treated GO	23

3.4 Characterization by UV-Vis Spectroscopy

After the supported Pt nanocatalysts were prepared by impregnation method and H_2 reduction, initially characterized via UV-Vis spectroscopy. The absorption peaks at 258 nm corresponding to the absorption of Pt(IV) species disappeared (Figure 3.8) indicating the reduction of Pt(IV) species and the existence of Pt(0) particles [93].
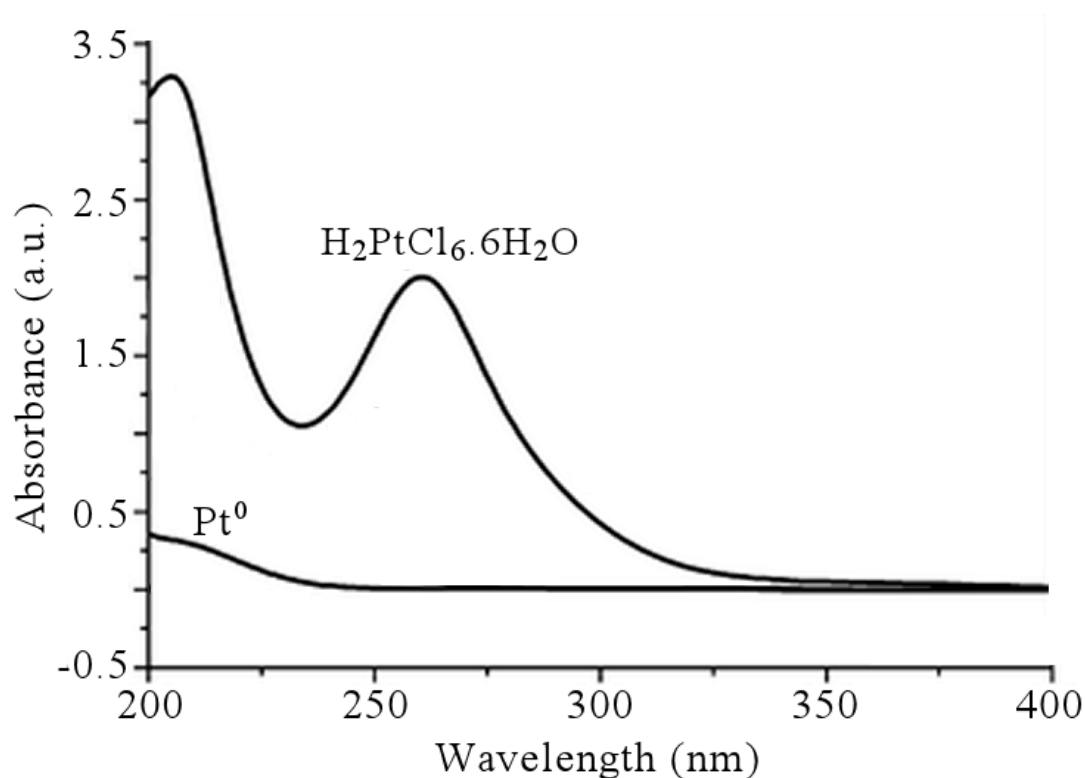

Figure 3.8. UV-Vis spectra of $H_2PtCl_6.6H_2O$ and prepared nanocatalysts

3.5 Characterization by XRD

Layer spacing of supporting materials and crystal structures of prepared nanocatalysts were examined via XRD. The faced center cubic (fcc) crystalline structure of Pt(0) was displayed in X-ray powder diffraction patterns of all prepared nanocatalysts (Figure 3.9). The broad reflections indicated the nanocrystalline natures of the samples. In the XRD patterns of nanocatalysts, the broad diffraction peaks at 2θ = 39.9, 46.3, 67.5, and 81.2, are assigned to Pt (111), Pt (200), Pt (220), and Pt (311) respectively, as being consistent with the fcc structure of platinum [94].

The nanocrystallite size of the Pt(0) were calculated and reported in Table 3.2, by measuring the full width at half maximum (FWHM) of the peak in radian, via the Scherrer equation:

$$\text{Particle Size} = (0.9 \times \lambda) / (d \times \cos\theta)$$

where λ = 1.54060 Å (in the case of CuKα1 radiation); so, 0.9. λ = 1.38654, θ is the $2\theta/2$, and d is the full width at half maximum intensity of the peak in radian. In order to convert angle to radian:

$$\text{Rad} = (22 \times \text{angle in degree}) / (7 \times 180) = \text{angle in degree} \times 0.01746$$

Table 3.2. Particle sizes calculated by Scherrer equation

Type of Nanocatalyst	2θ=39.9	2θ=46.8	2θ=68	2θ=81.2	Average
Pt / GO	5.05 nm	5.17 nm	3.58 nm	3.12 nm	4.23 nm
Pt / 20 min. TU treated GO	4.21 nm	4.31 nm	3.17 nm	2.4 nm	3.52 nm
Pt / 2 h. TU treated GO	5.05 nm	5.17 nm	3.9 nm	3.47 nm	4.39 nm
Pt / 5 h. TU treated GO	4.21 nm	3.68 nm	3.17 nm	3.12 nm	3.54 nm
Pt / 24 h. TU treated GO	5.05 nm	4.31 nm	4.77 nm	4.45 nm	4.64 nm

The average particle sizes of 20 min. and 5 hours TU treated GO are found more smaller than the others as being consistent with their activities calculated in the section of cyclic voltammetry. The increase in the particle sizes is related to the modification of the surface of supporting materials. Oxygen, nitrogen and sulphur functional groups increase the dispersion of the precursor on supporting material. This is due to the increase in the electrostatic adsorption of the anionic precursor on the surface of the supporting material. The increased dispersion may lead to monodispersed smaller particles of the 20 min and 5 h TU treated GO particles.
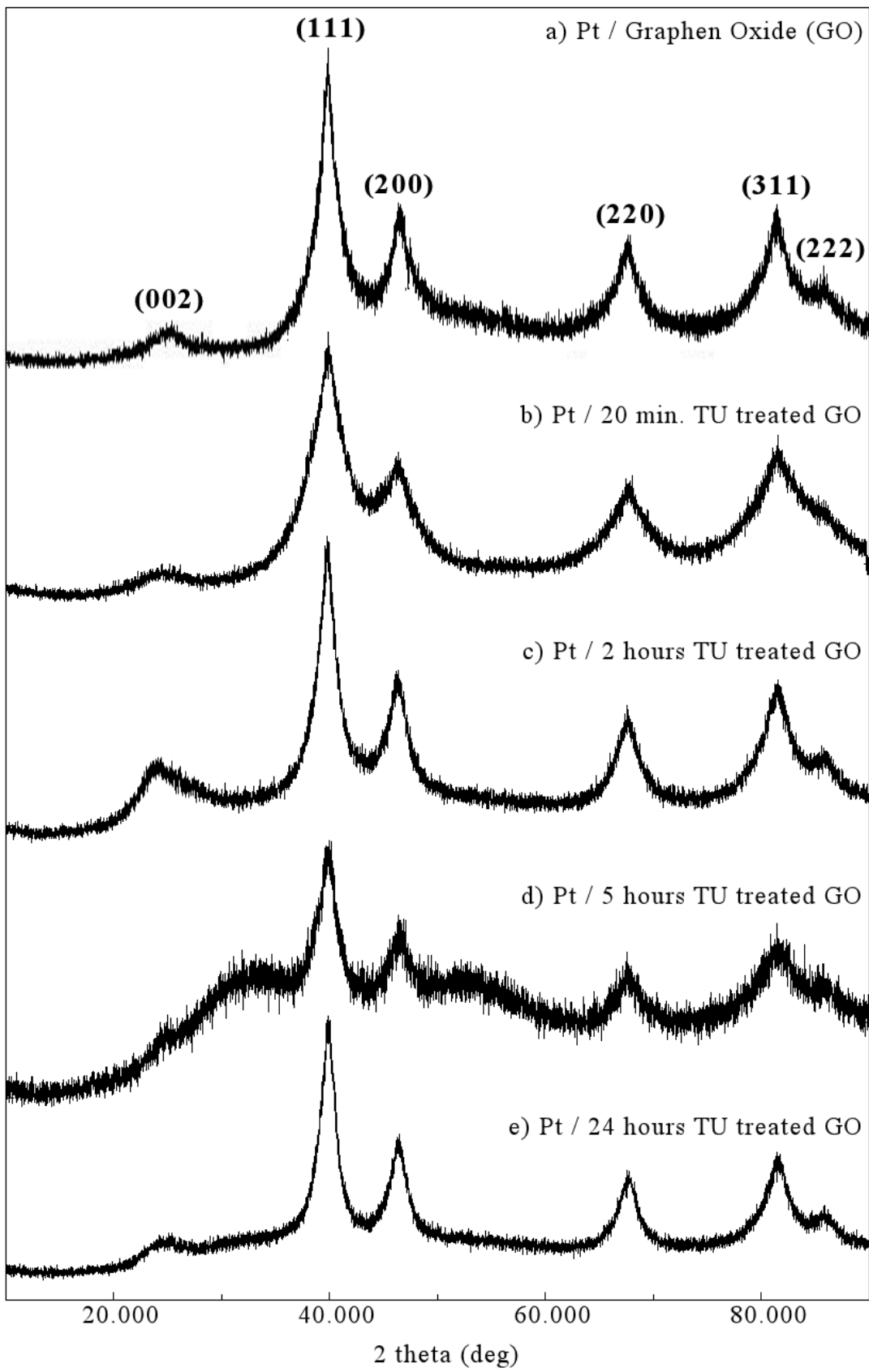
Figure 3.9. XRD patterns of Pt / supporting materials

The increase in size of the particles is also related with the platinum amount. In the nucleation and growth process, adsorption of higher quantities of the precursor on the surface of supporting material causes larger growth of the formed Pt nanoparticles. In general, higher platinum percentage in the catalysts causes larger platinum particle size resulting in lower platinum surface area. The relative amounts of prepared nanocatalysts were determined by ICP-MS as stated in the related section.

On the other hand, in the XRD patterns, the first peaks labelled as C (002) which vary at between 24°-26°, is graphite peak corresponding to the graphene structure. Pt/GO and Pt/partially reduced GOs exhibit a weak and broad diffraction peak at about $24.1^o - 25.5^o$ in their XRD patterns [95]. Diffraction peak of graphene oxide at 12.6^o becomes broader and shifts to higher degrees as a result of the significant decrease in spacing due to the loss of oxygen functional groups from the interlayer of graphene oxide. In the spectrum of GO and TU treated GO (Figure 3.10), diffraction peak of graphene oxide becomes broader and shifts to higher degrees after treatment with TU, indicating that there is a decrease in the amount of functional groups as a result of partially reduction during the treatment by thiourea.
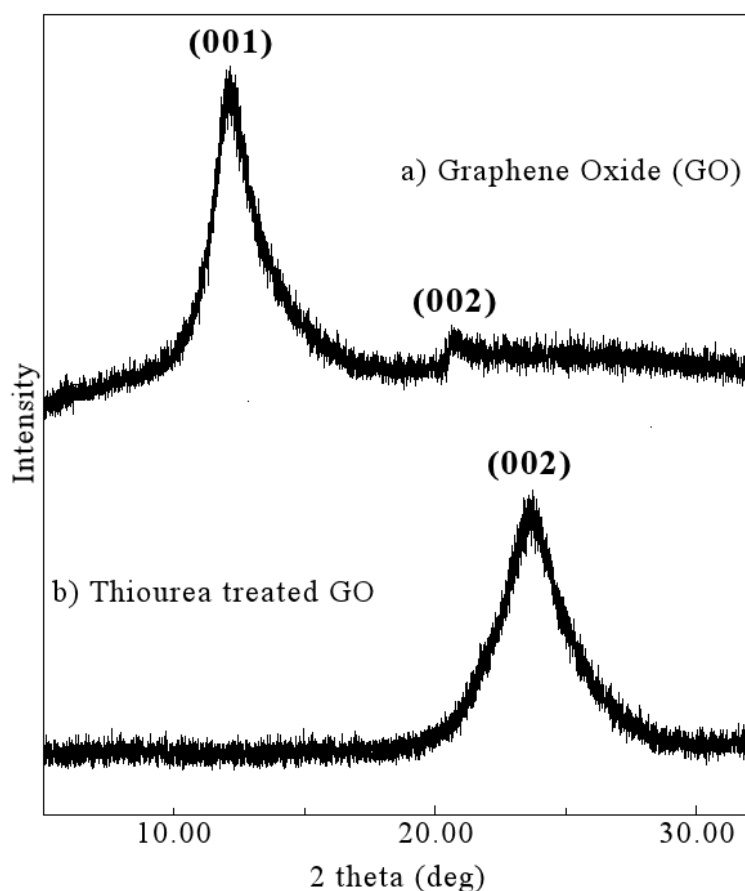

Figure 3.10. XRD patterns of GO and TU-treated GO

79

The layer spacing of between supporting materials are calculated (Table 3.3) by the means of Bragg equation:

$$\lambda = 2d\sin(\theta)$$

where λ is the wavelength of the X-ray beam (0.154nm), d is the distance between graphite oxide or reduced graphene oxide adjacent sheets or layers, and θ is the diffraction angle. In order to calculate layer spacing (d), Bragg equation can be rewritten as following:

$$d = \lambda/2 \sin(\theta) = 0.154nm / 2 \sin(\theta)$$

Table 3.3. Layer spacing distances of prepared nanocatalysts

Type of Nanocatalyst	2θ (^{o})	Layer Spacing
Pt / GO	25.5	0.35 nm
Pt / 20 min. TU treated GO	24.7	0.36 nm
Pt / 2 h. TU treated GO	24.1	0.37 nm
Pt / 5 h. TU treated GO	25	0.36 nm
Pt / 24 h. TU treated GO	25	0.36 nm

The layer distance of reduced GO and graphite is theoretically almost same. The difference between graphite and reduced GO is that graphite is a three dimensional, layered carbon allotrope, where layers are consists of carbon atoms arranged in a honeycomb fashion and where each layer is connected through van der wall's interaction. However, here, reduced GO is prepared from the reduction of graphene oxide, that is to say that layers are already detached by chemical methods. Reduced GO tries to attain the sp^2 carbon network back as it is in graphene (single layer of graphite) but some defects caused from oxidation or incomplete reduction are inevitable. So, there are still some oxygen functional groups in or on the reduced graphene oxide surface. Secondly, in comparison with graphite and reduced GO, later consists of smaller domain of sp^2 carbon network since defects and other oxygen functional groups present in the reduced GO sheet. As a result, XRD peak becomes broad and less intense (loss of crystallinity) compared to graphite. Thirdly, the reduced GO exhibits better electrochemical performance as it has high surface area (enhanced capacitance), oxygen functional groups in or on the surface (better adsorption) and moreover, it is layered and electronically conducting, considered as an efficient alternative to graphite in material chemistry.

3.6 Inductively Coupled Plasma Mass Spectrometry (ICP-MS)

The amounts of sulphur and platinum in prepared nanocatalysts were determined via Inductively Coupled Plasma Mass Spectrometry. The percentages for each nanocatalyst are reported in Table 3.4.

Table 3.4. Sulphur and platinum ratios of prepared nanocatalysts

Type of Nanocatalyst	Pt (%)	S(%)
Pt / GO	26.9 ± 0.2	1.2 ± 0.1
Pt / 20 min. TU treated GO	32.9 ± 0.2	8.5 ± 0.2
Pt / 2 h. TU treated GO	35.3 ± 0.2	6.2 ± 0.3
Pt / 5 h. TU treated GO	33.4 ± 0.2	6.9 ± 0.1
Pt / 24 h. TU treated GO	30.1 ± 0.2	8.7 ± 0.2

It is seen that these determined Pt percentages of TU treated supporting materials are a bit higher than the theoretical percentage (%30) calculated from the amount of chloroplatinic acid ($H_2PtCl_6.H_2O$) used in impregnation process. These increased percentages may indicate the loss of some supporting materials in the H_2 reduction process due to the high temperature (210 C^o).

Also, platinum amounts for each catalyst on one electrode are calculated by basing on the percentages obtained by ICP-MS method (Table 3.5). These electrodes were than employed for electrochemical analysis (cyclic voltammetry method) explained in related section.

Table 3.5. Amount of platinum on one electrode

Type of Nanocatalyst	Amount of Platinum on One Electrode
Pt / GO	10.53×10^{-5} g/cm^2
Pt / 20 min. TU treated GO	13.07×10^{-5} g/cm^2
Pt / 2 h. TU treated GO	14.02×10^{-5} g/cm^2
Pt / 5 h. TU treated GO	13.50×10^{-5} g/cm^2
Pt / 24 h. TU treated GO	11.95×10^{-5} g/cm^2

3.7 Characterization by TEM

Transmission Electron Microscopy (TEM) provided direct imaging of nanomaterials to obtain quantitative measures of particle sizes, size distributions and morphologies. The TEM images of the prepared nanocatalysts (Figure 3.11) displayed the general distributions, particle sizes and the ratios of agglomeration.
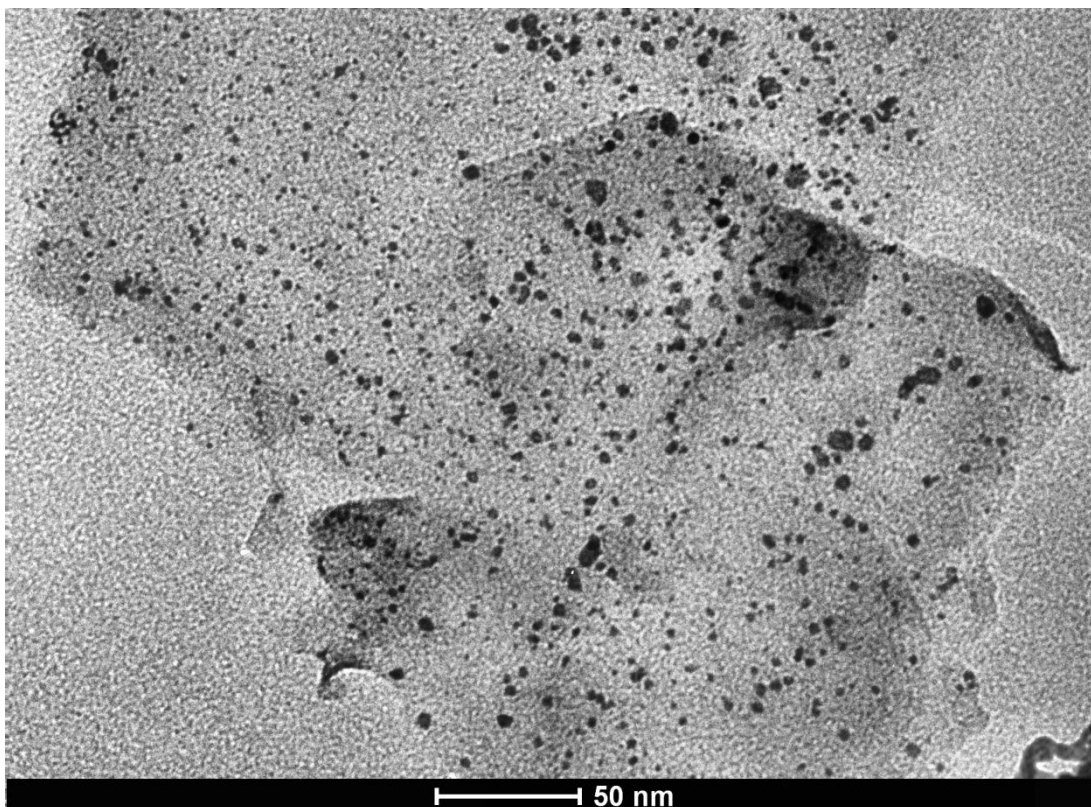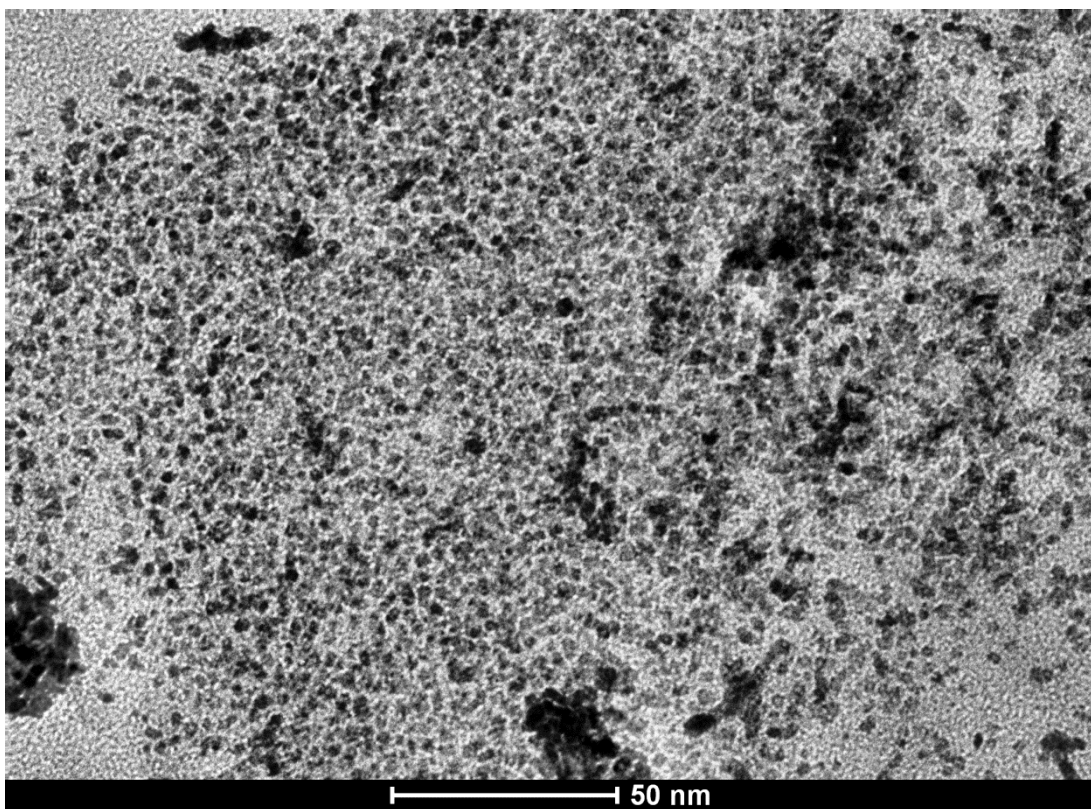
Figure 3.11.a. TEM image of Pt / GO

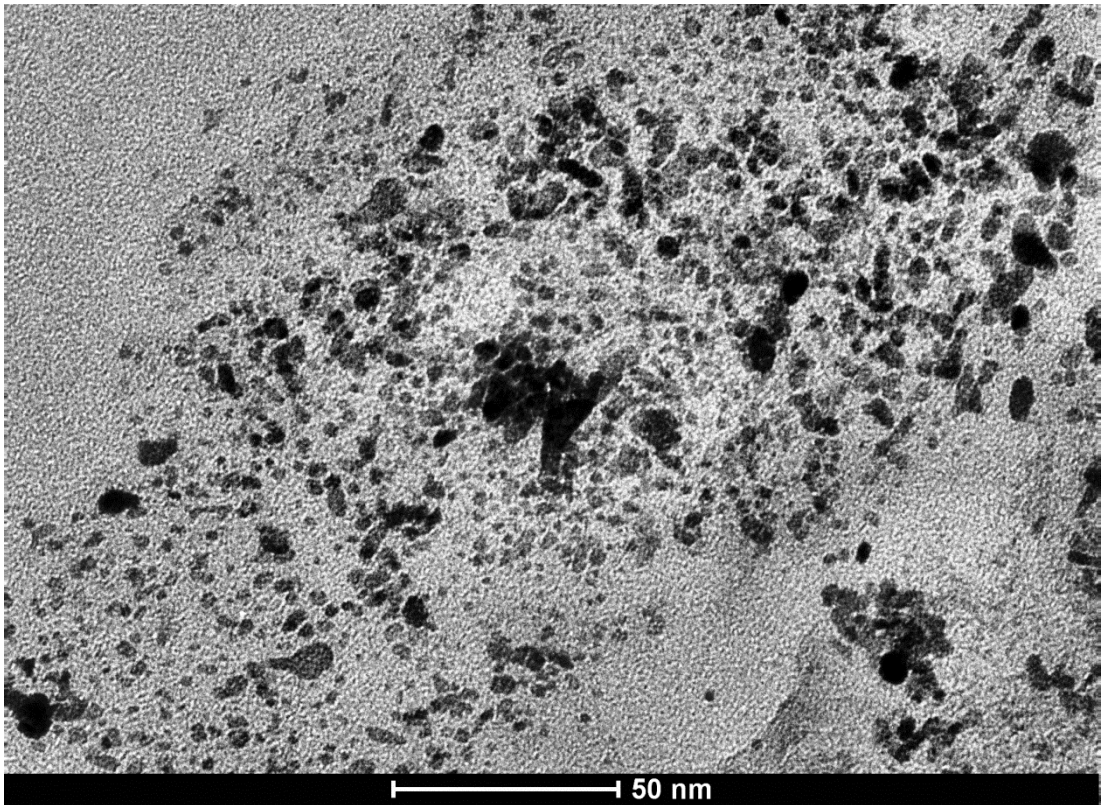Figure 3.11.b. TEM image of Pt / 20 min TU treated GO

50 nm

Figure 3.11.c. TEM image of Pt / 2 h TU treated GO
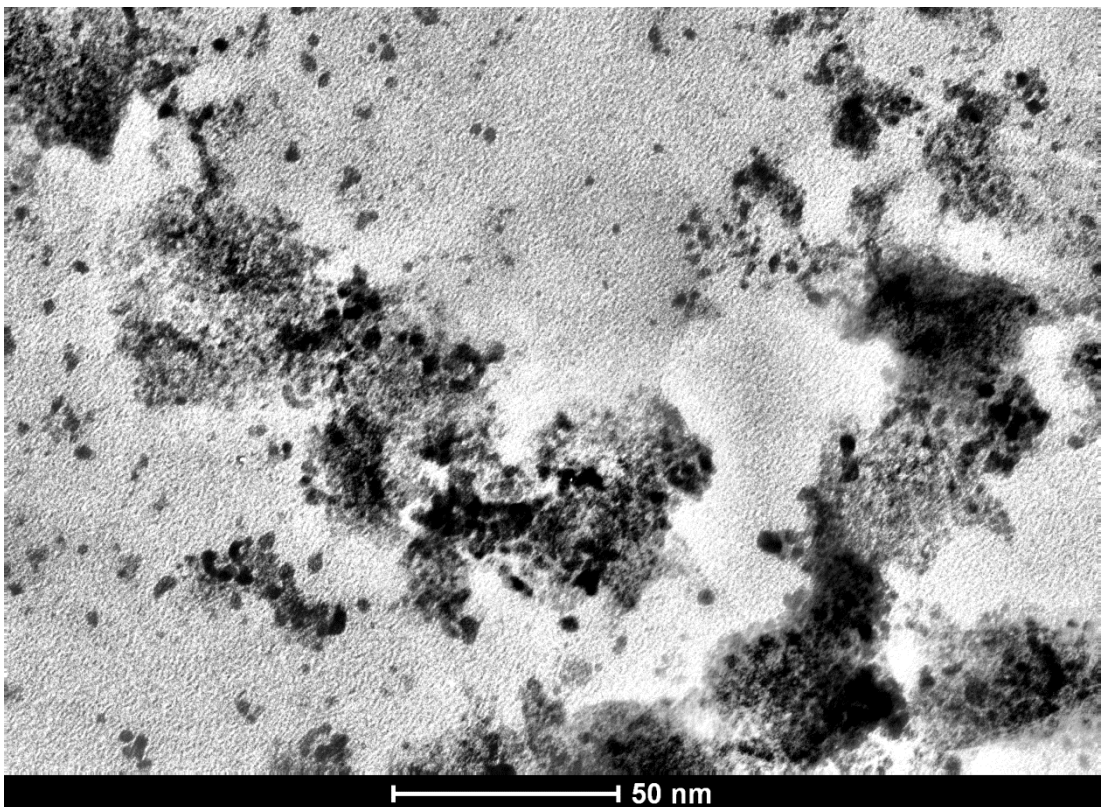

50 nm

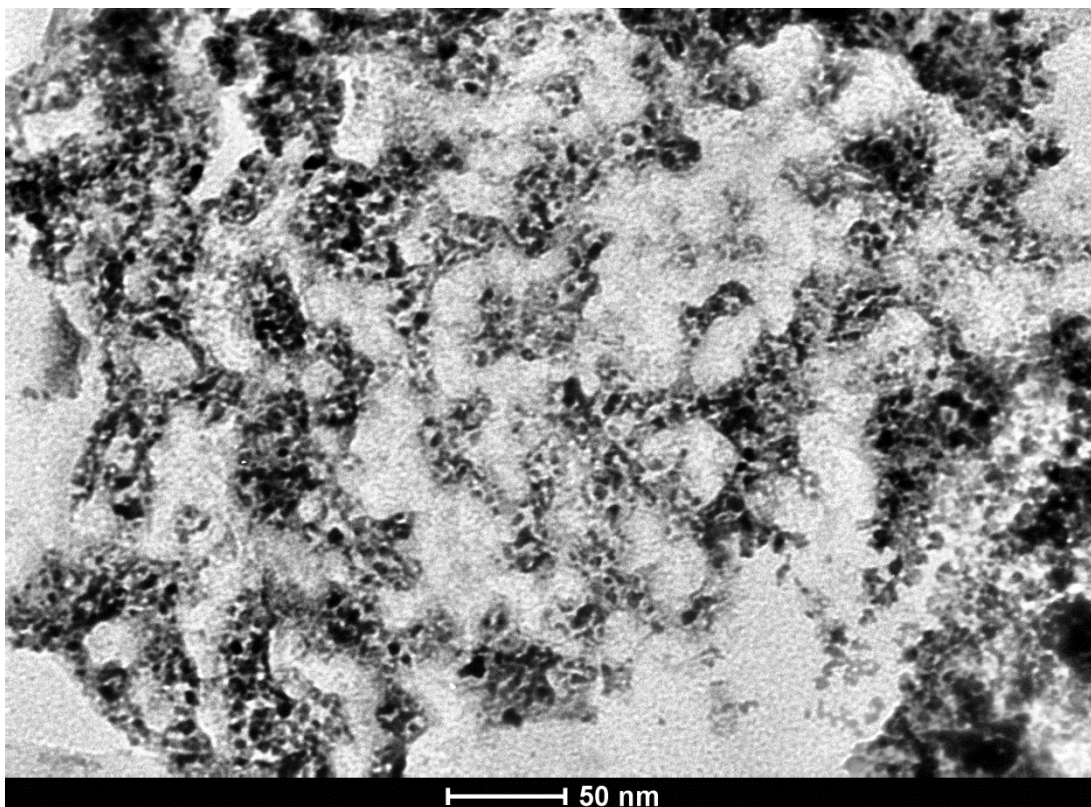Figure 3.11.d. TEM image of Pt / 5 h TU treated GO

Figure 3.11.e. TEM image of Pt / 24 h TU treated GO

It is seen that Pt / GO nanocatalysts has relatively less uniform particles, less dense distribution areas and agglomeration. The images of Pt / 20 min TU treated nanocatalysts display approximately the same sized monodispersed particles which confirms the positive effect of the functional groups on the formation of narrow distributed Pt nanoparticles on the surface of supporting material. On the other hand, the images of Pt / 2 h TU treated GO exhibit relatively larger, irregularly shaped particles and agglomeration which cause a decrease in the activity. In spite of some agglomerated areas, more dense distribution areas and relatively smaller, well-dispersed, more uniform particles are displayed in the images of 5 h TU treated GO in consistence with high activity. TEM images of 24 h TU treated GO displays relatively larger particles and agglomerated areas whereas relatively uniform and well-dispersed particles consistent with its average activity are observed. Also, different morphologies such as spherical, cubic, octahedral and rod shaped particles were observed in the TEM images.

The average particle sizes of the prepared nanocatalysts were calculated via imageJ software by counting of at least 5000 particles of each sample (Table 3.6). The

particle sizes of nanocatalyts are closely labelled in Figure 3.12 also. The particle size distributions are displayed in Figure 3.13.

Table 3.6. Average sizes of nanocatalysts calculated from TEM

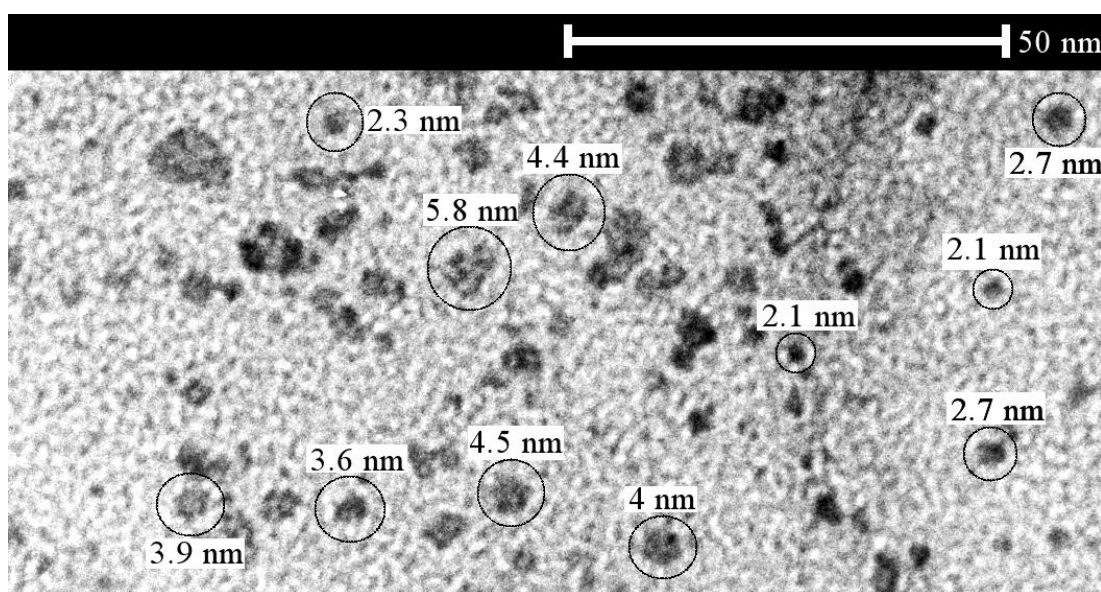| Type of Nanocatalyst	Mean of Particle Sizes Calculated from TEM
Pt / GO	3.90 nm
Pt / 20 min. TU treated GO	3.30 nm
Pt / 2 h. TU treated GO	4.14 nm
Pt / 5 h. TU treated GO	3.51 nm
Pt / 24 h. TU treated GO	4.33 nm

Figure 3.12.a. Labelled Pt / GO particles
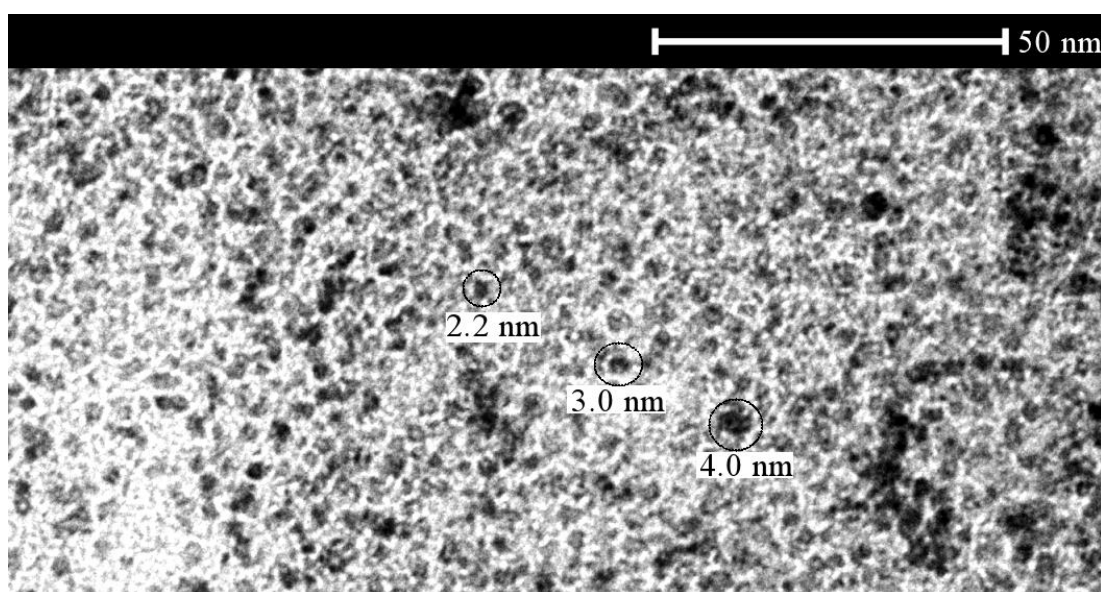
Figure 3.12.b. Labelled Pt / 20 min TU treated GO particles

85
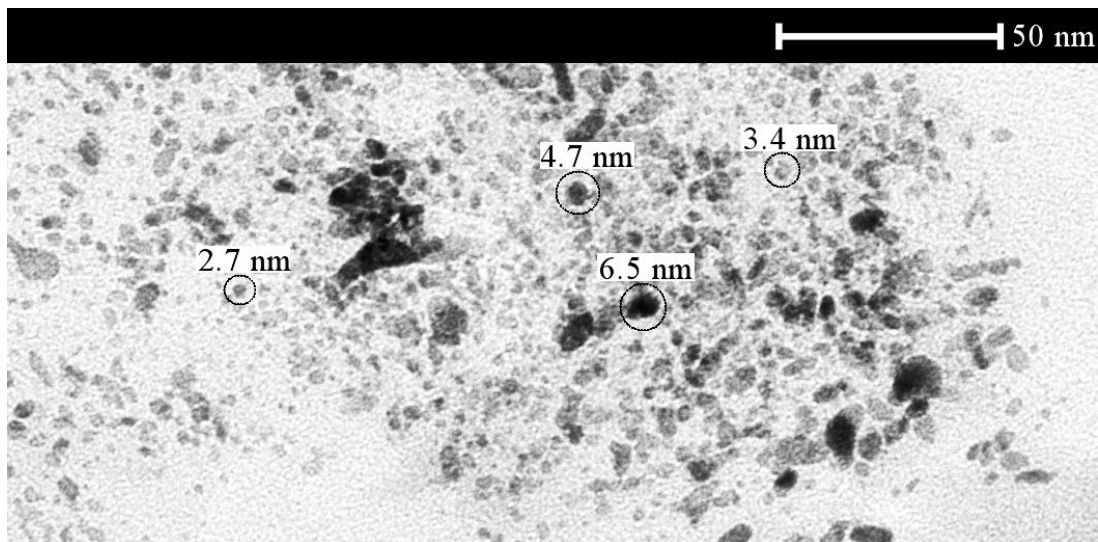
Figure 3.12.c. Labelled Pt / 2 h TU treated GO particles
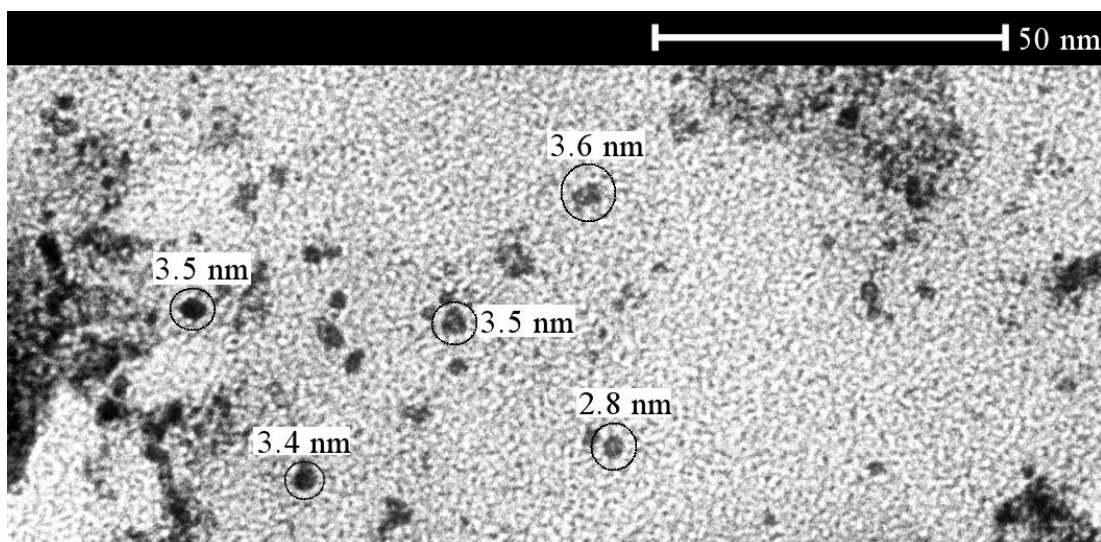
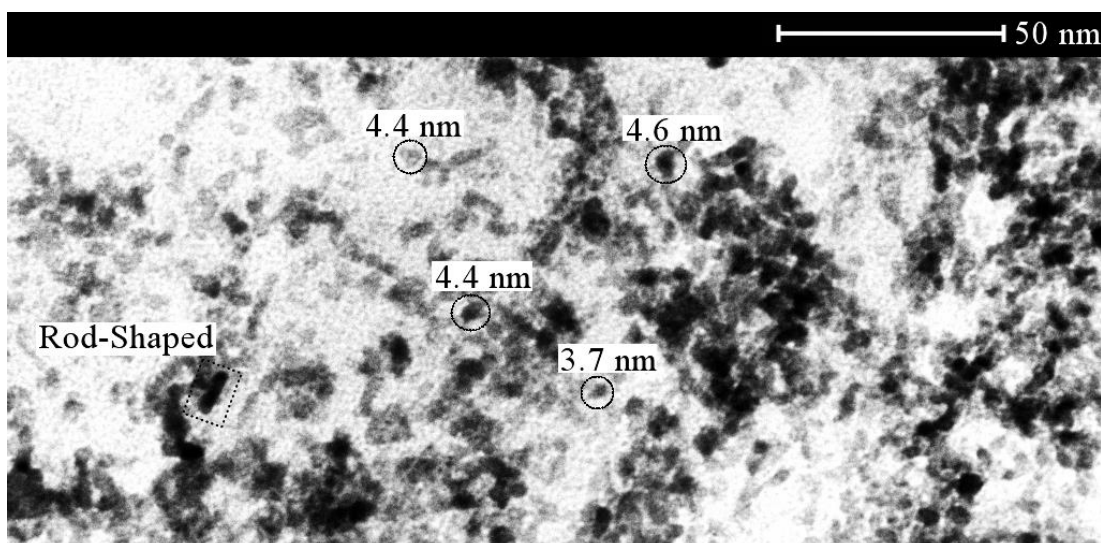Figure 3.12.d. Labelled Pt / 5 h TU treated GO particles

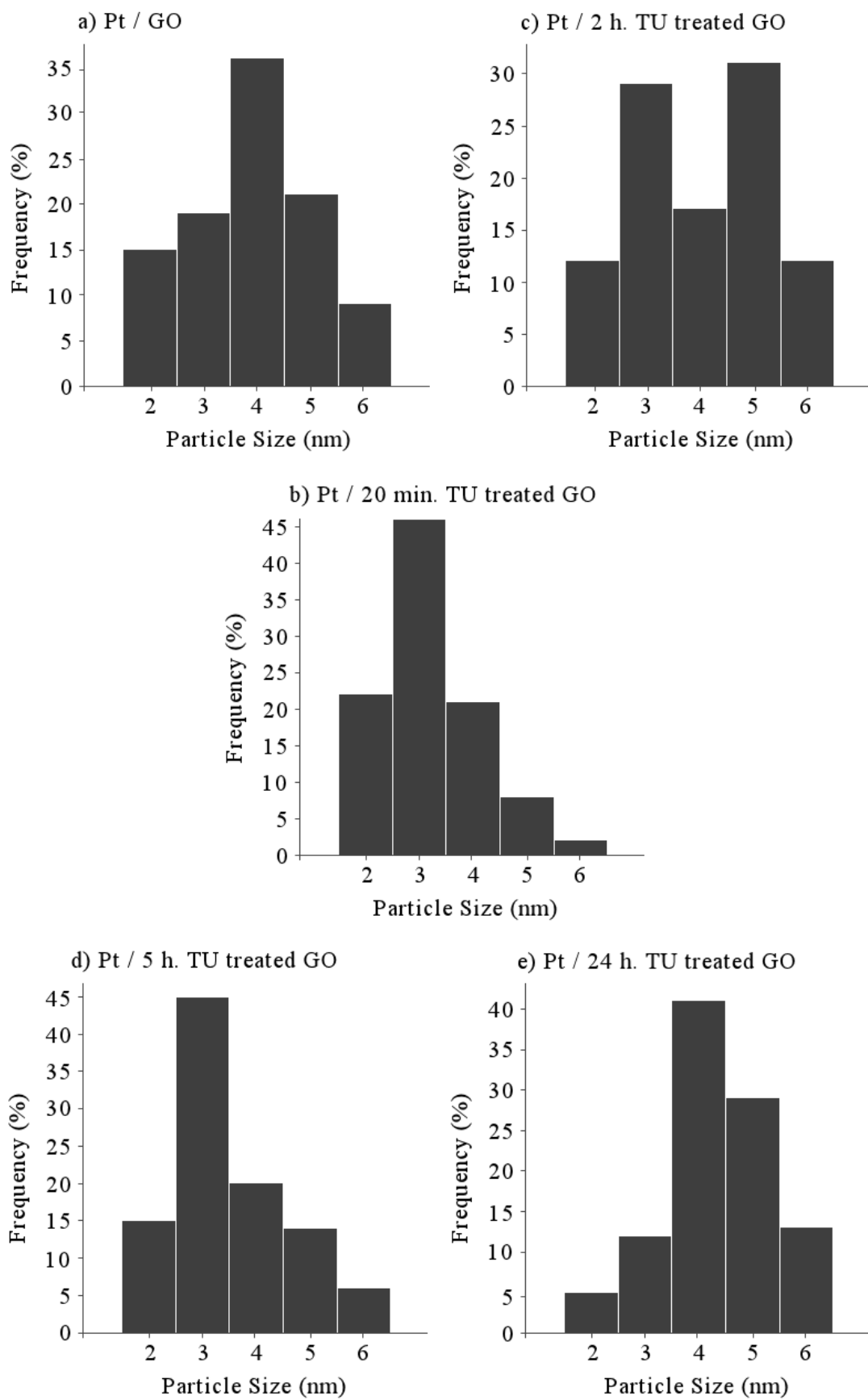Figure 3.12.e. Labelled Pt / 24 h TU treated GO particles

Figure 3.13. TEM histogram of particle size distribution

In comparison the average sizes obtained from XRD and TEM images, it is seen that the mean values exhibited by TEM images are smaller than that are obtained from XRD analyses. However, TEM and XRD results indicated the same order in the sizes of nanocatalysts.

In TEM images, different morphologies were observed also. Cubic structures observed clearly are seen in Figure 3.14.
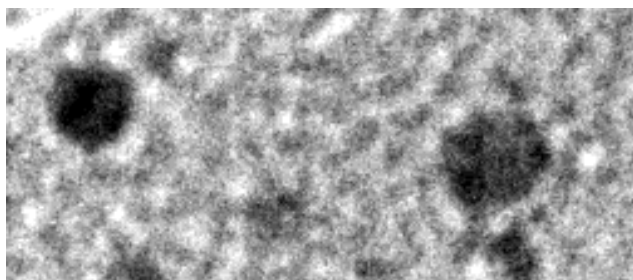

Figure 3.14. Examples of observed cubic particles

In Figure 3.15, simulated images of the growth of cubic particles are seen. Some of the nanoparticles exhibit these intermediate forms were also observed in the TEM images of prepared nanocatalysts.
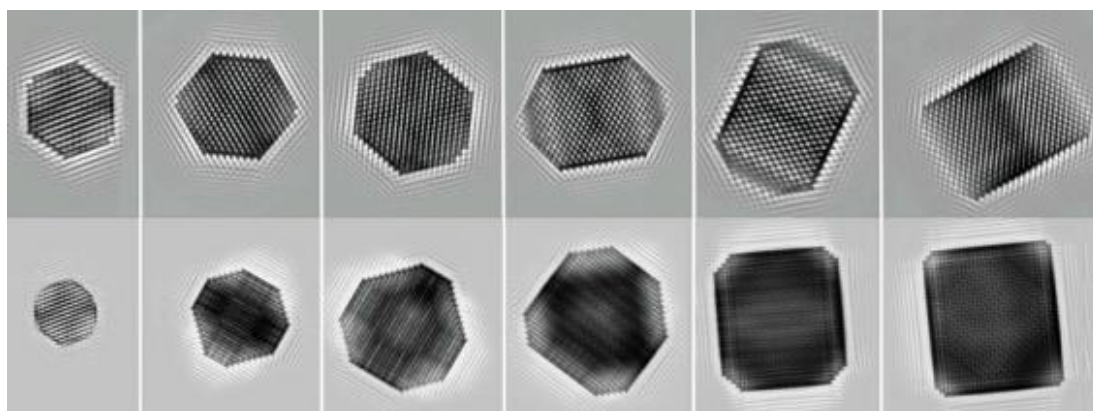

Figure 3.15. Simulated sequential images of the growth of the Pt nanocube [96]

3.8 Characterization by XPS

The electron bonding energies allow the identification of the atoms present on the surface. These energies also provide information on the chemical environment of the atom through chemical shifts. The binding energy increases with the state of oxidation, and in the same state of oxidation, it increases with the electronegativity of the neighboring atoms. When the oxidation state of the element increases, the

electronic density decreases and thus causes a displacement towards the higher binding energies. The study of these displacements makes it possible to determine the degree of oxidation of the element and consequently its chemical nature. An XPS spectrum is the plot of the number of photoelectrons emitted as a function of their binding energy.

All the prepared nanocatalysts were analysed via XPS and the spectral decompositions of the experimental photopics are carried out using the Origin Pro 8.5 software. In general, binding energies of C 1s, O 1s, Pt 4f, S 2p and N 1s (Table 3.7) are varies between 284-290, 530-535, 71-75, 161-165 and 398-402 eV respectively [97] as labelled on the general spectrum in Figure 3.16.

Table 3.7. Electron binding energies of analyzed elements

Region	Binding Energies (eV)
C 1s	284 – 290
O 1s	530 – 535
Pt 4f	71 – 75
S 2p	161 – 165
N 1s	398 – 402

In general spectrum, it is seen Pt / 2 h TU treated GO has the highest platinum ratio on its surface in consistence with its relatively larger particle size. It is also seen that Pt / GO has the lowest platinum ratio on its surface in consistence with its lowest activity. These ratios are also compatible with the amounts determined by ICP-MS analysis.

General spectrum displays relatively higher oxygen ratios of TU treated GO supported naocatalysts than Pt / GO; whereas, relatively reduced carbon ratios are observed. This result is consisted with the Raman spectrum of supporting materials indicating the reduction of the size of the sp^2 domains for TU treated materials. An increased O/C ratio compared to that of GO may suggest a decrease in the average size of the sp^2 domains upon reduction of the GO, and can be explained if new graphitic domains were created that are smaller in size to the ones present in GO before reduction, but more numerous in number. Decreased G band in the Raman spectrum of TU treated GOs is compatible with decrease carbon ratios observed in XPS spectrums.
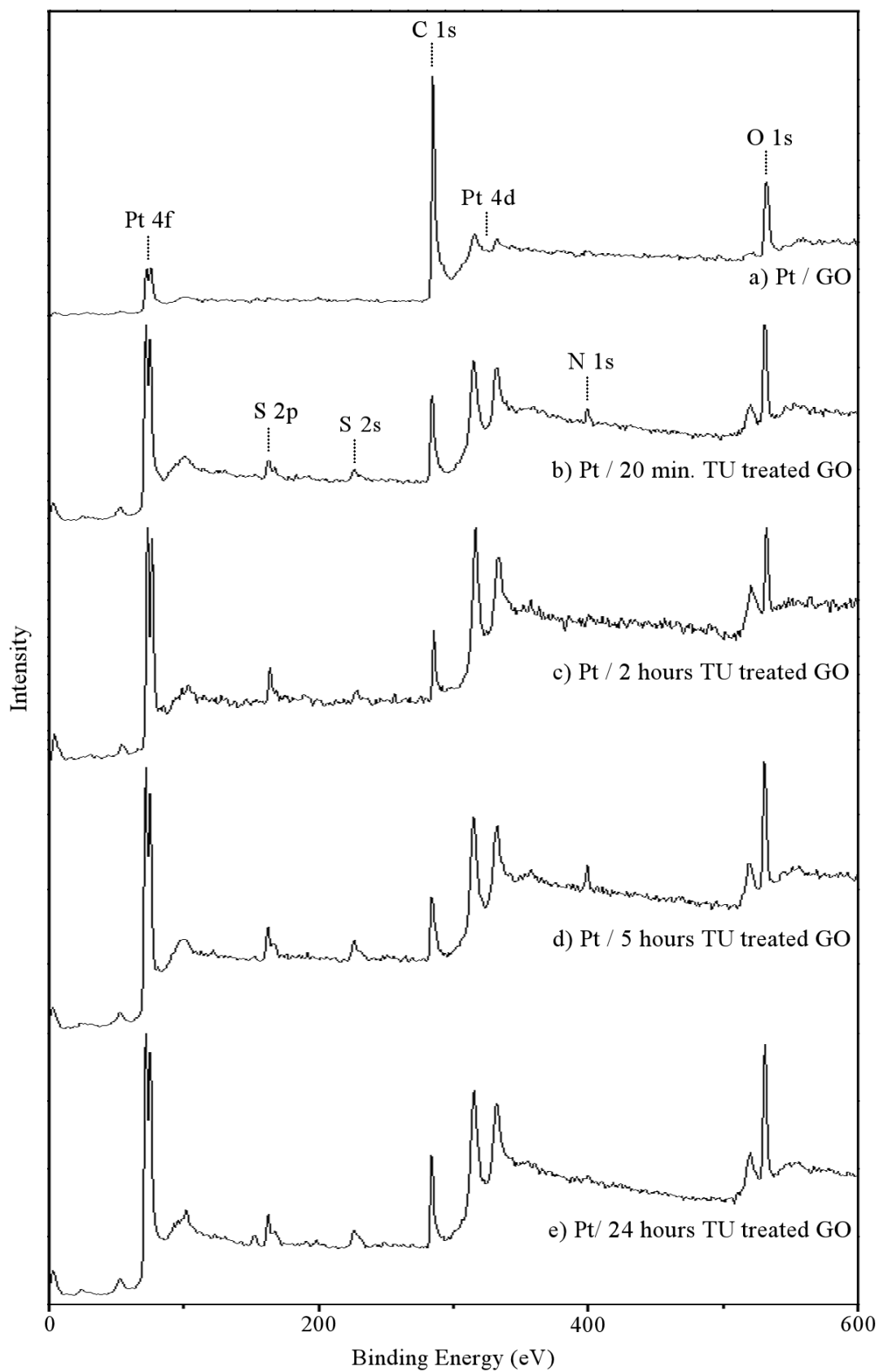
Figure 3.16. XPS spectrum of prepared nanocatalysts

In C 1s spectrum, binding energies of common chemical states (Table 3.8) are theoretically ~286 eV, ~287 eV, ~288 eV for C-O / C-N / C-S, C=O / C=N / C=S , O-C=O respectively [97]. For graphite and graphene, binding energies of common chemical states are ~284 eV and 284.8 eV for sp^2 carbon and sp^3 carbon respectively.

Table 3.8. Electron binding energies of common chemical states of carbon

Chemical States	Binding Energies (eV)
sp^2	~284
C-O / C-N /C-S	~286
C=O / C=N / C=S	~287
O-C=O	~288

The C 1s spectrum of a sample with high concentration of sp^2 carbon has a broad, asymmetric tail towards higher binding energy. C 1s spectrum of nanocatalysts (Figure 3.17) indicates the existence of C-O, C=O and O-C=O states. Higher sp^2 contributions are considered as causing better conductivity. As another state, $\pi-\pi^*$ (HOMO–LUMO) transitions are characteristic satellite peaks in aromatic compounds arise from the excitation of the rings by photoelectrons. The π bond is characteristic for sp^2 hybridization, and the conductivity of sp^2 carbon arises from π-conjugate delocalized electrons.
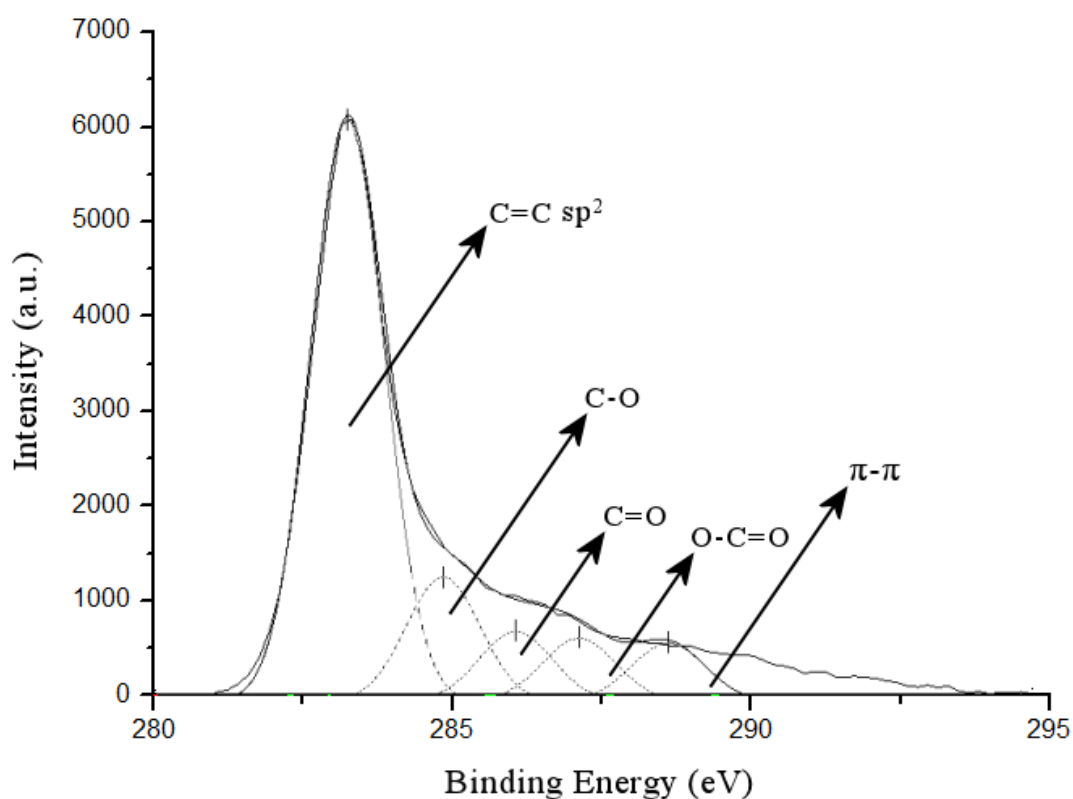

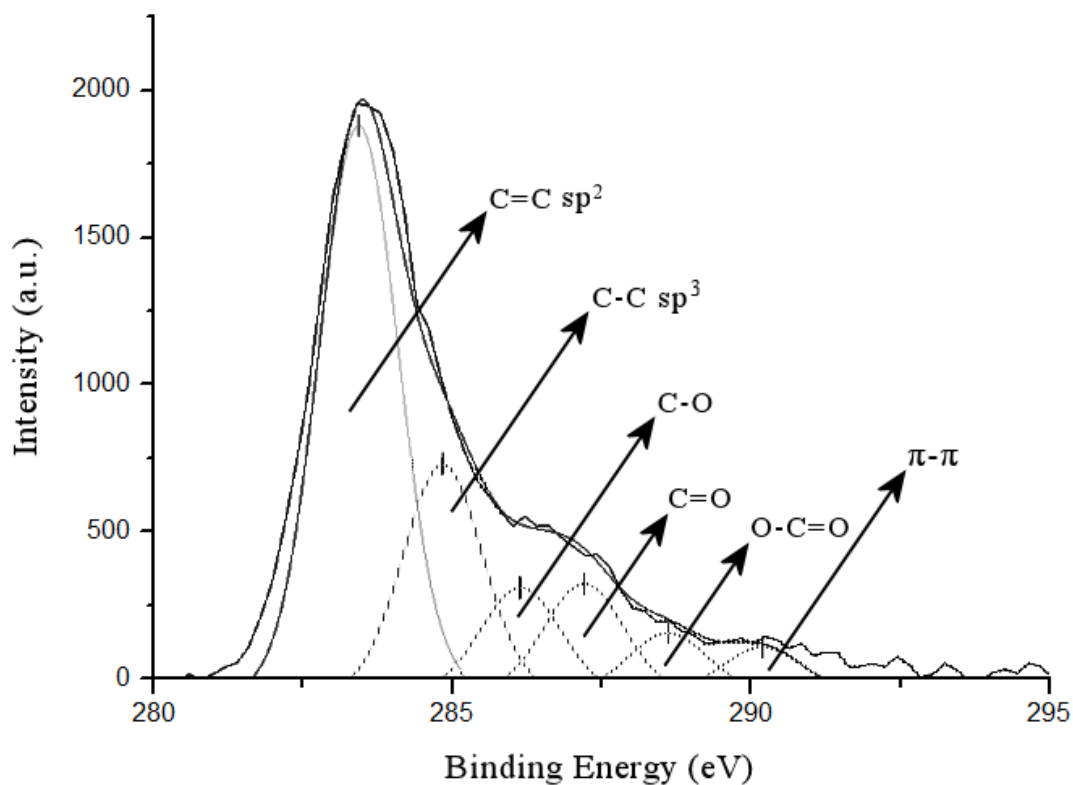Figure 3.17.a. C 1s electron spectra of Pt / GO

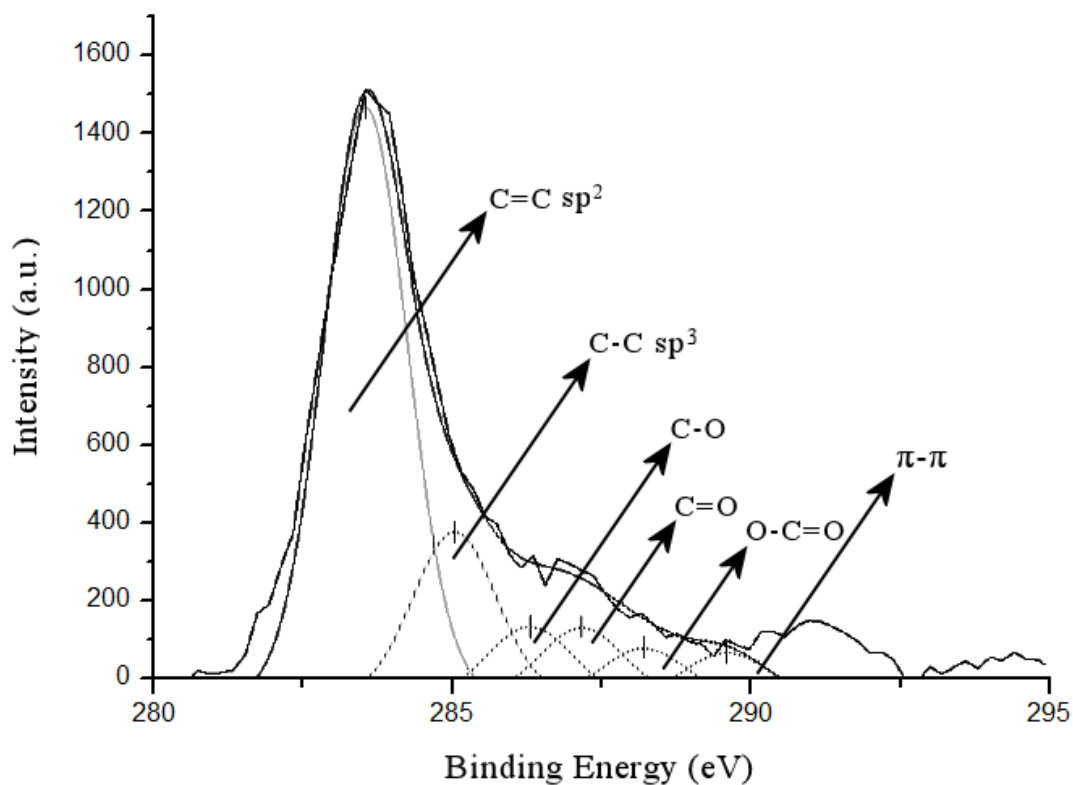Figure 3.17.b. C 1s electron spectra of Pt / 20 min. TU treated GO

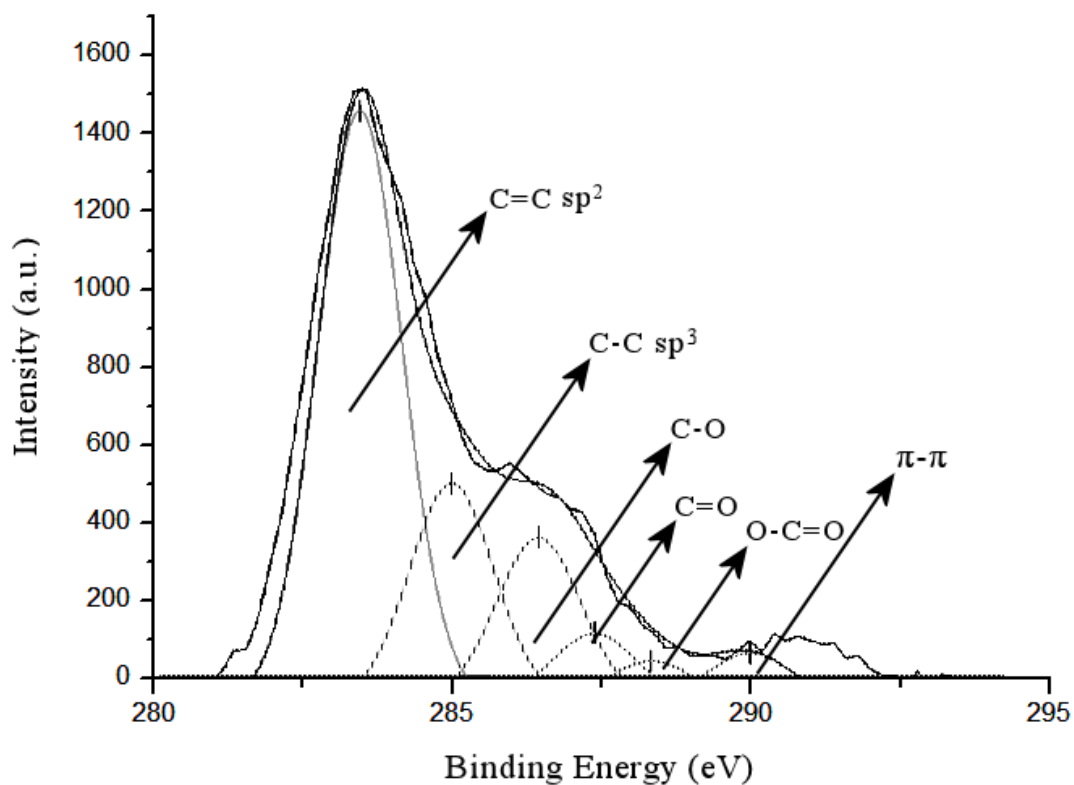Figure 3.17.c. C 1s electron spectra of Pt / 2 h TU treated GO

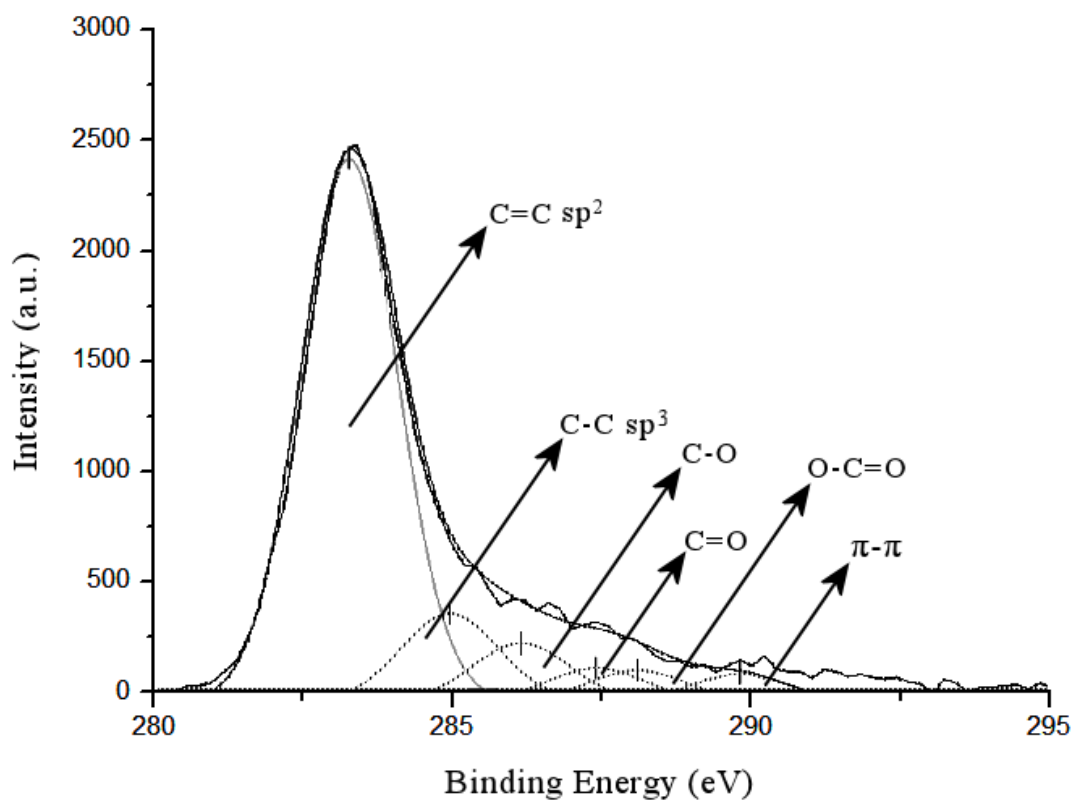Figure 3.17.d. C 1s electron spectra of Pt / 5 h TU treated GO

Figure 3.17.e. C 1s electron spectra of Pt / 24 h TU treated GO

In O 1s spectrum, binding energies of common chemical states (Table 3.9) are theoretically ~531 eV, ~533 eV, ~534 eV for C-O, C=O, O-C=O respectively [97]. Also the binding energy of metal oxide (i.e. platinum oxide) is theoretically ~529 as that is observed in the spectrum of Pt / 5 h TU treated GO.

Table 3.9. Electron binding energies of common chemical states of oxygen

Chemical States	Binding Energies (eV)
C-O	~531
C=O	~533
O-C=O	~534

O 1s spectrum of prepared nanocatalysts (Figure 3.18) displays the dramatically decreased amount of carboxyl group in TU treated GOs compared with GO, which indicating the reduction by thiourea. In the spectrum of Pt / 24 h TU treated GO, C-O bonds become largely prominent while the other oxygen groups have decreased to minimum amounts. Also it is seen that C=O groups are prominent for Pt / 20 min TU treated GO besides C-O groups in high ratio. Platinum oxide and C-O bonds can be seen as prominent for Pt / 5 h TU treated GO.
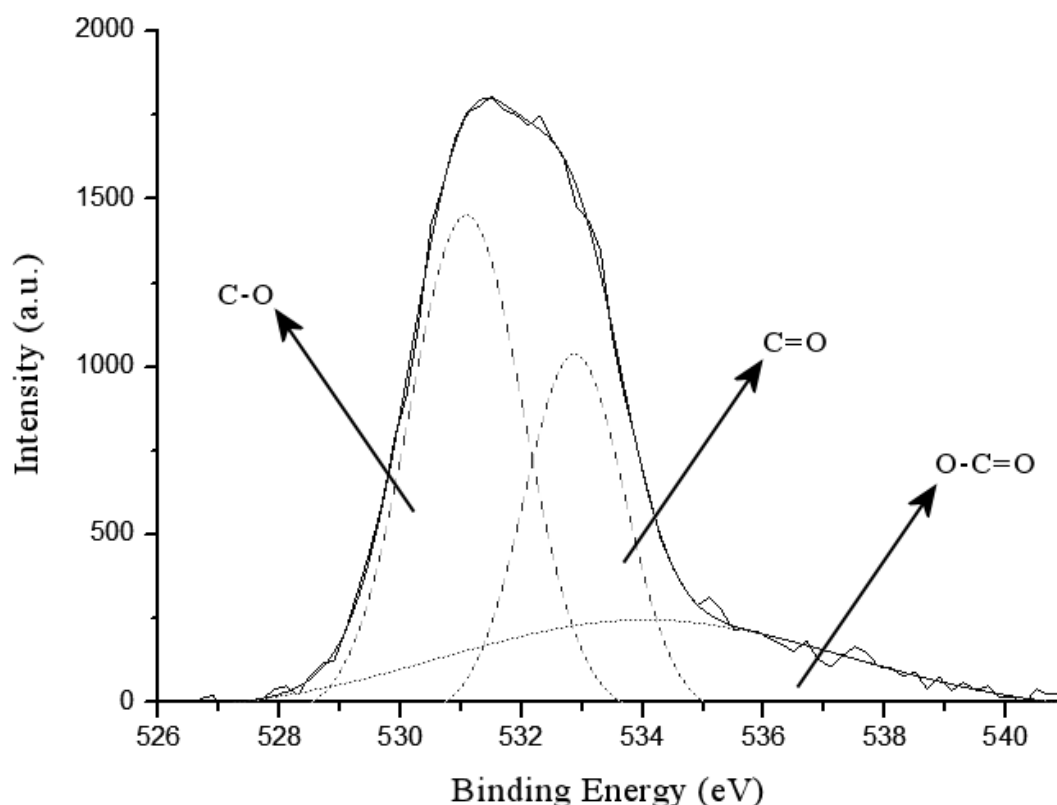

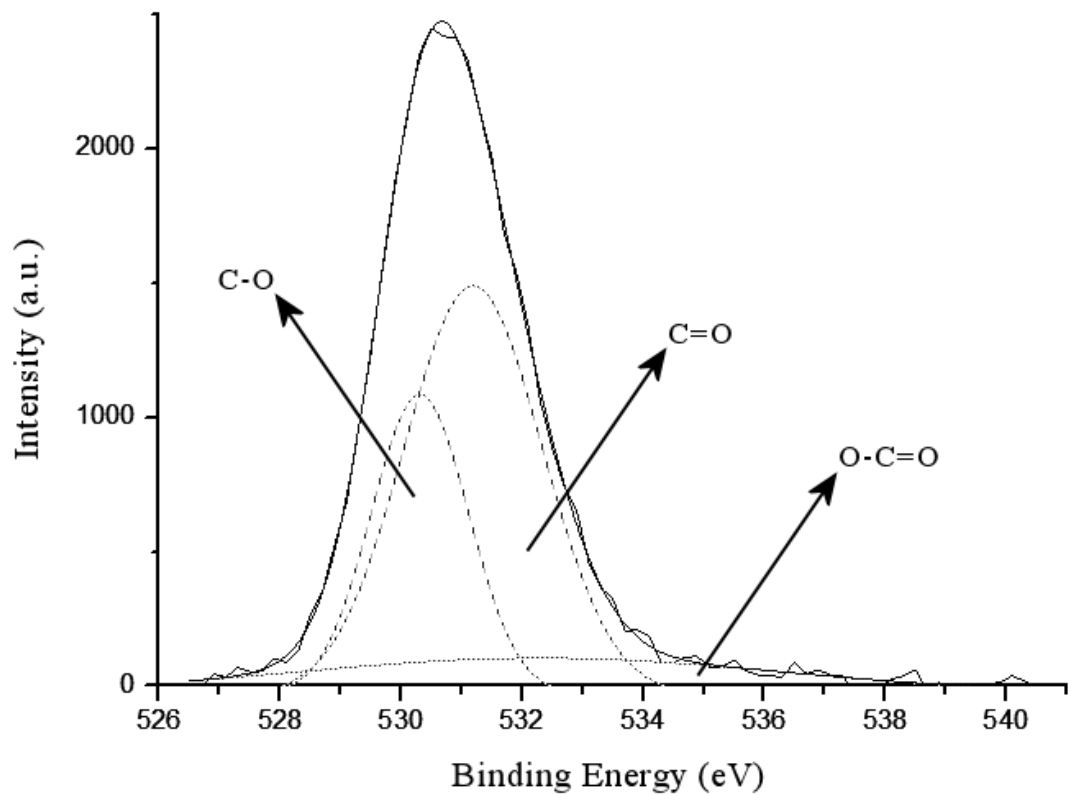Figure 3.18.a. O 1s electron spectra of Pt / GO

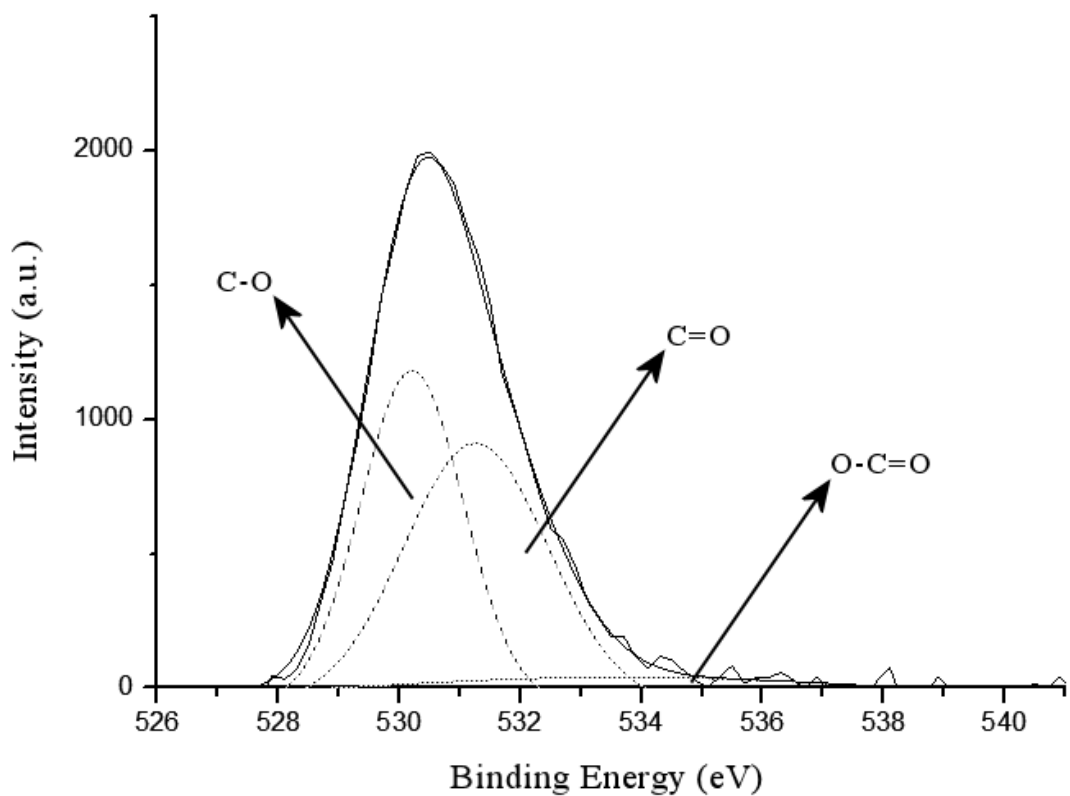Figure 3.18.b. O 1s electron spectra of Pt / 20 min TU treated GO

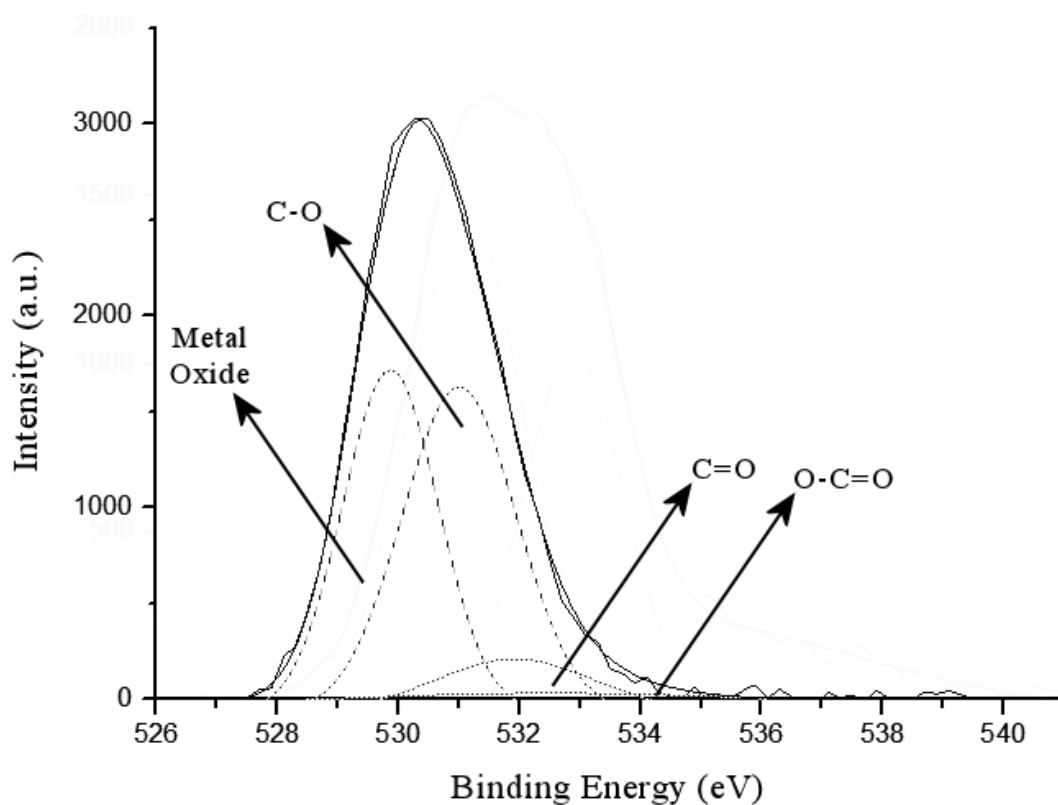Figure 3.18.c. O 1s electron spectra of Pt / 2 h TU treated GO

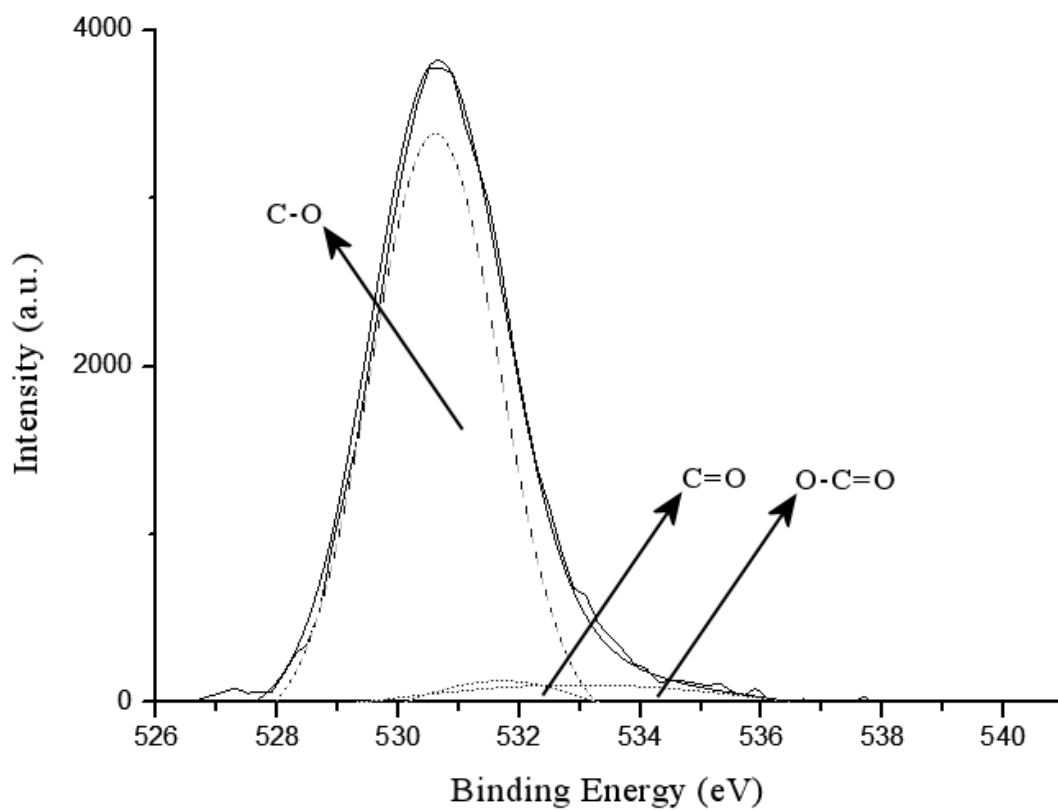Figure 3.18.d. O 1s electron spectra of Pt / 5h TU treated GO

Figure 3.18.e. O 1s electron spectra of Pt / 24 h.

In the spectrum of S 2p, binding energies of common chemical states (Table 3.10) are theoretically ~162.5 eV, ~165.5 eV, ~168.0 eV for C-S, C=S, S-O respectively [97]. The largest peaks of the S-C bonds indicate thiol groups on the graphene carbon lattice. The S=C peak may arise from presence of unhydrolyzed thiourea and it is larger for 20 min, 2 h and 5 h treated GO (Figure 3.19), while the S-O peak may be due to unwanted oxidation of byproducts. In addition, in the spectrum of N 1s, binding energies of common chemical states (Table 3.10) are theoretically ~399 eV, ~401 eV, ~402 eV for C-NH$_2$, C=N, N-O respectively [97]. The presence of thiol groups is indicated by N 1s spectrum of Pt / TU treated GOs (Figure 3.20). The minimum amount of sulphur and nitrogen observed in Pt/GO may be caused from unwanted remainings of starting materials (nitric acid and sulfuric acid) in the preparation procedure of GO.

Table 3.10. Electron binding energies of common chemical states of S and N

Chemical States	Binding Energies	Chemical States	Binding Energies
C-S	~162.5 eV	C-NH$_2$	~399 eV
C=S	~165.5 eV	C=N	~401 eV
S-O	~168.0 eV	N-O	~402 eV

Figure 3.19.a. S 2p electron spectra of Pt / GO

Figure 3.19.b. S 2p electron spectra of Pt / 2O min TU treated GO

Figure 3.19.c. S 2p electron spectra of Pt / 2 h TU treated GO

Figure 3.19.d. S 2p electron spectra of Pt / 5 h TU treated GO

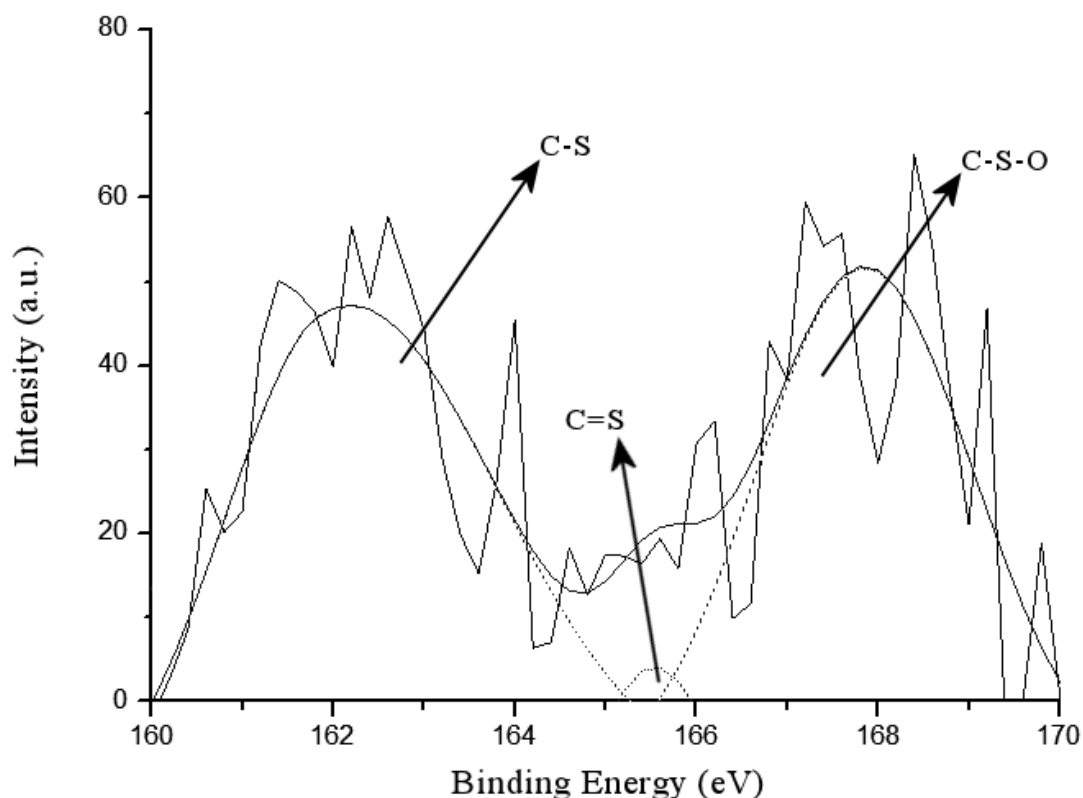Figure 3.19.e. S 2p electron spectra of Pt / 24 h TU treated GO

Figure 3.20.a. N 1s electron spectra of Pt / GO
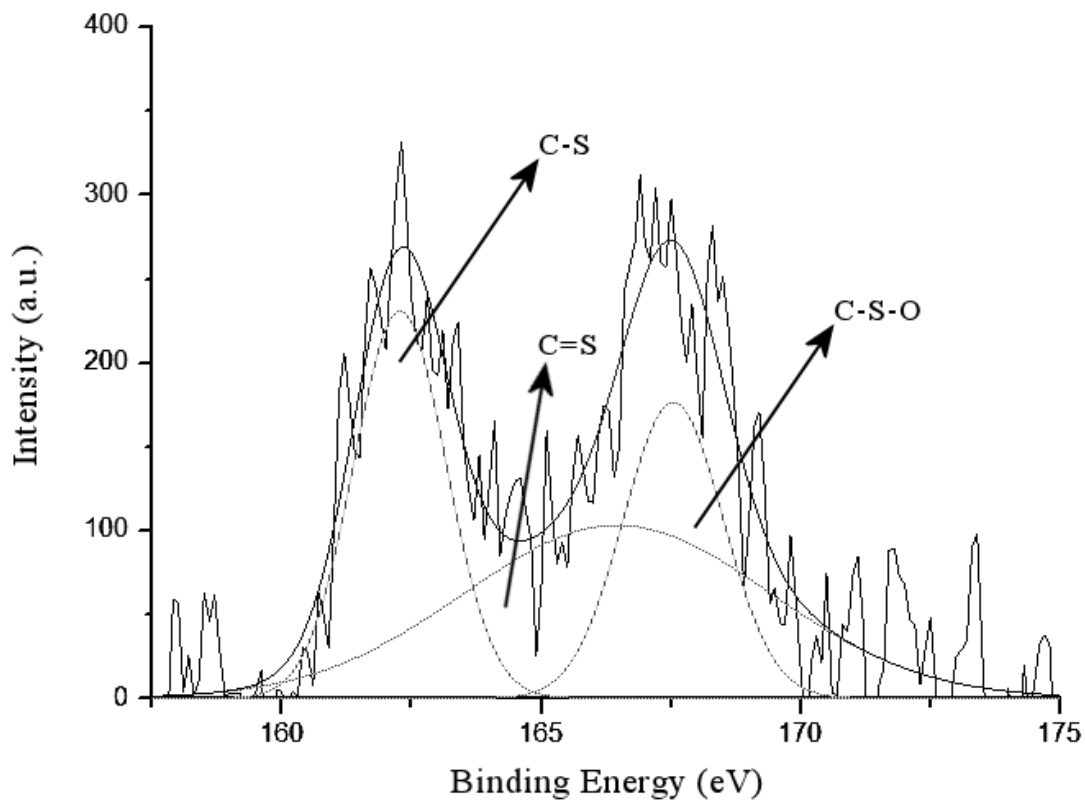

Figure 3.20.b. N 1s electron spectra of Pt / 20 min TU treated GO
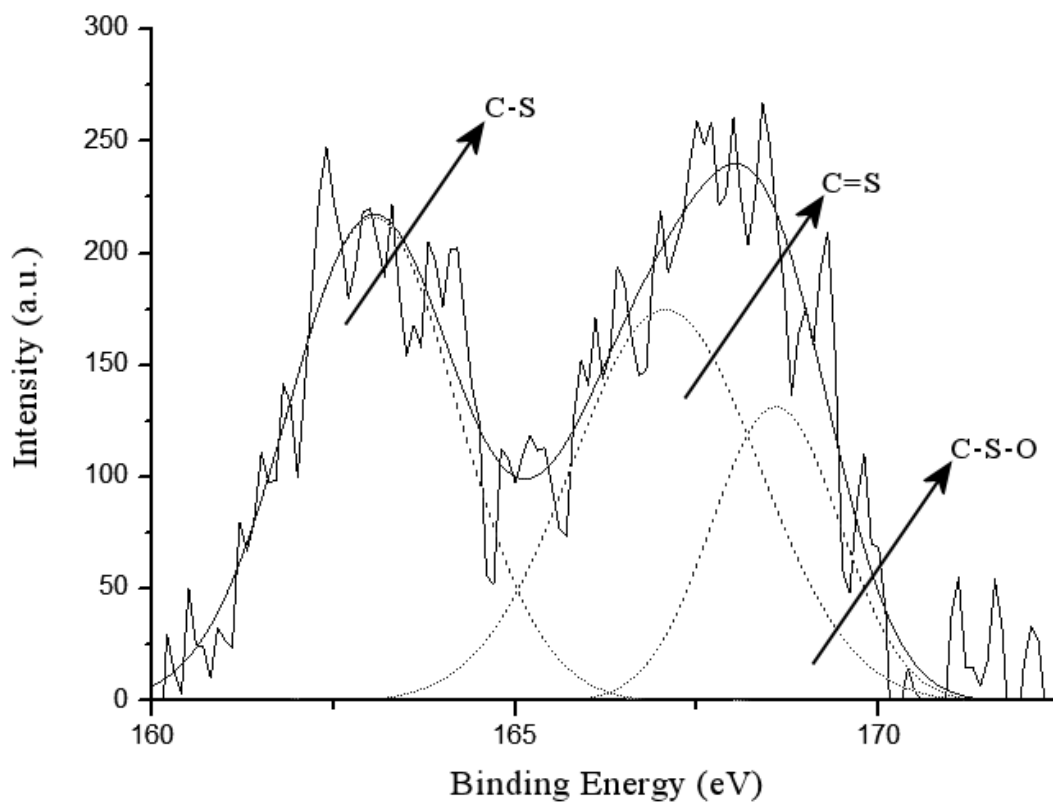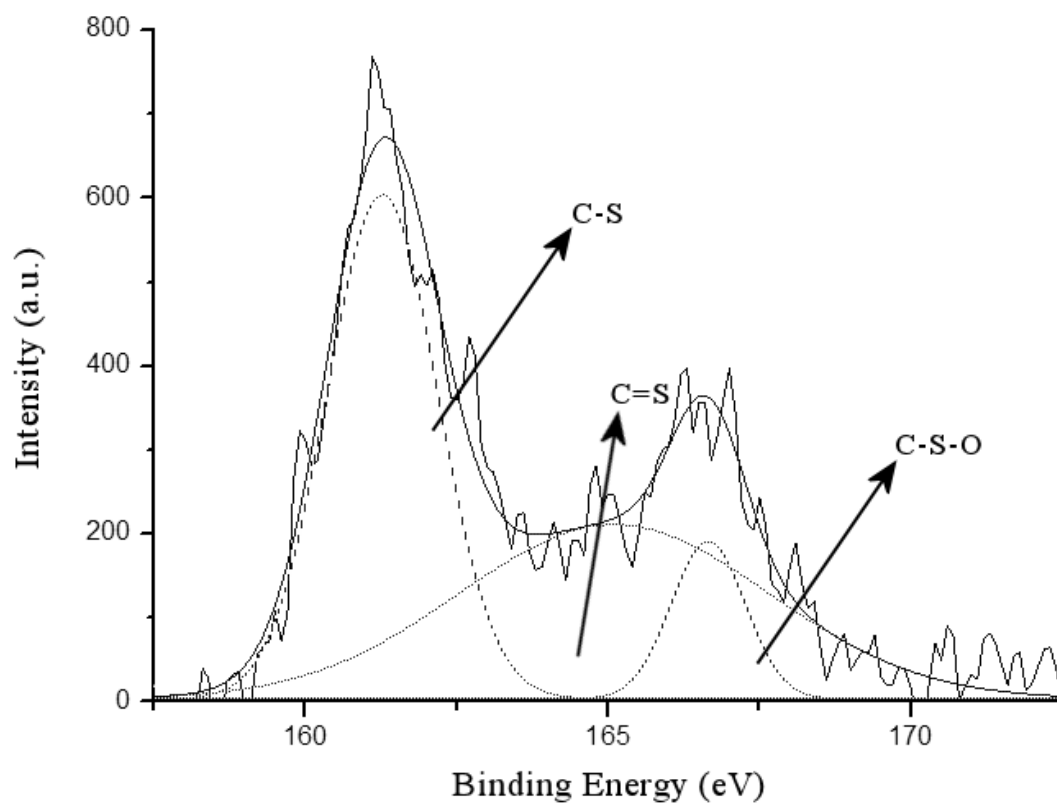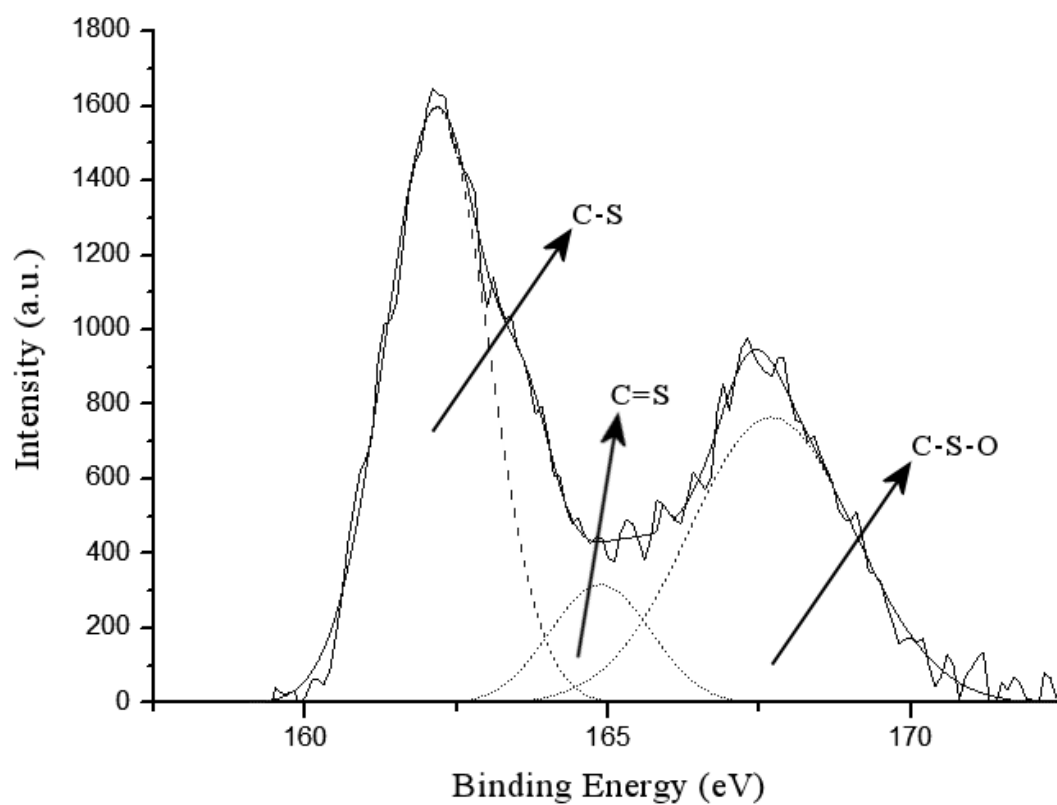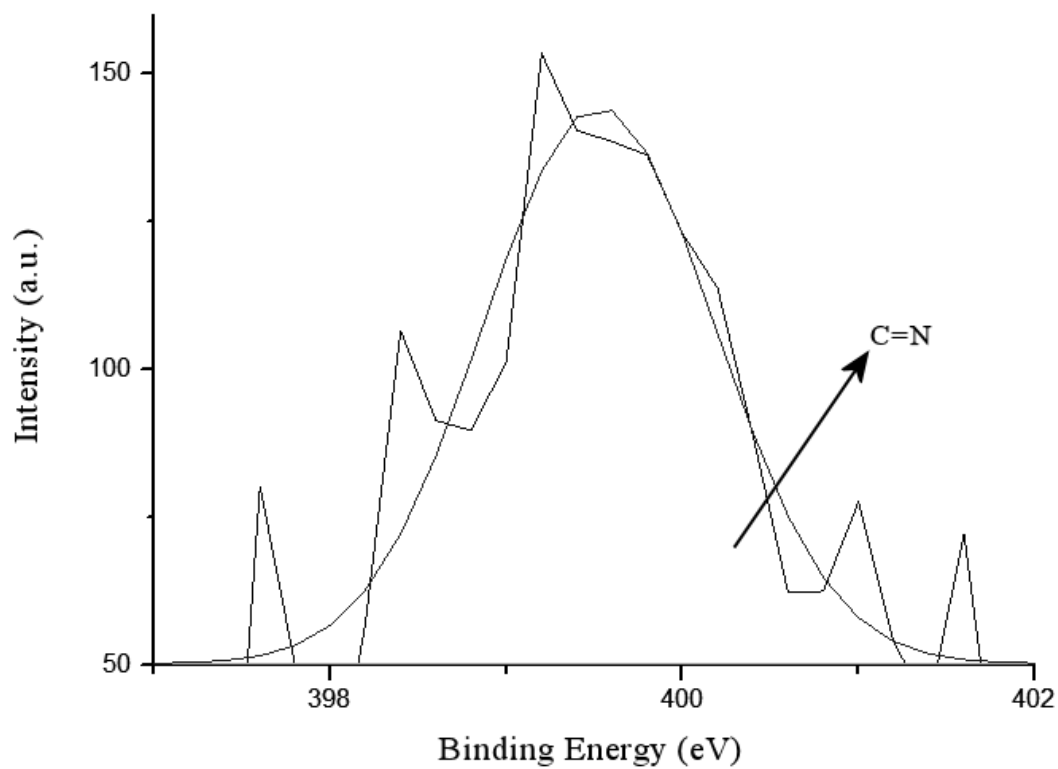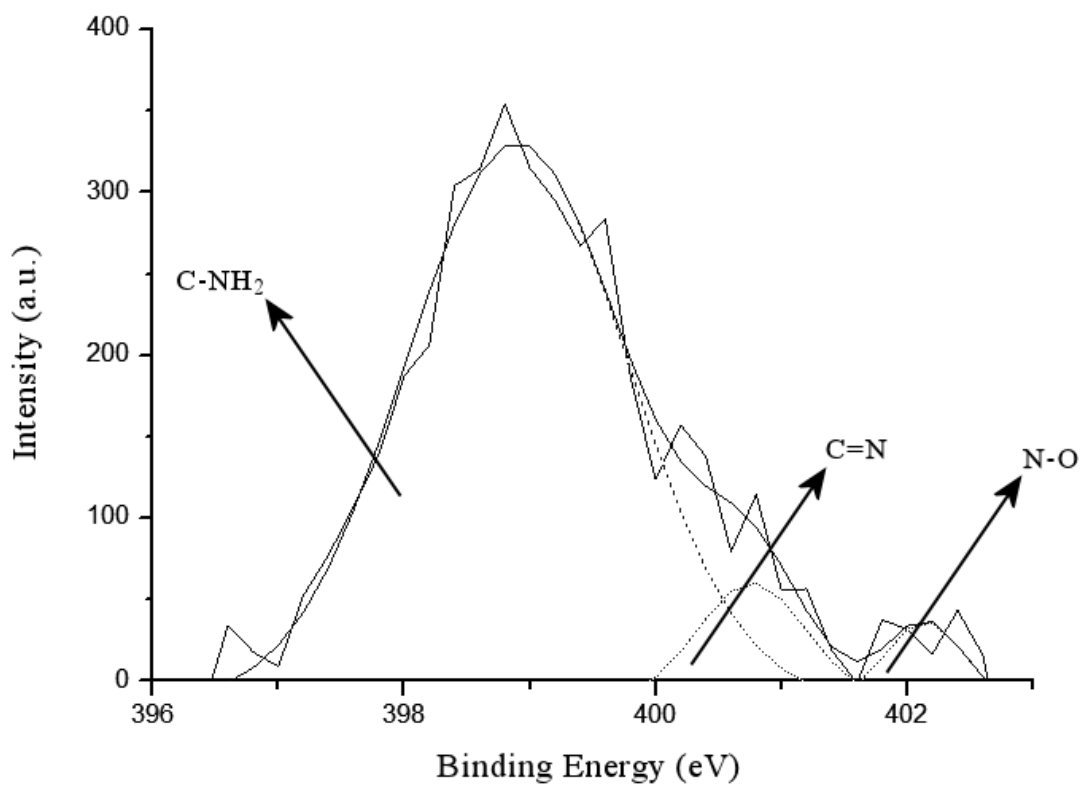
Figure 3.20.c. N 1s electron spectra of Pt / 2 h TU treated GO

Figure 3.20.d. N 1s electron spectra of Pt / 5 h TU treated GO

Figure 3.20.d. N 1s electron spectra of Pt / 24 h TU treated GO

As another analyzed element, Pt 4f region has well separated spin-orbit components having Δ_{metal}=3.35eV [97]. In the XPS spectrum for each of nanocatalyst (Figure 3.21), Pt 4f peaks consisting of pairs of doublet ($4f_{7/2}$ and $4f_{5/2}$) with the spin orbit splitting of 3.3 eV were obtained. The relative intensity of the doublet peaks having equal half widths is 4:3. Binding energies of common chemical states exhibited in doublet peaks (Table 3.11) are ~71.5-74.4 eV, ~72.5-76.1 eV, ~74.9-78.2 eV for Pt (0), Pt (II), Pt (IV) respectively [98].

Table 3.11. Electron binding energies of common chemical states of platinum

Chemical States	Binding Energies (eV)
Pt (0)	~71.1 – 74.4
Pt (II)	~ 72.5 – 76.1
Pt (IV)	~74.9 – 78.2

The ratios of Pt(0), Pt(II) and Pt(IV) was calculated basing on the areas of the fitted peaks (Table 3.12). In order to obtain the ratio of the oxidation states of the platinum nanoparticles by XPS technique, Gaussian-Lorentzian method was used for fitting XPS peaks and the background was subtracted by means of Shirley's method. Calculations were performed by Origin Pro 8.5 software.
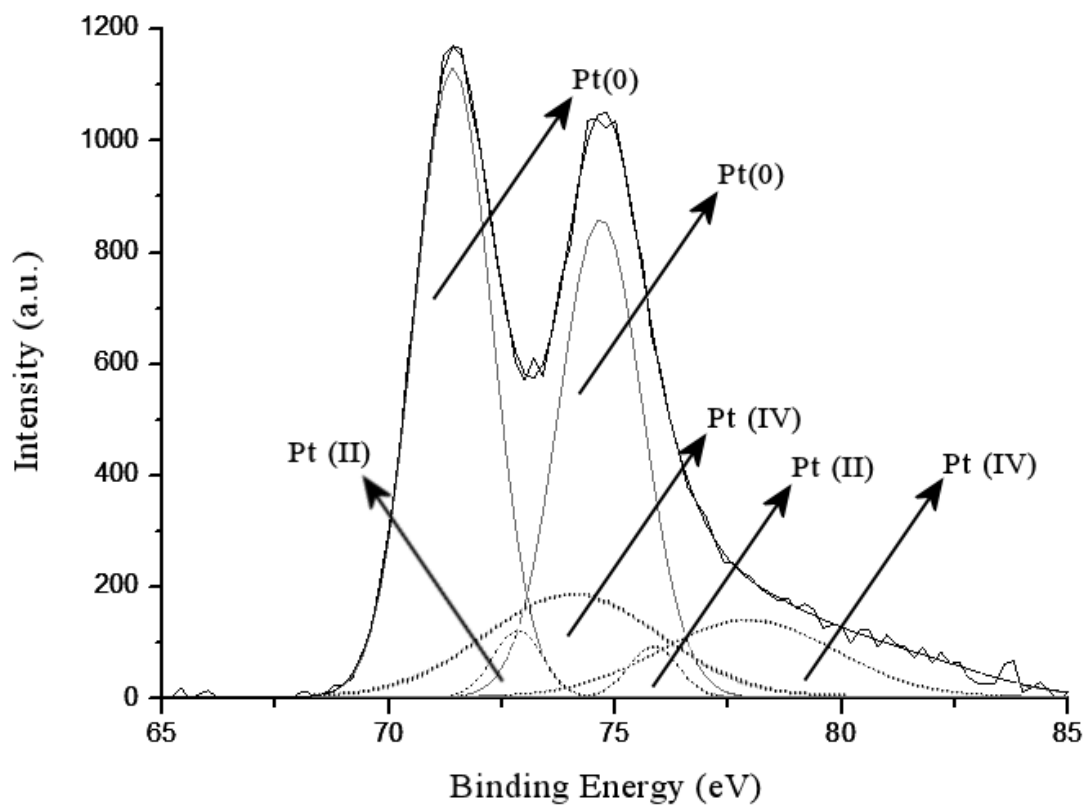
Figure 3.21.a Pt 4f electron spectra of Pt / GO
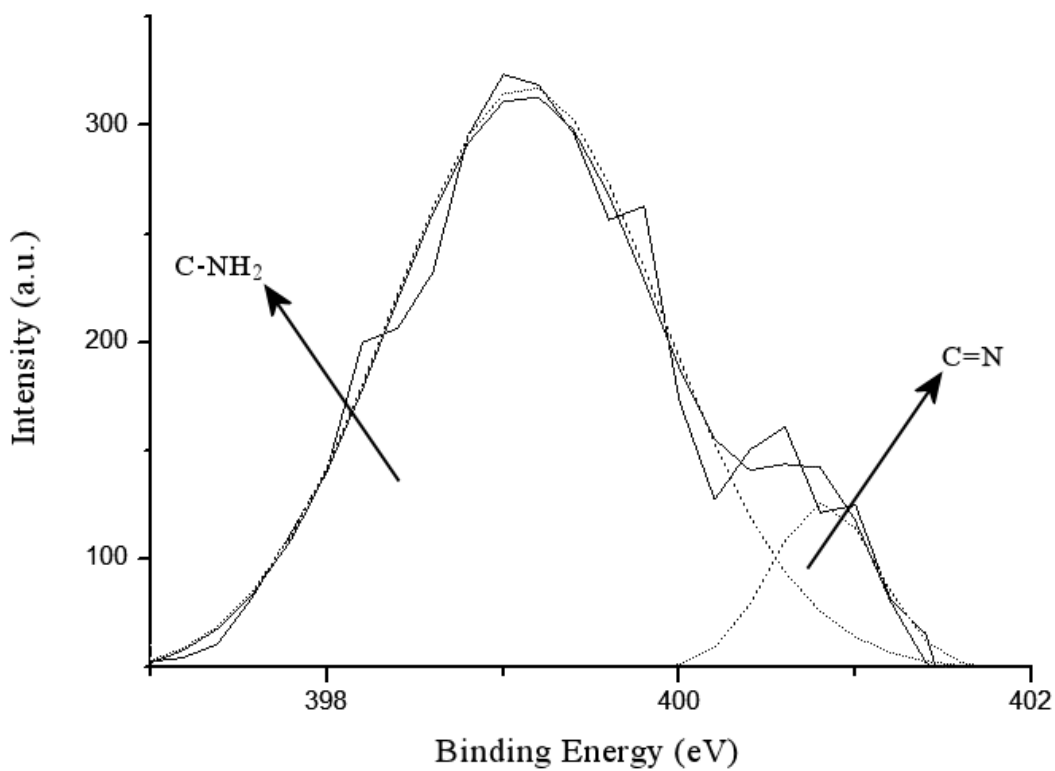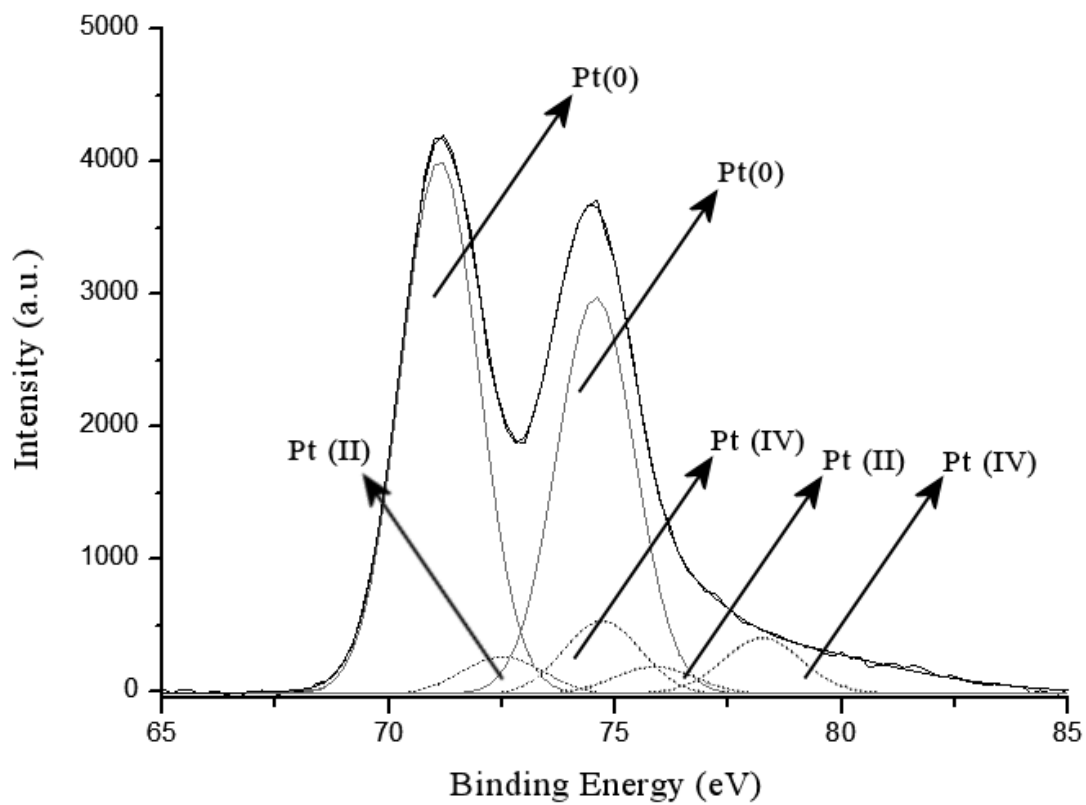

3.21.b. Pt 4f electron spectra of Pt / 20 min TU treated GO
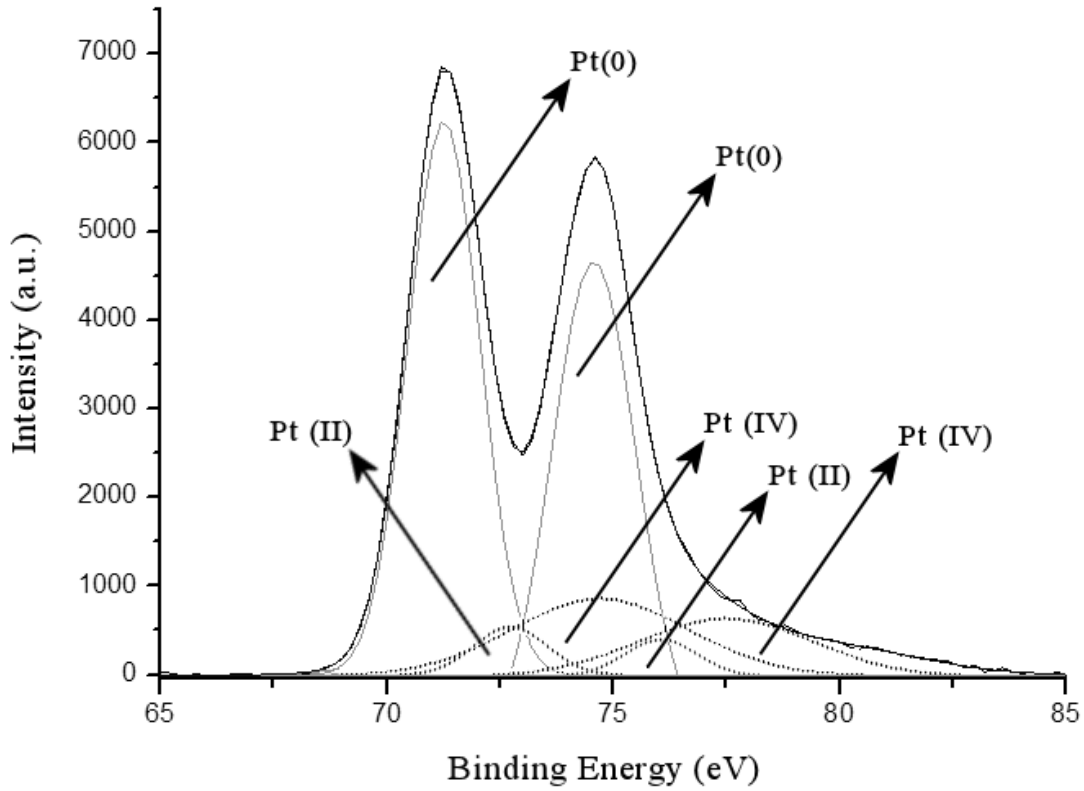
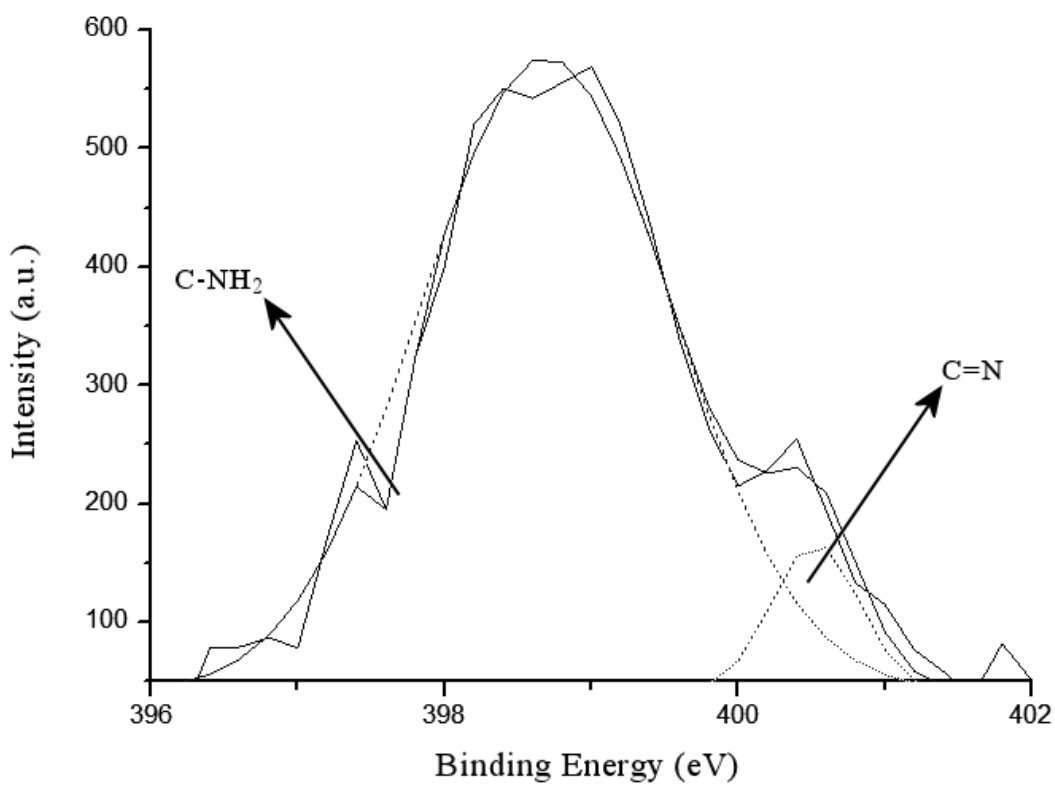Figure 3.21.c. Pt 4f electron spectra of Pt / 2 h TU treated GO

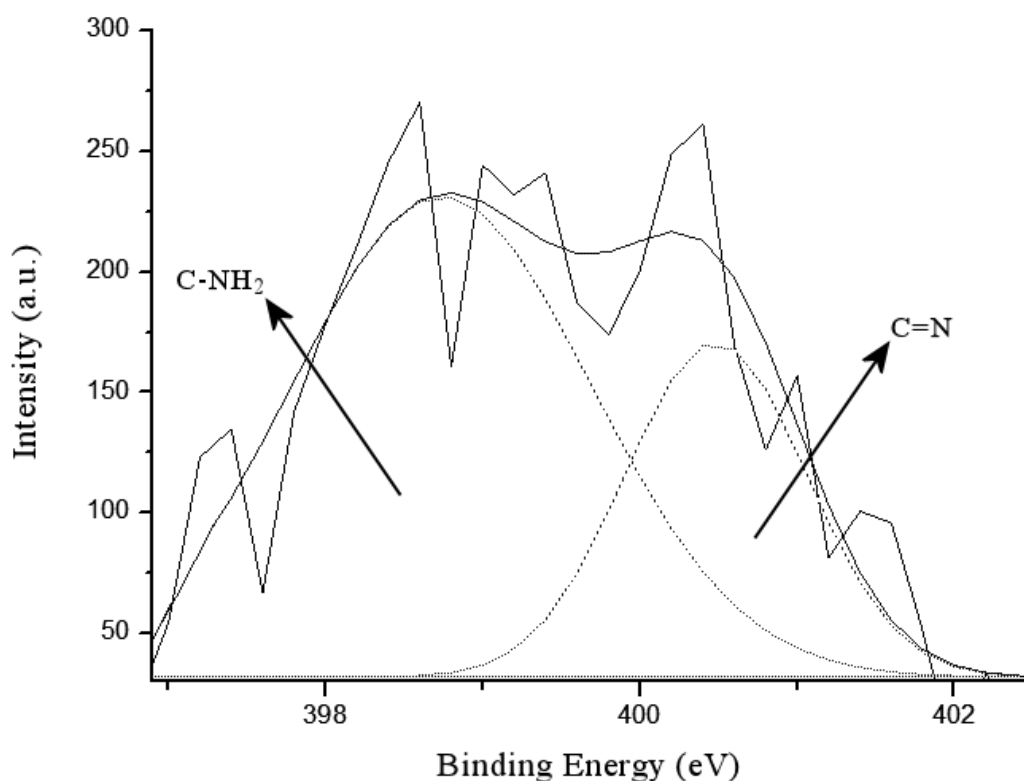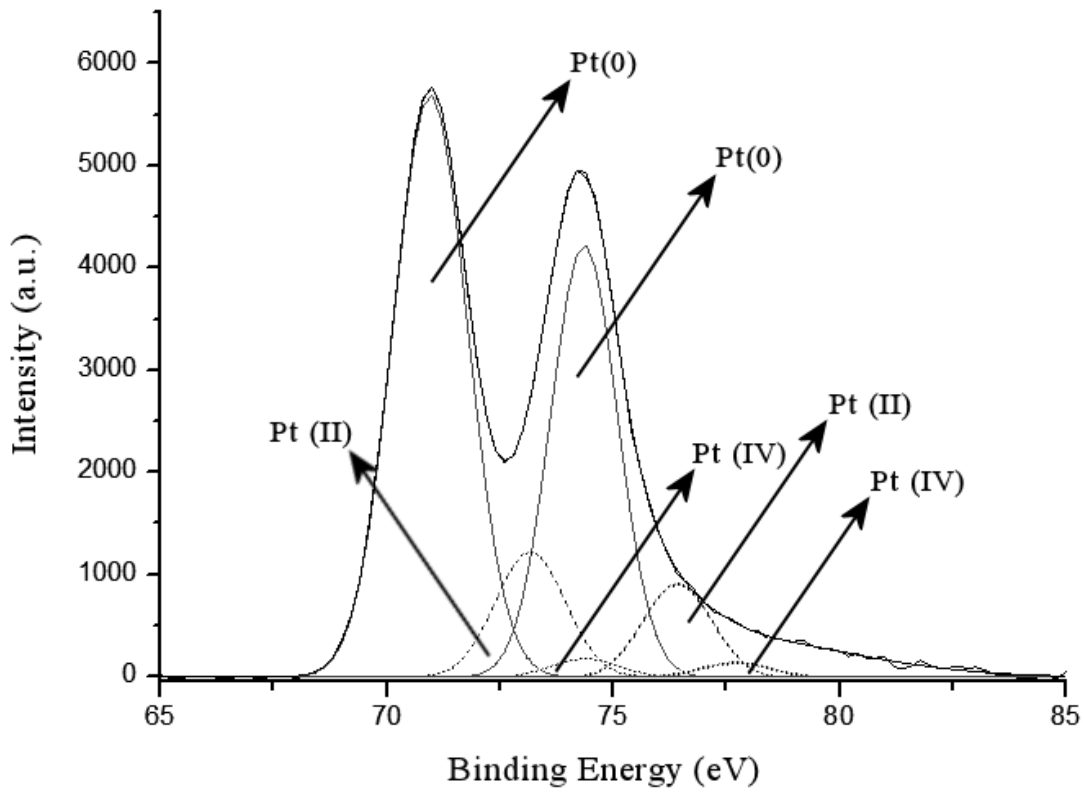Figure 3.21.d. Pt 4f electron spectra of Pt / 5 h TU treated GO
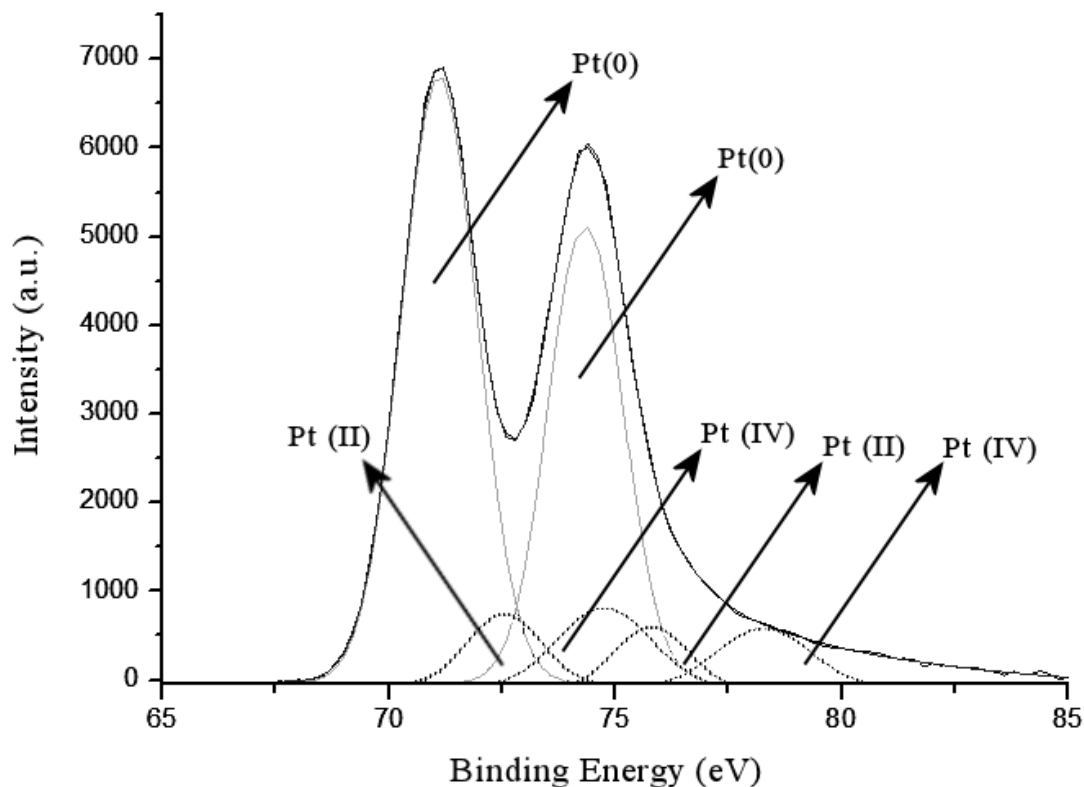
Figure 3.21.e. Pt 4f electron spectra of Pt / 24 h TU treated GO

As a result, the ratios of Pt(0) found above 70% of the prepared nanocatalysts indicate successfully formations of "zero-state" Pt nanoparticals. The relatively lowest Pt(0) ratios were found in Pt/GO and Pt/2h TU treated GO in consistence with their relatively lower activities. Also, relatively the highest Pt (II) ratio was found in Pt/5 h TU treated GO in consistence with its O 1s spectrum.

Table 3.12. The percentages of Pt (0), Pt (II) and Pt (IV) in prepared nanocatalysts

Type of Nanocatalyst	Pt (0)	Pt (II)	Pt (IV)
Pt / GO	70%	6%	24%
Pt / 20 min. TU treated GO	81%	6%	13%
Pt / 2 h. TU treated GO	69%	8%	23%
Pt / 5 h. TU treated GO	78%	17%	5%
Pt / 24 h. TU treated GO	84%	7%	9%

If the percentage platinum amounts determined by ICP-MS technique are proportioned to Pt (0) ratios obtained from XPS spectrum, the overall Pt (0) ratios can be calculated (Table 3.13). For example, if the percentage of platinum is 27% in Pt/GO, the overall percentage of Pt(0) is obtained as 27 x (70/ 100) which is equal to 18.9 %. These Pt(0) ratios of the nanocatalysts are in consistence with their activities.

Table 3.13. The overall Pt (0) ratios proportional to ICP-MS results

Type of Nanocatalyst	Overall Pt (0) Ratio
Pt / GO	18.9 %
Pt / 20 min. TU treated GO	26.7 %
Pt / 2 h. TU treated GO	24.1 %
Pt / 5 h. TU treated GO	26.0 %
Pt / 24 h. TU treated GO	25.2 %

3.9 Cyclic Voltammetry (CV) Studies

Electrochemical properties and activities of all prepared nanocatalysts toward methanol oxidation reaction were examined via the cyclic voltammetry technique. In accordance with their cyclic voltammograms, the electrochemical surface areas (ECSA), Pt utilities and the roughness factor values were calculated for all catalysts.

Hydrogen adsorption and desorption curves exhibited the adsorption and desorption of the hydrogen atoms exist in the electrolyte on the surface of the nanocatalyst (platinum). In order to obtain the hydrogen adsorption (H_{ads}) and desorption (H_{des}) curves in acidic medium, voltage swept from -0.35V to 1.0 V in 0.5 M $HClO_4$. Figure 3.22 displays the cyclic voltammograms of all nanocatalysts in 0.5 M $HClO_4$ at room temperature.
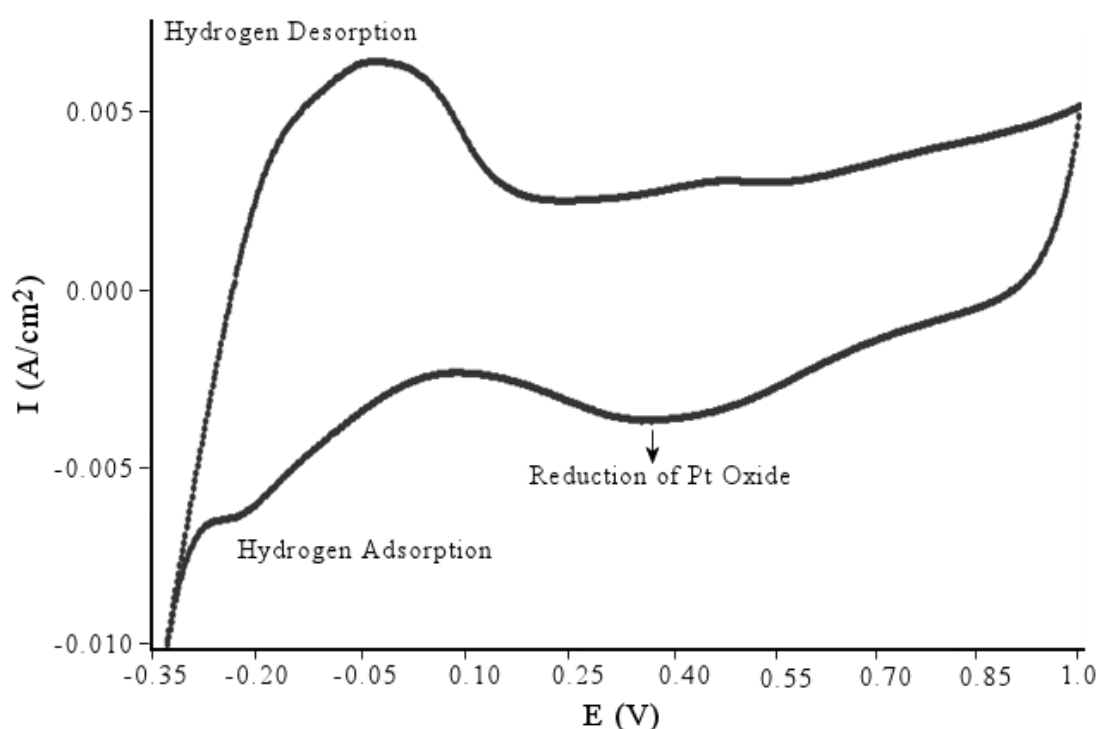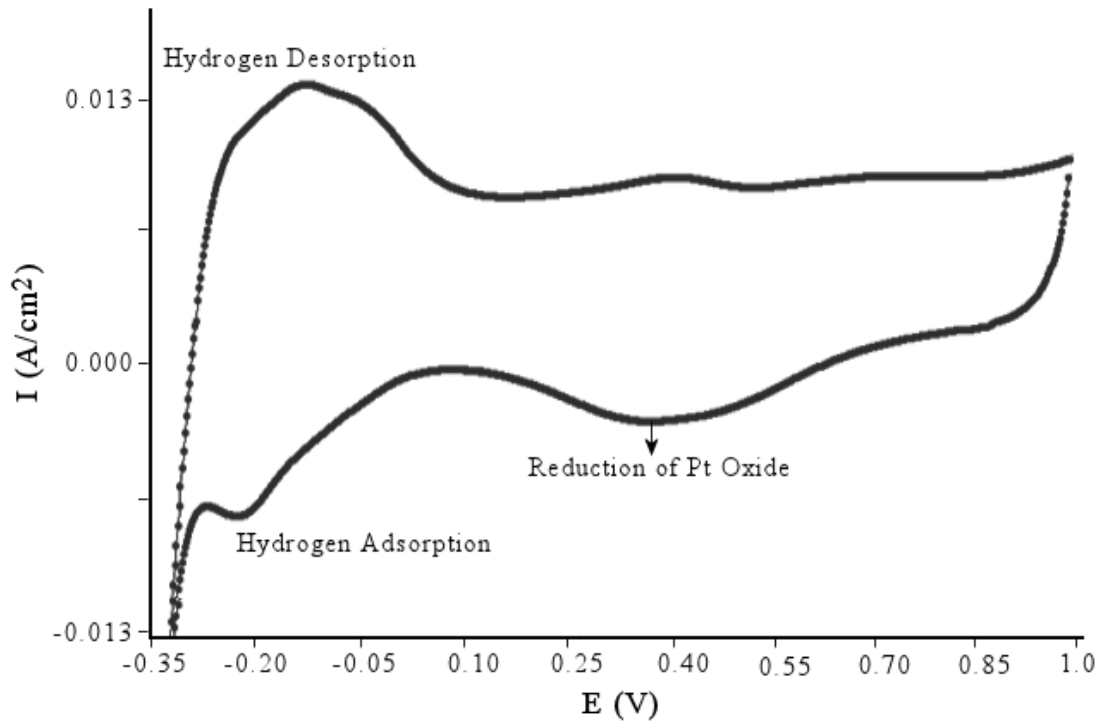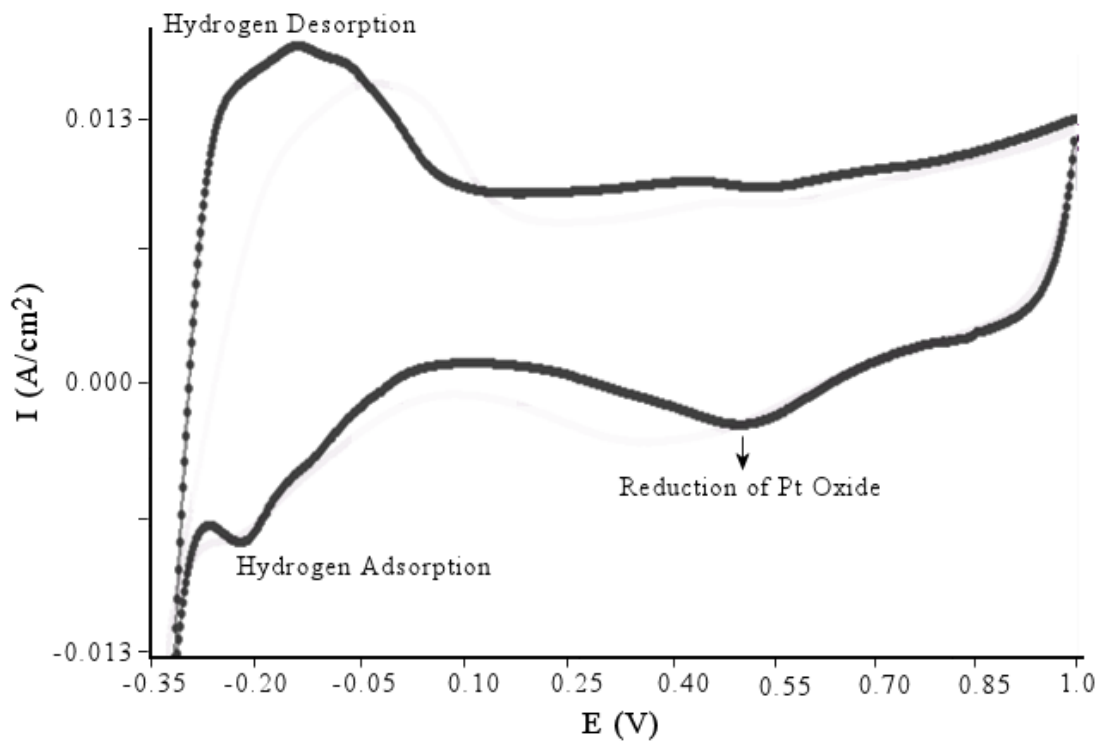

Figure 3.22.a. Cyclic voltammogram of Pt / GO in 0.5 M $HClO_4$

3.22.b. Cyclic voltammogram of Pt / 20 min TU treated GO in 0.5 M HClO$_4$

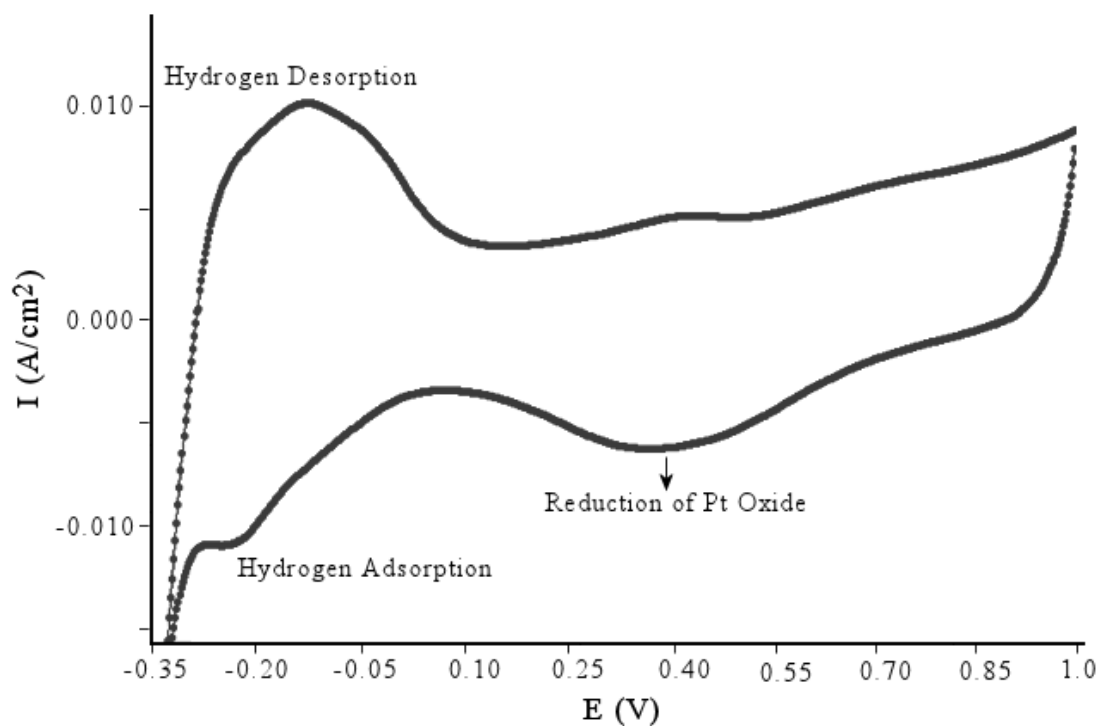3.22.c. Cyclic voltammogram of Pt / 2 hours TU treated GO in 0.5 M HClO$_4$

Figure 2.22.d. Cyclic voltammogram of Pt / 5 hours TU treated GO in 0.5 M HClO$_4$
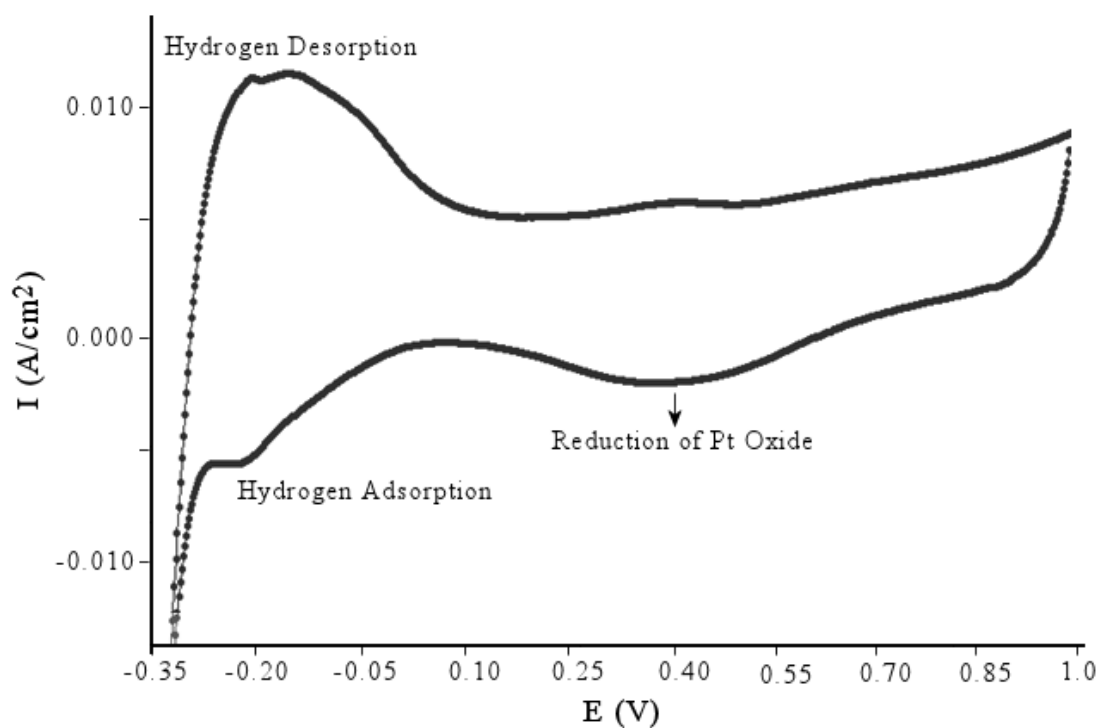

Figure 3.22.e. Cyclic voltammogram of Pt / 24 hours TU treated GO in 0.5 M HClO$_4$

In addition, electro-catalytic performances were examined via cyclic voltammetry (CV) of methanol electro-oxidation. Performances of Pt / supporting materials toward the methanol oxidation examined in 0.1 M $HClO_4$ mixed with 1 ml of 0.5 M CH_3OH at scan rate of 20 mV/s. In anodic sweeps, well-defined broad peaks corresponding to methanol oxidation was observed at around 0.8 V. On the other hand, in cathodic sweeps, sharper peaks which may be attributed to the removal of carbonaceous species not completely oxidized in the forward sweep were observed at around 0.6 V. The presence of only oxidation peaks in both forward and reverse sweeps indicates that electro-oxidation of methanol is an irreversible process.

The electro-oxidation of methanol on the prepared nanocatalysts was analyzed by basing on the two current peaks of the forward and reverse sweeps. It was seen that the methanol oxidation reaction starts at around 0.30 V for Pt/ GO and reaches its maximum potential at around 0.70 V, whereas it starts at around 0.20 - 0.25 V for Pt / TU treated nanocatalysts and reaches its maximum potentials at around 0.80 V. That is to say that the well-defined peaks preceded by a shoulder (onset) at about 0.20 V in the forward sweeps exhibit the characteristic features of methanol electro-oxidation. On the other hand, peaks in the reverse sweeps are considered as the result of the removal of carbonaceous species not completely oxidized in forward sweeps. The existence of anodic peaks for the electro-oxidation of methanol in both anodic and cathodic sweeps can be attributed to the high catalytic activity of the catalysts toward methanol oxidation reaction besides indicating the irreversibility of the reaction.

Amount of the methanol oxidized, that is to say the peak height (current) attained in forward sweep is proportional to the catalyst activity. For instance, among the prepared catalysts, Pt / 20 min TU treated GO showed the highest current peak toward methanol oxidation. This may be attributed to its higher surface area, higher Pt(0) ratio, and monodispersing. However, the electro-catalytic activities are based on the amount of platinum also. So, it is necessary to calculate the current exhibited per one gram of platinum in order to obtain the activities. In this context, the activities of all the prepared nanocatalysts toward methanol oxidation reaction was obtained by basing on the amounts of platinum on the working electrodes and CV measurements (Figure 3.23) performed between 0.0 and 1.0 volts at a scan rate of 20 mV/s in 0.1 M $HClO_4$ & 0.5 M CH_3OH electrolyte solution at room temperature. The

measurements were performed at least in ten cycles for one working electrode and by employing more than twenty different working electrodes for each of samples. The obtained activities, the voltage maxima and the poisoning degrees (If/Ir) of prepared nanocatalysts are listed in Table 3.14.

Table 3.14. Activities of prepared nanocatalysts toward methanol oxidation reaction

Type of Nanocatalyst	Peak Potential (V)	Current (A / g Pt)	I_f/I_r
Pt / GO	0.79	140	0.86
Pt / 20 min. TU treated GO	0.86	272	0.46
Pt / 2 h. TU treated GO	0.84	192	0.65
Pt / 5 h. TU treated GO	0.85	231	0.59
Pt / 24 h. TU treated GO	0.83	214	0.73

Regarding to methanol oxidation to carbon dioxide (CO_2), carbon monoxide which is the reaction intermediate is a common problem since it binds strongly to the Pt catalyst and deactivates it. The anodic peaks in the reverse sweep (I_r) are considered as attributing to the oxidation of residual intermediates. Many researchers suggest the peak ratio (I_f/I_r) is corresponding to the CO-poisoning factor. According to this remark, a small I_r indicates a highly elimination of the residual intermediates (CO) in the forward sweep, and this indicates a lower level of CO poisoning. However, according to some researchers, I_r is related to freshly chemisorbed methanol rather than to the residual CO [99]. According to Chung et al, the I_f/I_r ratio is not related to level of CO tolerance, but to degree of oxophilicity instead [100]. The lowest I_f/I_r ratio of Pt / 20 min and 5 h TU treated GOs and the highest one of Pt / GO may be evaluated in accordance with this remark.

Pt / 20 min TU treated GO showed the highest activity toward methanol oxidation (Figure 3.24). This may be attributed to its higher surface area (Table 3.17), higher Pt(0) ratio, monodispersed small particles (~ 3 nm). Pt / 5 h TU treated GO has also relatively higher activity which may be attributed its higher Pt(0) ratio and high surface area. Relatively lower activities of Pt / GO and Pt / 2 h TU treated GO may be the result of their lower Pt(0) ratios. The activities of the commercial catalyst E-TEK 40% Pt/Vulcan XC-72 and Pt/MWCNT are 75 and 140 A / (g of Pt) respectively [55]. That is to say that the activity of Pt / 20 min TU treated GO is about 2 times greater than that of the commercial catalyst Pt/MWCNT.

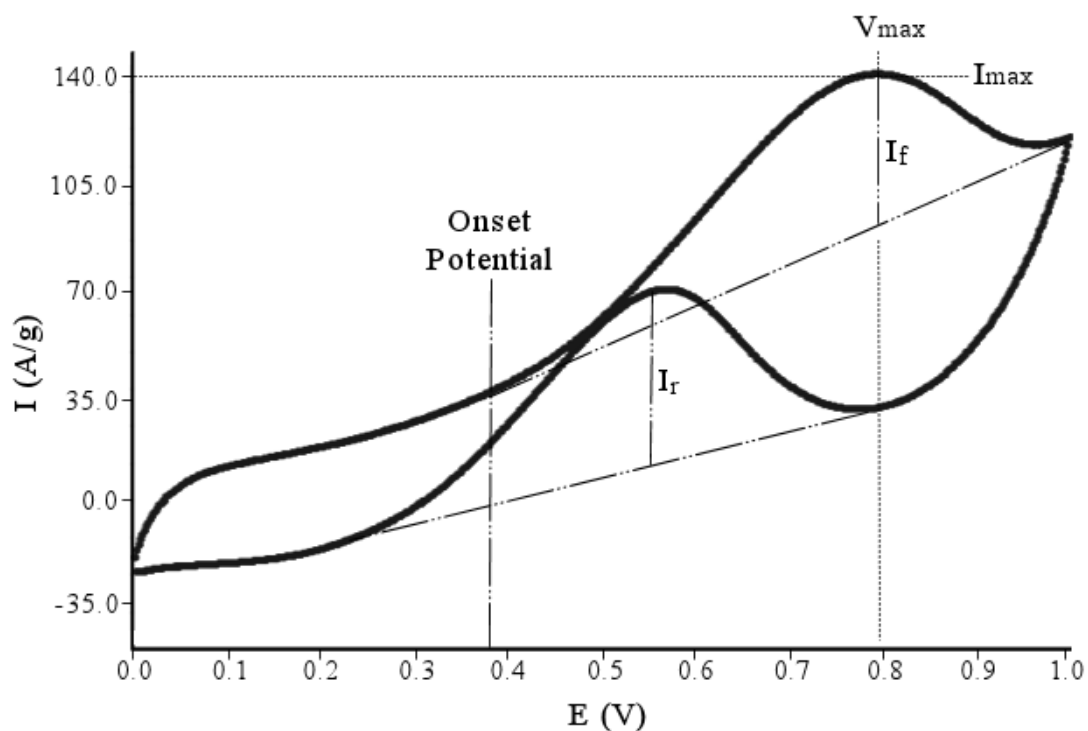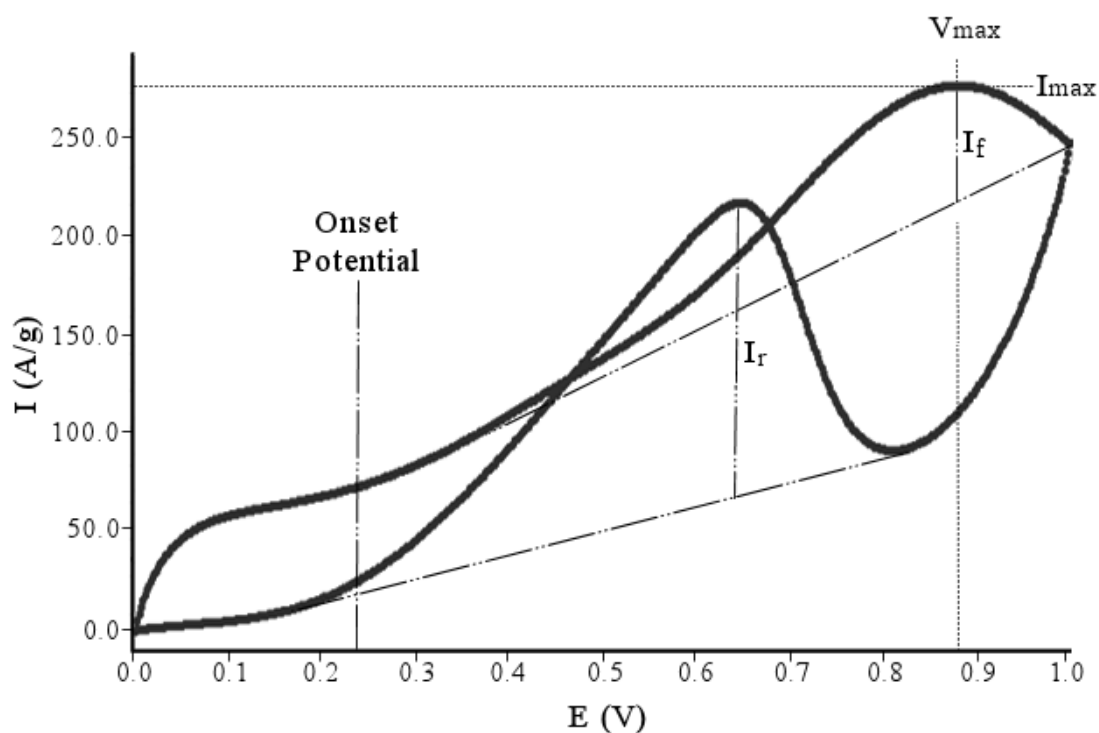Figure 3.23.a. Methanol oxidation peak of Pt / GO

Figure 3.23.b. Methanol oxidation peak of Pt / TU 20 min treated GO
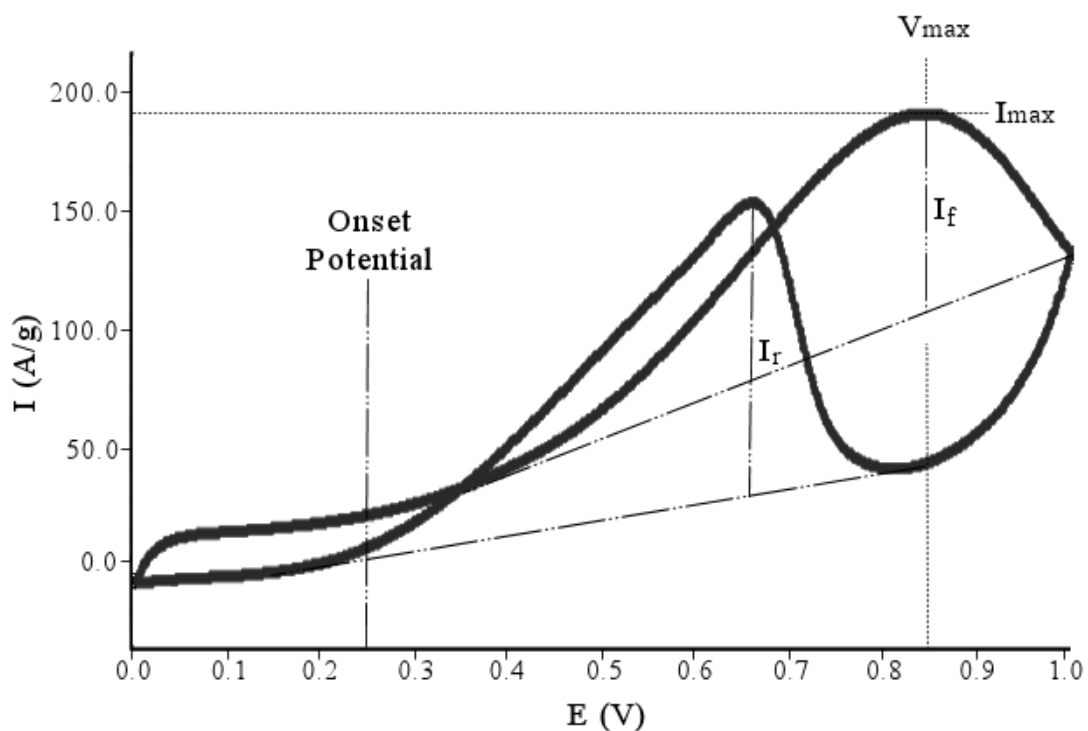
111

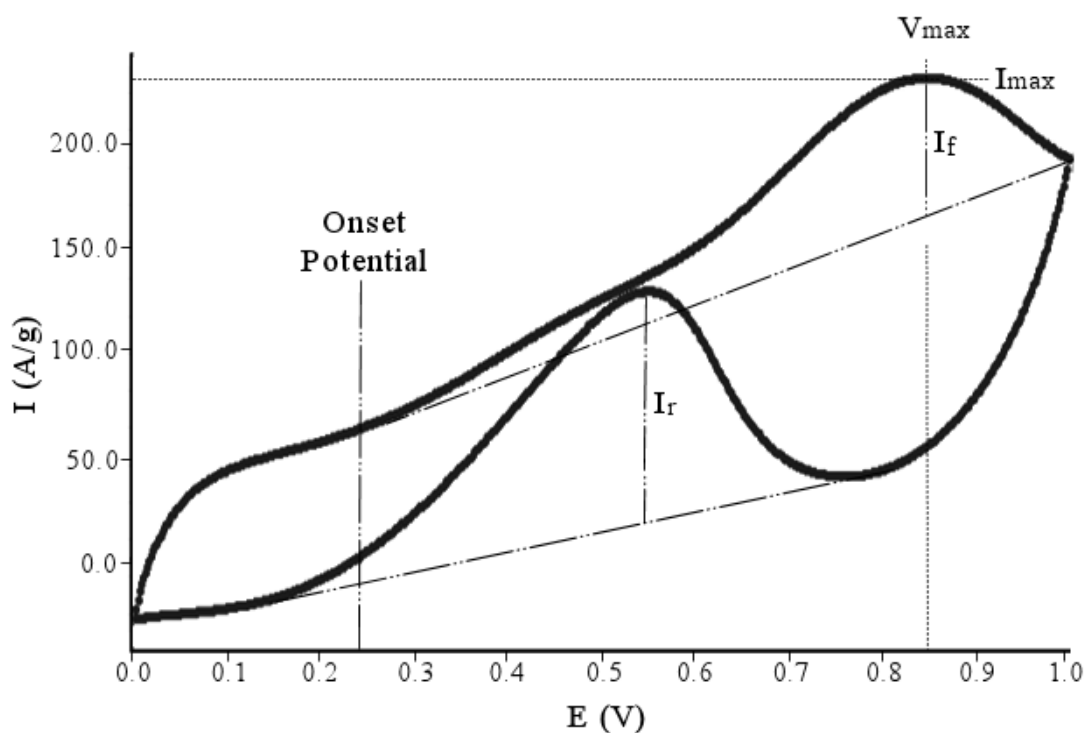Figure 3.23.c. Methanol oxidation peak of Pt / TU 2 h treated GO

Figure 3.23.d. Methanol oxidation peak of Pt / TU 5 h treated GO

112
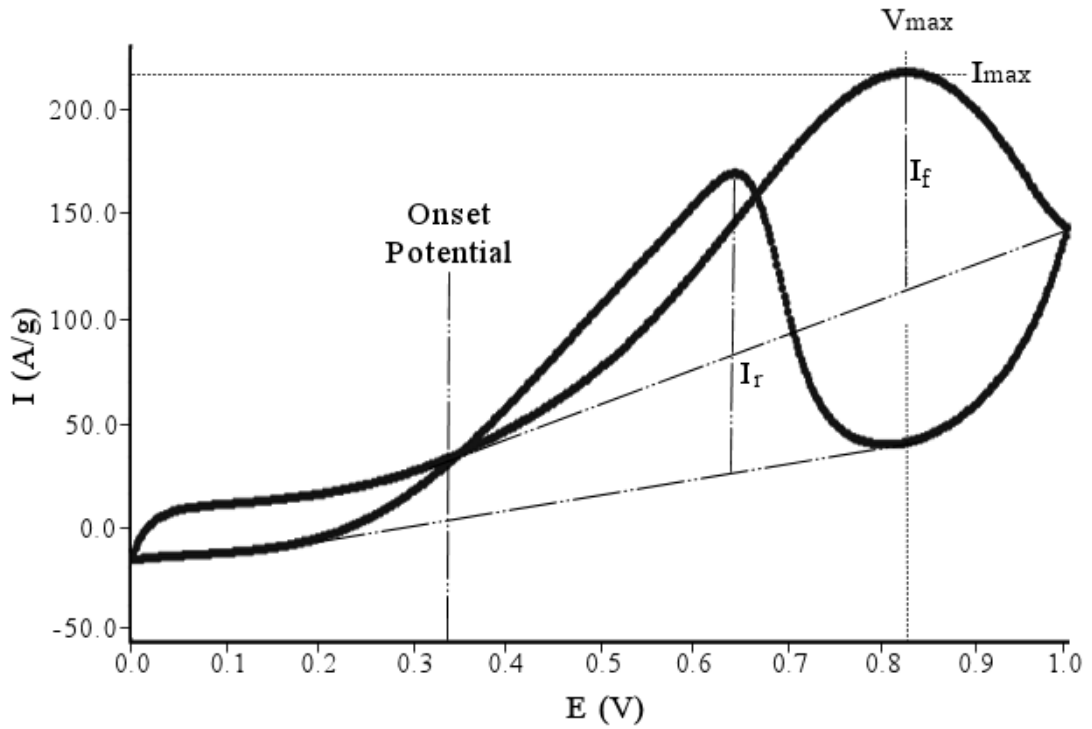
Figure 3.23.e. Methanol oxidation peak of Pt / TU 24 h treated GO
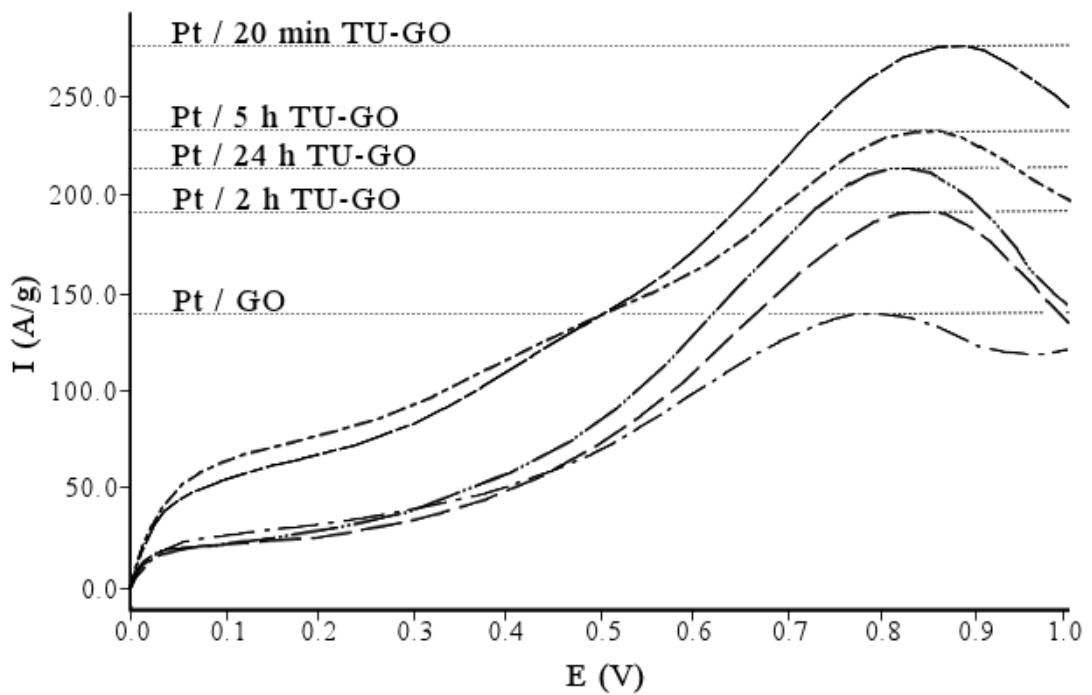
Figure 3.24. Methanol oxidation peaks of all catalytic samples

According to Chen et al. [101], the oxygen content is decreased in reduced graphene and the sp^2 carbons are restored after reduction. This exhibits much higher electrochemical capacitance and cycling durability than carbon nanotubes and chemically reduced graphene. Moreover, as a result of partially reduction, the elimination of oxide groups would create vacancies along the sp^2 carbon structure which could favor the deposition and dispersion of the platinum particles. The obtained activities may be evaluated also taking into account these remarks.

As a next step, the electrochemical properties of prepared nanocatalysts were examined by calculating their chemical surface areas (CSA), electrochemical surface areas (ECSA), platinum utilities, and the roughness factors. A not negligible part of Pt atoms present on the catalyst surface are not electrochemically active; that is to say that they are not accessible due to being localized inside small pores or the presence of excess oxides. So, the surface areas determined by cyclic voltammetry (ECSA) may be smaller than the intrinsic surface area of the catalyst (CSA). The ratio of ECSA and CSA is commonly used to evaluate the Pt utilization.

The CSA is the intrinsic surface area of a catalyst and inversly proportional to its average particle size. The chemical surface areas of all the prepared nanocatalysts were calculated (Table 3.15) by using the following formula:

$$CSA= 6000 / (\rho \times d)$$

where ρ is the density of Pt metal (21.40 g/cm^3), and d is the crystalline particle diameter (nm) obtained from XRD and TEM measurements [102].

Table 3.15. The chemical surface areas of prepared nanocatalysts

Type of Nanocatalyst	CSA (XRD)	CSA (TEM)
Pt / GO	66.28 m^2 / g Pt	71.89 m^2 / g Pt
Pt / 20 min. TU treated GO	79.65 m^2 / g Pt	84.96 m^2 / g Pt
Pt / 2 h. TU treated GO	63.86 m^2 / g Pt	67.77 m^2 / g Pt
Pt / 5 h. TU treated GO	79.20 m^2 / g Pt	79.88 m^2 / g Pt
Pt / 24 h. TU treated GO	60.42 m^2 / g Pt	64.76 m^2 / g Pt

Electrochemical surface area consists of the active (accessible) sites of the catalyst surface toward methanol oxidation reaction. It is inversely proportional to amount of platinum.

The electrochemical surface areas of each prepared nanocatalysts were calculated from the charges for hydrogen desorption and amount of platinum per one electrode, in accordance with the following formula:

$$ECSA = Q_{hyd} / (0.21 \text{ x } [Pt])$$

where Q_{hyd} is the electrical charge for hydrogen desorption (mC), 0.21 (mC/cm^2) [103] is the Pt crystalline activity surface area transition constant which represent the charge required to oxidize a monolayer of H_2 on bright Pt, and [Pt] (mg/cm^2) is the amount of Pt per one electrode calculated basing on ICP-MS results. The values of ECSA are reported in Table 3.17. It is seen that electrochemical surface areas decrease with increasing Pt particle size.

The charges for hydrogen desorption (Q_{hyd}) were calculated by integration of the area under the hydrogen desorption peak displayed by cyclic voltammograms in the range of -0.35 to 1.0 V (Figure 3.22). Gamry software was employed for integration. The Q_{hyd} values are reported in Table 3.16.

Table 3.16. Charges of hydrogen desorption regions

Type of Nanocatalyst	Q_{hyd} : Charge of Hydrogen Desorption Region
Pt / GO	9.15 mC
Pt / 20 min. TU treated GO	20.43 mC
Pt / 2 h. TU treated GO	14.50 mC
Pt / 5 h. TU treated GO	18.65 mC
Pt / 24 h. TU treated GO	11.40 mC

Table 3.17. ECSA values of prepared nanocatalysts

Type of Nanocatalyst	ECSA
Pt / GO	41.38 m^2 / g Pt
Pt / 20 min. TU treated GO	74.43 m^2 / g Pt
Pt / 2 h. TU treated GO	49.25 m^2 / g Pt
Pt / 5 h. TU treated GO	65.78 m^2 / g Pt
Pt / 24 h. TU treated GO	45.43 m^2 / g Pt

As a result, the ratio of the electrocatalytically active surface area which is accessible for reactants (ECSA) to the total surface area of Pt (CSA) gives the Pt utilizations (Table 3.18), as expressed by the following formula:

$$\text{Pt Utility (\%)} = (ECSA/CSA) \text{ x } 100$$

Table 3.18. Pt utilities of prepared nanocatalysts

Type of Nanocatalyst	% Pt Utility (XRD)	% Pt Utility (TEM)
Pt / GO	62.4	58.4
Pt / 20 min. TU treated GO	93.8	87.6
Pt / 2 h.　TU treated GO	77.1	72.7
Pt / 5 h.　TU treated GO	83.0	82.3
Pt / 24 h.　TU treated GO	75.2	70.1

The ratios of utility indicate the accessibility of the platinum surfaces. 100% Pt utilization ratio means that the entire Pt surface is accessible for reactants.

As the last parameter calculated, the roughness factor is the ratio of the actual electrochemically active catalyst surface area to geometric surface area; and it is required for defining morphology effects. Increased surface roughness causes increased surface area of the catalyst. The roughness factors for all prepared nanocatalysts were calculated (Table 3.19) as the ratio of the real area (A_{real}) to the geometrical area (A_{geom}) as expressed by the following formula:

$$R.F. = A_{real} / A_{geom}$$

Geometric surface area (A_{geom}) is the area of electrode employed. The electrode surface area (A) is equal to $\pi x r^2$, where r is the radius of electrode (0.35 cm). The actual surface area (A_{real}) is achieved by the means of following formula:

$$A_{real} = Q_{hyd} / 0.21$$

where Q_{hyd} is the electrical charge for hydrogen desorption (mC), and 0.21 is the Pt crystalline activity surface area transition constant (mC/cm^2).

Table 3.19. Roughness factors for prepared nanocatalysts

Type of Nanocatalyst	Roughness Factor (RF)
Pt / GO	114.6
Pt / 20 min. TU treated GO	256.0
Pt / 2 h.　TU treated GO	181.7
Pt / 5 h.　TU treated GO	233.7
Pt / 24 h.　TU treated GO	142.8

CHAPTER 4

CONCLUSION

Pt / graphene oxide (GO) and Pt / thiourea-treated GOs having different treatment durations were prepared. Characterizations were performed by Fourier Transform Infrared Spectroscopy (FTIR), Ultraviolet–Visible (UV-Vis) Spectrometry, acid-base back titration, X-ray Diffraction (XRD), Raman Spectroscopy, Transmission Electron Microscopy (TEM), X-ray Photoelectron Spectroscopy (XPS), and Inductively Coupled Plasma Mass Spectrometry (ICP-MS). The prepared nanocatalysts were then examined toward methanol oxidation reaction (MOR) by the means of Cyclic Voltammetry (CV). The following results were obtained:

1) GO, 20 min TU treated GO, 2 h TU treated GO, 5 h TU-treated GO and 24 h TU treated GO (r-GO) were found having 36%, 28%, 29%, 24%, 23% of carboxyl and hydroxyl functional groups respectively.

2) Thiourea was used as a reducing agent to obtain r-GO (24 h TU-treated GO) from GO; and, it was also employed for preparation of TU treated-GOs which were used as supports for catalysts.

3) For all prepared nanocatalysts, XRD patterns revealed the face centered cubic structures of the platinum nanoparticles and average particle sizes to be between 3-4 nm.

4) XPS analysis showed platinum in three oxidation states; and Pt(0) were found in higher ratios for all prepared nanocatalysts.

5) TEM images concluding XRD results showed that Pt / 20 min TU treated GO has monodispersed smallest particles (~3nm). Relatively larger (~4nm), less uniform, irregularly shaped and agglomerated particles were observed for Pt / 2h TU treated GO. For Pt / TU-5h treated GO, relatively smaller (~3.5 nm), more uniform particles and more dense distribution areas were seen in spite of some agglomerated areas. Images of Pt / 24 h treated GO showed

relatively larger (~4 nm), yet well-dispersed, more uniform particles, but more agglomeration. Relatively less uniform particles, less dense distribution areas and some agglomerated areas were seen in the images of Pt / GO.

6) The lowest catalytic performance toward methanol oxidation reaction was recorded for the Pt / GO (140 A/g) due to its relatively lowest Pt(0) ratio, electrochemical surface area (41.38 m^2 / g Pt), platinum utility (~60%) and roughness factor (115). However, this activity is almost 2 times higher than that of the commercial catalyst E-TEK 40% Pt / Vulcan XC-72 (75 A/g).

7) The highest catalytic performance toward methanol oxidation reaction was recorded for the Pt / TU 20 min-treated GO (272 A/g) due to its highest Pt(0) ratio, electrochemical surface area (74.43 m^2 / g Pt), platinum utility (~90%) and roughness factor (256). This activity is 3.6 times higher than that of the E-TEK 40% Pt / Vulcan XC-72.

REFERENCES

[1] Demirdöven, Nurettin, and John Deutch. "Hybrid cars now, fuel cell cars later." Science 305.5686 (2004): 974-976.

[2] Mench, Matthew M. Fuel cell engines. John Wiley & Sons (2008): 96-106.

[3] Thounthong, Phatiphat, Stephane Rael, and Bernard Davat. "Energy management of fuel cell/battery/supercapacitor hybrid power source for vehicle applications." Journal of Power Sources 193.1 (2009): 376-385.

[4] Larminie, James, Andrew Dicks, and Maurice S. McDonald. Fuel cell systems explained. John Wiley (2003): 22-24.

[5] Davy, Humphry. The Collected Works of Sir Humphry Davy (etc.). Smith, Elder & Co (1839): 107.

[6] Grove, William Robert. "On the gas voltaic battery. experiments made with a view of ascertaining the rationale of its action and its application to eudiometry." Philosophical Transactions of the Royal Society of London 133 (1843): 91-112.

[7] Appleby, A. J. "From Sir William Grove to today: fuel cells and the future." Journal of Power Sources 29.1-2 (1990): 3-11.

[8] Andújar, José Manuel, and Francisca Segura. "Fuel cells: History and updating. A walk along two centuries." Renewable and sustainable energy reviews 13.9 (2009): 2309-2322.

[9] Haber, Fritz, and Ludwik Bruner. "Das Kohlenelement, eine Knallgaskette." Berichte der Bunsengesellschaft für physikalische Chemie 10.37 (1904): 697-713.

[10] Schmid, A. "The Gas Diffusion Electrodes." Enke-Verlag, Stuttgart (1923).

[11] Baur, Emil, and Hans Preis. "Über Brennstoff-Ketten mit Festleitern." Berichte der Bunsengesellschaft für physikalische Chemie 43.9 (1937): 727-732.

[12] Davtyan, O. K. Gas cell with a solid electrolyte. Associated Technical Services (1946).

[13] Broers, G. H. J., and J. A. A. Ketelaar. "High temperature fuel cells." Industrial & Engineering Chemistry 52.4 (1960): 303-306.

[14] Bacon, F. T. "Fuel cells, past, present and future." Electrochimica Acta 14.7 (1969): 569-585.

[15] Kordesch, Karl. "Hydrogen-Oxygen Fuel Cells with Carbon Electrodes." Industrial & Engineering Chemistry 52.4 (1960): 296-298.

[16] Perry, Mike L., and Tom F. Fuller. "A historical perspective of fuel cell technology in the 20th century." Journal of the electrochemical society 149.7 (2002): S59-S67.

[17] Berger, Carl. "Fuel Cells Incorporating Ion Exchange Membranes: Current State of Development." (1965): 188-202.

[18] Chu, Deryn, and Sol Gilman. "Methanol Electro-oxidation on Unsupported Pt-Ru Alloys at Different Temperatures." Journal of The Electrochemical Society 143.5 (1996): 1685-1690.

[19] Handbook, Fuel Cell. "EG&G technical services." Inc., Albuquerque, NM, DOE/NETL-2004/1206 (2004): 1-32.

[20] O'Hayre, Ryan, et al. "Fuel Cell Thermodynamics." Fuel Cell Fundamentals (2006): 25-76.

[21] Li, Xianguo, L. Fields, and G. Way. "Principles of fuel cells." Platinum Metals Rev 50.4 (2006): 200-1.

[22] O'hayre, Ryan, et al. Fuel cell fundamentals. John Wiley & Sons (2016): 37-44.

[23] Coppo, M., N. P. Siegel, and M. R. Von Spakovsky. "On the influence of temperature on PEM fuel cell operation." Journal of Power Sources 159.1 (2006): 560-569.

[24] Blomen, Leo JMJ, and Michael N. Mugerwa, eds. Fuel cell systems. Springer Science & Business Media (2013): 250-252.

[25] Yamaguchi, Takeo, Hideki Kuroki, and Fusae Miyata. "DMFC performances using a pore-filling polymer electrolyte membrane for portable usages." Electrochemistry communications 7.7 (2005): 730-734.

[26] McGrath, Kimberly M., GK Surya Prakash, and George A. Olah. "Direct methanol fuel cells." Journal of Industrial and Engineering Chemistry 10.7 (2004): 1063-1080.

[27] Cameron, D. S., et al. "Direct methanol fuel cells." Platinum Metals Review 31.4 (1987): 173-181.

[28] Hogarth, M. P., and G. A. Hards. "Direct methanol fuel cells." Platinum Metals Review 40.4 (1996): 150-159.

[29] Ormerod, R. Mark. "Solid oxide fuel cells." Chemical Society Reviews 32.1 (2003): 17-28.

[30] Plomp, L., et al. "Improvement of molten-carbonate fuel cell (MCFC) lifetime." Journal of power sources 39.3 (1992): 369-373.

[31] Steele, Brian CH, and Angelika Heinzel. "Materials for fuel-cell technologies." Nature 414.6861 (2001): 345-352.

[32] Mehta, Viral, and Joyce Smith Cooper. "Review and analysis of PEM fuel cell design and manufacturing." Journal of Power Sources 114.1 (2003): 32-53.

[33] Barbir, Frano. "PEM fuel cells." Fuel Cell Technology. Springer London (2006): 27-51.

[34] Litster, S., and G. McLean. "PEM fuel cell electrodes." Journal of Power Sources 130.1 (2004): 61-76.

[35] McLean, G. F., et al. "An assessment of alkaline fuel cell technology." International Journal of Hydrogen Energy 27.5 (2002): 507-526.

[36] Coutanceau, C., et al. "Development of electrocatalysts for solid alkaline fuel cell (SAFC)." Journal of Power Sources 156.1 (2006): 14-19.

[37] Liu, Hansan, et al. "A review of anode catalysis in the direct methanol fuel cell." Journal of Power Sources 155.2 (2006): 95-110.

[38] Wasmus, S., and A. Küver. "Methanol oxidation and direct methanol fuel cells: a selective review." Journal of Electroanalytical Chemistry 461.1 (1999): 14-31.

[39] Arico, A. S., S. Srinivasan, and V1 Antonucci. "DMFCs: from fundamental aspects to technology development." Fuel cells 1.2 (2001): 133-161.

[40] Sundmacher, Kai, et al. "Dynamics of the direct methanol fuel cell (DMFC): experiments and model-based analysis." Chemical Engineering Science 56.2 (2001): 333-341.

[41] Clavilier, J., and S. G. Sun. "Electrochemical study of the chemisorbed species formed from formic acid dissociation at platinum single crystal electrodes." Journal of electroanalytical chemistry and interfacial electrochemistry 199.2 (1986): 471-480.

[42] Chrzanowski, Wojciech, and Andrzej Wieckowski. "Surface structure effects in platinum/ruthenium methanol oxidation electrocatalysis." Langmuir 14.8 (1998): 1967-1970.

[43] F. Şen, "The Preparation and Analysis of New Carbon Supported Pt and Pt+Second Metal Nanoparticles Catalysts for Direct Methanol Fuel Cells," Dr. Philos. Thesis Chem. METU, Ankara (2013).

[44] Ghenciu, Anca Faur. "Review of fuel processing catalysts for hydrogen production in PEM fuel cell systems." Current opinion in solid state and materials science 6.5 (2002): 389-399.

[45] Greeley, J., et al. "Alloys of platinum and early transition metals as oxygen reduction electrocatalysts." Nature chemistry 1.7 (2009): 552-556.

[46] Boreskov, Georgiĭ Konstantinovich. Heterogeneous catalysis. Nova Publishers, (2003): 1-86.

[47] Folkins, Hillis O., and Elmer Miller. "Preparation and Properties of Catalysts." Industrial & Engineering Chemistry 49.2 (1957): 241-244.

[48] Aruna, Singanahally T., and Alexander S. Mukasyan. "Combustion synthesis and nanomaterials." Current opinion in solid state and materials science 12.3 (2008): 44-50.

[49] Cao, Guozhong. Nanostructures and nanomaterials: synthesis, properties and applications. World Scientific (2004): 391-411.

[50] Chen, Jingyi, et al. "Shape-controlled synthesis of platinum nanocrystals for catalytic and electrocatalytic applications." Nano Today 4.1 (2009): 81-95.

[51] Burda, Clemens, et al. "Chemistry and properties of nanocrystals of different shapes." Chemical reviews 105.4 (2005): 1025-1102.

[52] Stiles, Alvin B. "Catalyst supports and supported catalysts." (1987).

[53] Fraga, M. A., et al. "Properties of carbon-supported platinum catalysts: role of carbon surface sites." Journal of Catalysis 209.2 (2002): 355-364.

[54] Frelink, T., W. Visscher, and J. A. R. Van Veen. "Particle size effect of carbon-supported platinum catalysts for the electrooxidation of methanol." Journal of Electroanalytical Chemistry 382.1-2 (1995): 65-72.

[55] Liu, Zhaolin, et al. "Carbon-supported Pt nanoparticles as catalysts for proton exchange membrane fuel cells." Journal of Power Sources 139.1 (2005): 73-78.

[56] Liu, Hansan, et al. "A review of anode catalysis in the direct methanol fuel cell." Journal of Power Sources 155.2 (2006): 95-110.

[57] Eriksson, Sara, et al. "Preparation of catalysts from microemulsions and their applications in heterogeneous catalysis." Applied Catalysis A: General 265.2 (2004): 207-219.

[58] Rymeš, J., et al. "Microemulsions in the preparation of highly active combustion catalysts." Catalysis Today 75.1 (2002): 297-303.

[59] Schwarz, James A., Cristian Contescu, and Adriana Contescu. "Methods for preparation of catalytic materials." Chemical Reviews 95.3 (1995): 477-510.

[60] Lewis, Larry N. "Chemical catalysis by colloids and clusters." Chemical Reviews 93.8 (1993): 2693-2730.

[61] Ahmadi, Temer S., et al. "Shape-controlled synthesis of colloidal platinum nanoparticles." Science-New York Then Washington- (1996): 1924-1925.

[62] Bonnemann, H., and K. S. Nagabhushana. "Advantageous fuel cell catalysts from colloidal nanometals." Journal of New Materials for Electrochemical Systems 7.2 (2004): 93-108.

[63] Islam, Md Aminul, M. Anwarul Kabir Bhuiya, and M. Saidul Islam. "A review on chemical synthesis process of platinum nanoparticles." Asia Pacific Journal of Energy and Environment 1.2 (2014): 107-20.

[64] Zhang, Changlin, et al. "A Generic Wet Impregnation Method for Preparing Substrate-Supported Platinum Group Metal and Alloy Nanoparticles with Controlled Particle Morphology." Nano letters 16.1 (2015): 164-169.

[65] Fulton, James W. "Selecting the catalyst configuration." Chemical Engineering 93.9 (1986): 97-101.

[66] Pinna, Francesco. "Supported metal catalysts preparation." Catalysis Today 41.1 (1998): 129-137.

[67] Lekhal, Azzeddine, Benjamin J. Glasser, and Johannes G. Khinast. "Impact of drying on the catalyst profile in supported impregnation catalysts." Chemical Engineering Science 56.15 (2001): 4473-4487.

[68] Geim, Andre K., and Konstantin S. Novoselov. "The rise of graphene." Nature materials 6.3 (2007): 183-191.

[69] Geim, A. K. "Graphene prehistory." Physica Scripta 2012.T146 (2012): 014003.

[70] Allen, Matthew J., Vincent C. Tung, and Richard B. Kaner. "Honeycomb carbon: a review of graphene." Chemical reviews 110.1 (2009): 132-145.

[71] Brodie, Benjamin C. "On the atomic weight of graphite." Philosophical Transactions of the Royal Society of London 149 (1859): 249-259.

[72] Dreyer, Daniel R., et al. "The chemistry of graphene oxide." Chemical Society Reviews 39.1 (2010): 228-240.

[73] Gao, Wei, et al. "New insights into the structure and reduction of graphite oxide." Nature chemistry 1.5 (2009): 403-408.

[74] He, Heyong, et al. "A new structural model for graphite oxide." Chemical physics letters 287.1 (1998): 53-56.

[75] Mao, Shun, Haihui Pu, and Junhong Chen. "Graphene oxide and its reduction: modeling and experimental progress." Rsc Advances 2.7 (2012): 2643-2662.

[76] Pumera, Martin. "Graphene-based nanomaterials for energy storage." Energy & Environmental Science 4.3 (2011): 668-674.

[77] Chua, Chun Kiang, and Martin Pumera. "Monothiolation and reduction of graphene oxide via one-pot synthesis: hybrid catalyst for oxygen reduction." ACS nano 9.4 (2015): 4193-4199.

[78] G. Gökağaç, J. M. Léger, and F. Hahn, "Behaviour of bimetallic Pt-Pd carbonsupported catalysts in methanol electrooxidation," Zeitschrift fur Naturforsch. -Sect. B J. Chem. Sci. 58. 5 (2003): 423–432.

[79] Doyle, Walter M. "Principles and applications of Fourier transform infrared (FTIR) process analysis." Process control and quality 2.1 (1992): 11-41.

[80] Long, Derek Albert, and D. A. Long. Raman spectroscopy. Vol. 206. New York: McGraw-Hill (1977).

[81] Chauhan, Ashish, and Priyanka Chauhan. "Powder XRD technique and its applications in science and technology." Journal of Analytical & Bioanalytical Techniques 5.5 (2014): 1.

[82] Clark, Roger N. "Spectroscopy of rocks and minerals, and principles of spectroscopy." Manual of remote sensing 3 (1999): 3-58.

[83] Gurker, Norbert, Maria F. Ebel, and Horst Ebel. "Imaging XPS -A new technique, I-principles." Surface and Interface Analysis 5.1 (1983): 13-19.

[84] Thomas, Robert. Practical guide to ICP-MS: a tutorial for beginners. CRC press (2013): 1-4.

[85] Williams, David B., and C. Barry Carter. "The transmission electron microscope." Transmission electron microscopy. Springer Us (1996): 3-17.

[86] Burghardt, Robert C., and Robert Droleskey. "Transmission electron microscopy." Current protocols in microbiology (2006): 2B-1.

[87] Evans, Dennis H., et al. "Cyclic voltammetry." (1983): 290.

[88] Stewart, James E. "Infrared absorption spectra of urea, thiourea, and some thiourea-alkali halide complexes." The Journal of Chemical Physics 26.2 (1957): 248-254.

[89] Lu, Jinlin, et al. "Self-assembled platinum nanoparticles on sulfonic acid-grafted graphene as effective electrocatalysts for methanol oxidation in direct methanol fuel cells." Scientific reports 6 (2016): 21530.

[90] Jankovský, O., et al. "Towards graphene bromide: bromination of graphite oxide." Nanoscale 6.11 (2014): 6065-6074.

[91] Cheng, Meng, et al. "Restoration of graphene from graphene oxide by defect repair." Carbon 50.7 (2012): 2581-2587.

[92] Das, Ashok Kumar, et al. "Iodide-mediated room temperature reduction of graphene oxide: a rapid chemical route for the synthesis of a bifunctional electrocatalyst." Journal of Materials Chemistry A 2.5 (2014): 1332-1340.

[93] Tang, Zhicheng, Dongsheng Geng, and Gongxuan Lu. "Size-controlled synthesis of colloidal platinum nanoparticles and their activity for the electrocatalytic oxidation of carbon monoxide." Journal of colloid and interface science 287.1 (2005): 159-166.

[94] Ha, Hyung-Wook, et al. "One-pot synthesis of platinum nanoparticles embedded on reduced graphene oxide for oxygen reduction in methanol fuel cells." Electrochemical and Solid-State Letters 14.7 (2011): B70-B73.

[95] Chang, Chia-Feng, Quang Duc Truong, and Jiann-Ruey Chen. "Retracted: Graphene as excellent support for rapid and efficient near infrared-assisted triptic proteolysis." (2013): 221-228.

[96] Liao, Hong-Gang, et al. "Facet development during platinum nanocube growth." Science 345.6199 (2014): 916-919.

[97] Moulder, J. F. Handbook of X-ray photoelectron spectroscopy: a reference book of standard spectra for identification and interpretation of XPS data. Eds. Jill Chastain, and Roger C. King. Eden Prairie, Minnesota: Physical Electronics Division, Perkin-Elmer Corporation (1992).

[98] Z. Ozturk, F. Sen, S. Sen, and G. Gokagac, "The preparation and characterization of nano-sized Pt-Pd/C catalysts and comparison of their superior catalytic activities for methanol and ethanol oxidation," J. Mater. Sci. 47.23 (2012): 8134–8144.

[99] Hofstead-Duffy, Augusta M., et al. "Origin of the current peak of negative scan in the cyclic voltammetry of methanol electro-oxidation on Pt-based electrocatalysts: a revisit to the current ratio criterion." Journal of Materials Chemistry 22.11 (2012): 5205-5208.

[100] Chung, Dong Young, Kyung-Jae Lee, and Yung-Eun Sung. "Methanol electro-oxidation on the Pt surface: revisiting the cyclic voltammetry interpretation." The Journal of Physical Chemistry C 120.17 (2016): 9028-9035.

[101] Chen, Yao, et al. "High performance supercapacitors based on reduced graphene oxide in aqueous and ionic liquid electrolytes." Carbon 49.2 (2011): 573-580.

[102] B. Krishnamurthy and S. Deepalochani, "Performance of Platinum Black and Supported Platinum Catalysts in a Direct Methanol Fuel Cell," Int. J. Electrochem. Sci, 4 (2009): 386–395.

[103] Z. Dongping, J. Velmurugan, and M. V. Mirkin, "Adsorption/desorption of hydrogen on Pt nanoelectrodes: Evidence of surface diffusion and spillover," J. Am. Chem. Soc. 131.41 (2009): 14756–14760.